

INFORMATION TO USERS

This manuscript has been reproduced from the microfilm master. UMI films the text directly from the original or copy submitted. Thus, some thesis and dissertation copies are in typewriter face, while others may be from any type of computer printer.

The quality of this reproduction is dependent upon the quality of the copy submitted. Broken or indistinct print, colored or poor quality illustrations and photographs, print bleedthrough, substandard margins, and improper alignment can adversely affect reproduction.

In the unlikely event that the author did not send UMI a complete manuscript and there are missing pages, these will be noted. Also, if unauthorized copyright material had to be removed, a note will indicate the deletion.

Oversize materials (e.g., maps, drawings, charts) are reproduced by sectioning the original, beginning at the upper left-hand corner and continuing from left to right in equal sections with small overlaps. Each original is also photographed in one exposure and is included in reduced form at the back of the book.

Photographs included in the original manuscript have been reproduced xerographically in this copy. Higher quality 6" x 9" black and white photographic prints are available for any photographs or illustrations appearing in this copy for an additional charge. Contact UMI directly to order.

UMI

**A Bell & Howell Information Company
300 North Zeeb Road, Ann Arbor MI 48106-1346 USA
313/761-4700 800/521-0600**



CHARACTERIZATION OF TRAPPED PARTICLES IN RF PLASMAS

by

Michael Joseph Schabel

Copyright © Michael Joseph Schabel 1997

**A Thesis Submitted to the Faculty of the
DEPARTMENT OF MATERIALS SCIENCE AND ENGINEERING
In Partial Fulfillment of the Requirements
For the Degree of
Master of Science
In the Graduate College
THE UNIVERSITY OF ARIZONA**

1997

UMI Number: 1386622

**Copyright 1997 by
Schabel, Michael Joseph**

All rights reserved.

**UMI Microform 1386622
Copyright 1997, by UMI Company. All rights reserved.**

**This microform edition is protected against unauthorized
copying under Title 17, United States Code.**

UMI
300 North Zeeb Road
Ann Arbor, MI 48103

STATEMENT BY AUTHOR

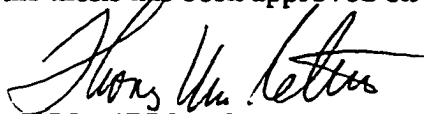
This thesis has been submitted in partial fulfillment of requirements for an advanced degree at The University of Arizona and is deposited in the University Library to be made available to borrowers under rules of the Library.

Brief quotations from this thesis are allowable without special permission, provided that accurate acknowledgement of source is made. Requests for permission for extended quotation from or reproduction of this manuscript in whole or in part may be granted by the copyright holder.

SIGNED: 

APPROVAL BY THESIS DIRECTORS

This thesis has been approved on the date shown below:

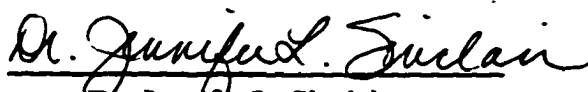


Dr. Thomas W. Peterson
Professor of

Chemical and Environmental Engineering

8/15/97

Date



Dr. Jennifer L. Sinclair
Associate Professor of

Chemical and Environmental Engineering

8/11/97

Date



Dr. David C. Lynch
Professor of

Materials Science and Engineering

8-18-97

Date

Acknowledgments

I would like to express my sincere appreciation to my advisors Dr. Thomas W. Peterson, Dr. Jennifer L. Sinclair, and Dr. David C. Lynch. Their advice, guidance, encouragement, and patience was what made this research successful. I would also like to thank my parents, Cheryl and William Bandi, and Joseph Schabel, whose support of all of my endeavors is never-ending and is always appreciated. I was also blessed by the patience of Melissa Duhaime, who helped me get to the end. I was fortunate to be assisted in this research by Mark Zerella whose contribution to this work went far beyond expectations. I would like to thank Mary Garrity, who arranged for an Optical Emission Spectrometer to be used in this work on loan from IBM East Fishkill and who always found time to field my questions about plasmas and micro-contamination. Finally, I would like to thank the Center for Micro-Contamination at the University of Arizona for funding this research and providing industrial guidance.

TABLE OF CONTENTS

LIST OF FIGURES	7
LIST OF TABLES	10
ABSTRACT	11
1. Introduction	12
2. Plasma and Particle Theory	19
2.1 Plasma Theory	20
2.2 Particle Formation	28
2.3 Particle Charging	29
2.4 Particle Trapping	30
2.4.1 Electrostatic Forces	31
2.4.2 Gravitational Forces	32
2.4.3 Ion Collisions	33
2.4.4 Ion Orbital Forces	36
2.4.5 Neutral Collisions	37
2.4.6 Charged Particle-Induced Dipole Forces	38
2.4.7 Thermophoretic Forces	45
2.4.8 Neutral Drag Forces	47
2.4.9 Summary of Forces	48
2.5 Brownian Particle Motion	49
2.6 Atom-Particle Collisions	52
2.7 Coulombic Interactions	54
2.8 Coulombic Particle Theory	61
2.9 Summary	62

3. Experimental Diagnostic Theory.	64
3.1 Optical Emission Spectroscopy.	65
3.1.1 Atomic Emission.	67
3.1.2 Molecular Emission.	73
3.1.3 OES Instrumentation.	74
3.1.4 Instrument Resolution and Limitations	76
3.2 Laser Light Scatter.	78
3.3 Laser Doppler Velocimetry	80
3.3.1 General Laser Doppler Velocimetry Theory.	81
3.3.2 Extended LDV Hardware Theory	85
3.3.3 LDV Data Reduction.	90
4. Experimental Setup.	94
4.1 Base Configuration.	94
4.2 Experimental Diagnostic Equipment.	102
4.2.1 Optical Emission Spectroscopy.	102
4.2.2 Laser Light Scatter.	103
4.2.3 Laser Doppler Velocimeter/Phase Doppler Particle Analysis	104
4.2.4 Scanning Electron Microscopy.	107
4.3 Electrode Configuration.	107
4.4 Grounding.	109
5. Trapped Particle Characterization	111
5.1 Seeded Particles	112
5.2 Laser Light Scatter	117
5.3 Optical Emission Spectroscopy	131
5.4 Long Term Particle Trap Behavior.	138
5.5 Laser Doppler Velocimetry.	147

5.6 Summary of Experimental Results	169
5.7 Particle Motion Model	173
5.8 Charged Particle-Deposition Model	177
5.9 Particle Agglomeration Model	180
6. Conclusions	184
SCIENTIFIC CONTRIBUTIONS	187
LIST OF SYMBOLS	188
REFERENCES	193

LIST OF FIGURES

2.1.1	Paschen curve for hydrogen	21
2.1.2	Plasma potential across electrodes	22
2.1.3	Anisotropic plasma chemical etching of a substrate	23
2.4.1	Sphere of influence	39
2.4.2	Velocity of polarized argon atom.	44
2.4.3	Thermophoretic forces versus applied temperature gradient.	46
2.5.1	Particle motion due to thermal energy considerations.	51
2.6.1	Particle motion by Coulombic interactions.	57
2.6.2	Comparison of Coulomb theory and thermal energy theory.	58
2.6.3	Particle velocity versus separation distance.	60
3.1.1	Schematic energy level diagram.	68
3.1.2	Representative argon emission spectra.	69
3.1.3	Diffraction interface.	75
3.3.1	Laser beam intersection.	82
3.3.2	Intersection of probe volume with a flat plate.	83
3.3.3	Gaussian intensity profile.	83
3.3.4	High frequency signal from a moving particle.	84
3.3.5	Signal processing to generate a Doppler burst.	85
3.3.6	Schematic of optic manipulation in an Aerometrics Fiber Drive.	87
4.1.1	Tegal MCR-1 modified plasma etcher.	95
4.1.2	Gas flow path into plasma chamber.	96
4.1.3	Gas exit slots in exhaust manifold.	97
4.1.4	Calibration curve for argon mass flow controller.	99
4.2.1	Emission collection region in plasma.	103

4.2.2	Measurement coordinate reference frames for LDV.	105
4.3.1	Base configuration with raised chuck.	108
4.3.2	Modified chamber schematic.	109
5.0.1	Particle trap locations.	111
5.1.1	FESEM micrograph of agglomerated PSL particles	114
5.1.2	FESEM micrograph of monodisperse PSL particles	115
5.1.3	Schematic of particle injector	117
5.2.1	LLS of particles at 30 W, 16 mTorr	119
5.2.2	LLS of particles at 100 W, 16 mTorr.	120
5.2.3	LLS of particles at 150 W, 16 mTorr.	120
5.2.4	LLS of particles at 200 W, 16 mTorr.	121
5.2.5	LLS of particles at 30 W, 16 mTorr.	121
5.2.6	LLS of particles at 30 W, 22 mTorr	122
5.2.7	LLS of particles at 30 W, 29 mTorr	122
5.2.8	LLS of particles at 30 W, 35 mTorr	123
5.2.9	LDV traversing system.	124
5.2.10	Data rate versus probe position in ground plane trap.	125
5.2.11	Error in making boundary measurements based on data rate	126
5.2.12	Outline of particle trap cross section	128
5.2.13	Particle trap decay in time	130
5.3.1	Emission intensity in time	132
5.3.2	Comparison of emission for dusty and pristine plasmas.	133
5.3.3	Comparison of emission for high and low particle concentrations	133
5.3.4	Equilibrium time dependence on power.	134
5.3.5	Equilibrium time dependence on pressure	134
5.3.6	Secondary transient response to pressure change	136
5.3.7	Secondary transient response to power change	137

5.4.1	Cross section rate loss versus power	139
5.4.2	Cross section rate loss versus pressure.	139
5.4.3	Emission-time profiles for varied power at constant pressure.	140
5.4.4	Emission-time profiles for varied pressure at constant power.	141
5.4.5	Variation of trap cross section with power.	142
5.4.6	Variation of trap cross section with pressure.	142
5.5.1	Representative azimuthal velocity histogram.	149
5.5.2	Velocity vectors for particles passing through the LDV control volume.	150
5.5.3	Fraction of particles exhibiting a specified velocity.	151
5.5.4	Location of mapped slice and measured velocity directions.	154
5.5.5	Contour plot of azimuthal velocity.	155
5.5.6	Vertical velocity profile.	156
5.5.7	Radial velocity profile	157
5.5.8	Vertical velocity profiles for varied pressure	158
5.5.9	Mean particle velocity versus pressure	158
5.5.10	Radial velocity profile for varied power	159
5.5.11	Mean particle velocity versus power	160
5.5.12	Vertical local concentration profile for varied power	162
5.5.13	Maximum local particle concentration for varied power.	163
5.5.14	Radial local concentration profiles for varied pressure.	163
5.5.15	Maximum local concentration for varied pressure.	164
5.5.16	Area particle density versus pressure.	165
5.5.17	FESEM micrograph of PSL particle exposed to a plasma.	167
5.7.1	Predicted particle velocity for varied pressure.	175
5.7.2	Predicted particle velocity for varied power.	175
5.7.3	Comparison of experiment and model: velocity versus pressure.	176
5.7.4	Comparison of experiment and model: velocity versus power.	177
5.9.1	Hard collision approach velocities.	182

LIST OF TABLES

3.2.1	Argon emission intensities from Figure 3.2.2.	70
5.6.1	Summary of experimental results.	169

ABSTRACT

Particle contamination in plasma processing is a serious and challenging issue for the semiconductor industry. In this work, Laser Doppler Velocimetry, Laser Light Scattering, and Optical Emission Spectroscopy are used to elucidate the physical behavior of particles trapped in a plasma. Coulomb theory is used to describe the motion of particles. The theory agreed very well with experimental data and was explored to evaluate conditions for which particle agglomeration is likely. Finally, it was observed that particles may fall out of the particle trap during plasma ignition and subsequently contaminate the substrate.

CHAPTER 1

Introduction

Computer micro-chips are manufactured from blank silicon wafers by chemically machining the surface of the wafer into millions of electrical transistors. Consumer demands have encouraged the semiconductor industry to develop micro-chips that are extremely small with the ability to process information at high speeds. Industry's response in reducing the size of transistors on chips has been so consistent that its technological advance is well characterized by Moore's first law: *the number of transistors that one could put on a chip will double approximately every 20 months* [1]. One may conclude that transistor dimensions will quickly approach molecular length scales. The steady decrease in transistor size and a company's desire to be the first to profit from the implementation of new technology fuels the current research in semiconductor processing development.

As the transistor size decreases and the number of transistors per chip increases, the probability that the chip may be faulty due to an error in the manufacturing process increases. Often these errors are undetectable until the completion of the processing of the computer chip. There are many potential sources of error in manufacturing computer chips; one source is micro-contamination. In general, there are many types of micro-

contamination, but of particular interest to this work is micro-contamination due to particles. Particulate micro-contamination has a variety of sources: operator, air-borne in the environment, processing equipment, and the process itself. Particles that fall on the wafer during the manufacturing processes affect the performance of the micro-chips. Significant attempts have been made to reduce the potential for contamination due to the operators and the processing facilities. Additionally, wafer handling has evolved into an exacting science.

Contamination due to the manufacturing processes presently remains a serious challenge to the industry. The reasons for this are many, including the fact that identification of the source of contamination remains difficult with current analytical and diagnostic capabilities. Furthermore, once the source of particle formation is identified, removal of the source can be detrimental to the process itself. Of particular interest to the present research is the exploration of micro-contamination issues associated with plasma processing.

Plasma processing has seen widespread use in the semiconductor industry. In a modern fabrication facility, plasmas are used for substrate etching, chemical vapor deposition, chamber cleaning, and process gas abatement. In some applications, secondary chemical reactions can lead to the formation of particles. The particles can accrue a negative surface potential and become trapped in the plasma, resulting in very long residence times with respect to the residence time of the process gas. The long residence time increases the probability that the particle will grow due to chemical vapor deposition

or by colliding with a nearby particle and agglomerating. Once the plasma is extinguished, the force field that contributes to particle suspension diminishes. Depending on the conditions of the reactor, there are multiple possibilities regarding particle trajectories once the plasma is extinguished [2]. Small particles (~10 nm diameter) are easily entrained in the gas flow and can be carried out of the reactor in the exhaust stream. Larger particles, however, are greatly influenced by gravitational forces, and often fall onto and contaminate the surface of the wafer.

Particle contamination of wafers during processing costs the semiconductor industry enormous amounts of money every year. Blewer [3] estimated that a ten percent reduction in defect density can save a new fabrication facility over one billion dollars in its first year of operation. Reducing contamination also has a significant impact on environmental issues. Currently, cleaning steps, which are very environmentally unfriendly, are required to reduce particle contamination. If particle contamination can be reduced at the point of origin, fewer cleans will be required.

Selwyn *et al.* [3] observed that the cost associated with contamination is not only due to reduced product yield, but also to unnecessary operational costs. For example, a series of plasma etchers occupies large regions of space in a typical class 10 clean room. However, the environment inside the plasma chamber might be considered a class 10,000 clean room due to the formation of particles during the etch process. Therefore, large sums of money are expended to keep the environment around the plasma chamber clean, but since the wafer is inevitably exposed to the plasma chamber, the clean external

or by colliding with a nearby particle and agglomerating. Once the plasma is extinguished, the force field that contributes to particle suspension diminishes. Depending on the conditions of the reactor, there are multiple possibilities regarding particle trajectories once the plasma is extinguished [2]. Small particles (~10 nm diameter) are easily entrained in the gas flow and can be carried out of the reactor in the exhaust stream. Larger particles, however, are greatly influenced by gravitational forces, and often fall onto and contaminate the surface of the wafer.

Particle contamination of wafers during processing costs the semiconductor industry enormous amounts of money every year. Blewer [3] estimated that a ten percent reduction in defect density can save a new fabrication facility over one billion dollars in its first year of operation. Reducing contamination also has a significant impact on environmental issues. Currently, cleaning steps, which are very environmentally unfriendly, are required to reduce particle contamination. If particle contamination can be reduced at the point of origin, fewer cleans will be required.

Selwyn *et al.* [3] observed that the cost associated with contamination is not only due to reduced product yield, but also to unnecessary operational costs. For example, a series of plasma etchers occupies large regions of space in a typical class 10 clean room. However, the environment inside the plasma chamber might be considered a class 10,000 clean room due to the formation of particles during the etch process. Therefore, large sums of money are expended to keep the environment around the plasma chamber clean, but since the wafer is inevitably exposed to the plasma chamber, the clean external

environment has almost no bearing on the total contamination of the wafer. This example demonstrates that significant advances in processing as well as industry wide cost savings can be realized by studying and then eliminating the actual process of contamination in a plasma chamber.

Researchers have taken many different approaches to trying to reduce the particle contamination problem in plasmas. One approach is to understand how the particles nucleate in the plasma and then either adjust the reactor operating conditions or introduce a chemical inhibitor so that the precursor concentration in the chamber is minimized. Much of the current research in identifying chemical precursors has been with silane as a parent gas [5-11], although other gases have begun to receive attention [12-16]. The primary difficulties with researching gases other than silane, especially those used in etching applications, are that the chemistry and the chemical pathways are relatively unknown and the gases tend to be electronegative. For reasons which will be discussed in Chapter 2, process gas electronegativity introduces interesting challenges for modern metrology and spectrometry, making identification and quantification of potential particle nucleation precursors a difficult task. A challenge to the precursor identification and minimization approach is that there may be multiple precursors to particle formation evident in the form of photoresist and various materials already deposited on the substrate (oxides, nitrides, metal, etc.).

Other research groups have approached the micro-contamination problem by studying the forces acting on the particles, thereby elucidating the reasons why the

particles trap in the plasma. A suitable modification of reactor geometry or operating conditions might change the force field acting on the particles so that the particles are never trapped in the first place. One possible avenue is to modify the electric field that produces the plasma, by either changing the electrical properties or the geometry of the electrode [17]. This research area has seen a considerable modeling effort [18-21] which is often utilized to design plasma chambers. Electric field studies have also been experimentally approached and have been used to more thoroughly understand how the particles interact with the plasma [22-26].

Some researchers have attempted to take advantage of the fact that the particles can be manipulated by various fields while the plasma is ignited or after it is extinguished [27-29]. Some of the forces used for manipulating particles include magnetic forces, DC electric fields, thermophoretic forces, and fluid forces. One may find any number of these solutions used for a particular plasma processing application, however no general solution is currently available. Additionally, evidence suggests that the particles actually contaminate the wafer while the plasma is ignited [30] and may contribute to a phenomena known as “micromasking”, where it is possible that very small particles mask regions on the surface of the wafer and prevent uniform etching. Whereas a post-ignition particle manipulation strategy may serve to reduce the particle contamination problem, it does not necessarily eliminate the potential for contamination during plasma ignition.

In the present research, the goal is to experimentally study how the particles and the particle traps behave in the plasma environment and develop a physical model to

explain the behavior. An understanding of the inter-particle behavior as a function of various reactor operating conditions can be used to manipulate how the particles agglomerate. Although this research makes no attempt to establish the ideal reactor conditions for low levels of contamination (primarily because this is specific to the reactor being used), it does attempt to explain under what conditions a certain particle morphology might be expected due to particle collisions and agglomeration. As a result, the reactor could be designed so that only a certain type of particle, ideally one that is easily removed by a second process, falls on the wafer.

In this work, particle and particle trap behavior is studied using Laser Doppler Velocimetry (LDV), Laser Light Scattering (LLS), and Optical Emission Spectroscopy (OES). LDV is used to measure the velocity profiles of particles traveling through a fixed control volume in the plasma chamber. This control volume is traversed throughout the chamber in order to determine spatially resolved particle velocity profiles and local concentration profiles. Simultaneously, the particle trap behavior is studied using LLS and the plasma emission is monitored using OES. The three techniques employed together allow for a complete plasma-particle study. Some theories governing trapped particle behavior are developed here and some have been presented by other researchers in the literature. All of the theories are compared to experimental data of the current research and to that of other researchers in order to explain how and why particles move in the plasma. Once it is understood why particles move, it is possible to formulate a model that describes the motion of particles with respect to each other and to determine reactor

conditions for which the particles might collide and agglomerate. In addition, the model can be used to describe reactor conditions for which the particles are likely to fall out of the particle trap while the plasma is ignited, which leads to contamination.

CHAPTER 2

Plasma and Particle Theory

Plasma processing is an essential capability in manufacturing computer micro-chips. Often, exotic and complicated chemistry is utilized in the processing of a micro-chip. Plasmas allow for the desired chemistry to take place at temperatures much lower than the temperatures which would begin to cause damage to the chip. Additionally, special electrical properties of plasmas allow for surface chemistry to occur anisotropically on the surface of the substrate. In contrast, wet chemical processing techniques only allow for isotropic surface chemistry to occur.

Whereas the extreme chemical reactivity and electrical properties of a plasma are necessary for manufacturing modern micro-chips, these same properties promote the production of particles and contribute to wafer contamination, ultimately resulting in reduced product yields. A clear understanding of the relationship between plasma reactor operating conditions and the formation of contaminating particles is essential for eliminating plasma-induced micro-contamination. Particles accrue a surface potential in the presence of the plasma, and as a result, can become trapped in the plasma. The forces acting on the particles are introduced to aid in the discussion of the movement of trapped particles. Three theories are presented in an attempt to explain particle motion: thermal

kinetic energy, particle-molecule collisions, and coulombic particle-particle interactions. To conclude, a review of coulombic crystal theory is given to reinforce the idea that the particles should not be considered as non-interacting, as is commonly assumed in the literature.

2.1 Plasma Theory

A plasma is the fourth state of matter, and is comprised of neutrals, charged species (ions), and electrons. The migration of charged species allows for the transmission of electricity between two electrodes. The ability of a particular gas to conduct electricity depends on how much energy is needed to ionize the gas, the voltage drop applied to the electrodes, the distance between the two electrodes, and the concentration of the gas between the electrodes. There are two limits for a particular gas at which electron transmission is difficult. The first is at very low pressures, where the mean spacing between molecules and electrons is much larger than the physical dimensions of the reactor. In this case, the electrons travel from one electrode to the other without ever colliding with and ionizing a molecule. This situation does not promote the chemical reactivity that is desired for chemical processing. At the other extreme, the gas pressure is very high, resulting in a short ion lifetime. The time averaged concentration of ions in the chamber is so low that the plasma quickly chokes itself out. Using very high voltage drops across the electrodes can counter this problem, but results in high reactor temperatures

and is undesirable for micro-electronic processing. Between these two extremes, at moderate pressures and moderate voltage drops (i.e. 10 mTorr and 50 V/cm), the production and lifetime of ions is sufficient to sustain an electrical discharge. The voltage at which the discharge is sustained for a given pressure is called the breakdown voltage, V_B . The relationship between breakdown voltage, pressure, p , and electrode spacing, d , called the Paschen curve, is shown in Figure 2.1.1 for hydrogen gas [31].

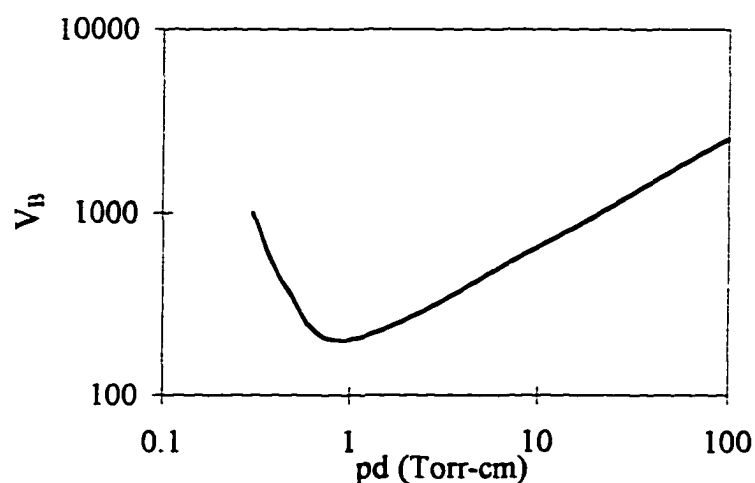


Figure 2.1.1 Paschen curve for Hydrogen, adapted from ref. [31]

As mentioned previously, one benefit of using plasma processing is that anisotropic chemical reactions can occur. For example, given a plasma with two electrodes and with ions and electrons in the bulk, there will exist a potential difference between the electrodes and the bulk plasma, and the electrodes will be negative with respect to the bulk due to charge continuity considerations. The potential boundary layer near the electrodes where

the potential changes from the value at the electrodes to the bulk potential is called the Debye sheath (Figure 2.1.2).

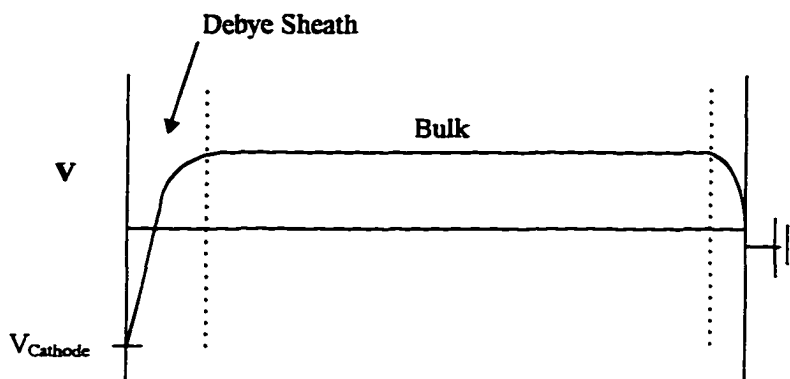


Figure 2.1.2 Plasma potential across electrodes

Positive ions will respond to the potential gradient and will accelerate normal to the electrode. The ions can reach velocities exceeding an order of magnitude greater than their thermal kinetic velocities. As such, they may contribute large amounts of energy to any surface reactions. This phenomenon is referred to as ion bombardment and is used in a variety of applications, including reactive ion etching, target sputtering, and ion implantation. In the case of reactive ion etching, ions help to mill trenches in the surface of the wafer where the vertical etch rate (due to chemical reactions plus ion bombardment) greatly exceeds the horizontal etch rate (due to chemical reactions alone) as shown in Figure 2.1.3.

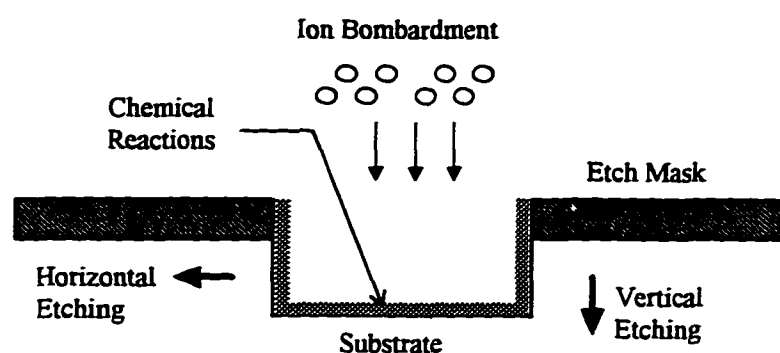


Figure 2.1.3 Anisotropic plasma reactive ion etching of a substrate

In order to achieve anisotropic etching properties, the substrate must be placed on the electrode. Typically, the substrate is a silicon wafer, which is an insulator. DC discharges will not ignite if an insulator is placed over the electrode, so time varying electric fields are used instead. Often, capacitively or inductively coupled radio frequency (rf=13.56 MHz) discharges are used for processing applications. To a lesser extent, microwave discharges are also now utilized in industry.

Sustained plasma ignition occurs only if there is a charge balance in the reactor; the number of electrons and negatively charged ions must identically balance the number of positively charged ions. This is referred to as quasineutrality. For a plasma that is at steady state, the production rate of electrons due to ionization of neutral molecules must equal

the rate at which the ions recombine to form neutrals. Furthermore, the flux of charged species to a surface must balance for quasineutrality to hold.

In general, the charged species will move through the plasma by diffusion. The charged species also respond to the electric field and experience an enhanced diffusivity called ambipolar diffusion. The flux of each of the species can be written as:

$$\begin{aligned}\Gamma_e &= -D_e \nabla n_e - \mu_e n_e E \\ \Gamma_+ &= -D_+ \nabla n_+ - \mu_+ n_+ E \\ \Gamma_- &= -D_- \nabla n_- - \mu_- n_- E\end{aligned}\quad [2.1.1 \text{ a,b,c}]$$

where n_i is the specie concentration, E is the strength of the electric field, μ_i is the specie mobility, D_i is the specie diffusion, and Γ_i is the specie flux. The subscript (i) refers to positive ions (+), negative ions (-), and electrons (e). By equating the specie flux, it is possible to eliminate the electric field. The electron flux is found by substituting the electric field into Equation 2.1.1a:

$$\Gamma_e = - \left\{ \frac{[D_e(\mu_- + \mu_+)n_e + (D_e\mu_+ + D_+\mu_e)]\nabla n_e + \mu_e n_e (D_+ + D_-)\nabla n_-}{(\mu_e + \mu_+)n_e + (\mu_- + \mu_+)n_-} \right\} \quad [2.1.2]$$

The fluxes for positive and negative ions are found in a similar manner. From these equations, chemical kinetic reaction rates can be theoretically developed based on the probability of collision, the concentration of the reactants (n_e , n_+ , n_- being the electron,

positive ion, and negative ion concentrations, respectively), the temperature at which the reaction takes place, and the activation energies for the reaction.

Defining a reaction temperature is not straightforward. The oscillating electric field which is used to overcome plasma generation problems in the presence of an insulating substrate will cause the electrons to move rapidly in the chamber and obtain very high kinetic energies and high temperatures, T_e . The electron energy distribution function (EEDF) is often approximated as being Maxwellian, although this is not strictly correct. Ions are too massive to respond to the 13.56 MHz field, so they remain at temperatures, T_i , near the neutral gas temperature, T_n . The electron temperature usually greatly exceeds the ion temperature.

Substantial efforts have been made in the modeling community to solve appropriate balance equations to determine the strength of the field in a plasma, kinetic reaction rates, species concentrations, plasma potential, electron energy distributions, and average electron energy [18-21]. These models are used to study surface chemistry [32] (i.e. wafer etching), particle formation [33], particle transport [34], and environmental concerns [35]. Experimental verification of the modeling results is currently crude at best, primarily because plasma diagnostic capabilities are limited. This issue is discussed in Chapter 3. Nonetheless, determination of the plasma parameters is very important for describing plasma-particle interactions. A number of physical relationships between the primary plasma parameters have been discovered by dimensional analysis of the balance laws for each of the species. Using these relationships, reasonable estimates of the plasma

parameters can be made without resorting to models which require significant computational resources.

The average electron density, \bar{n}_e , can be related to the applied power dissipated in the plasma, W , and the strength of the electric field, E :

$$\frac{W}{V} = \bar{n}_e q v_d E \quad [2.1.3]$$

where V is the volume of the reactor, q is the charge of an electron (-1.6×10^{-19} C), and v_d is the electron drift velocity. For convenience, this can be rearranged to:

$$\frac{\bar{n}_e}{\Lambda(W/V)} = [q v_d p \Lambda(E/p)]^{-1} \quad [2.1.4]$$

where p is the pressure and Λ is the electron diffusion length, which is found from scaling the electron balance equation [36]:

$$\frac{1}{\Lambda^2} = \left(\frac{2.405}{R}\right)^2 + \left(\frac{\pi}{2L}\right)^2 \quad [2.1.5]$$

where $2L$ is the electrode spacing of a reactor with a cylindrical shell of radius R . The electron drift velocity can be approximated by an electron energy balance:

$$v_d \approx \left[\frac{T_e (1.6 \times 10^{-19})}{2m_e} \right]^{1/2} \quad [2.1.6]$$

Finally, it has been observed that the electron temperature is proportional to the electric field divided by the chamber pressure (E/p) over large ranges of E/p :

$$T_e \propto \frac{E}{p} \quad [2.1.7]$$

Substituting 2.1.6 and 2.1.7 in 2.1.3 allows the electron density to be rewritten as:

$$\bar{n}_e = \frac{W}{qV(4 \times 10^{-10})} \frac{p^{1/2}}{E^{3/2}} \left(\frac{2m_e}{c} \right)^{1/2} \quad [2.1.8]$$

where c is a proportionality constant for Equation 2.1.7.

From these equations, the average electron density, average electron temperature, kinetic reaction rates, ion concentrations, and species concentrations can be estimated with knowledge of the deposited power, the volume of the cylindrical reactor, the chamber pressure, and the strength of the electric field. In the following sections, the usefulness of these approximations will become evident.

2.2 Particle Formation

Particle contamination in a plasma can be generated in a number of ways. For example, particles can enter into the chamber with the silicon wafer, can form from homogeneous gas phase nucleation, and can form on the surface of chamber walls. Evidence in the literature suggests that all of these are important contributors to the total contamination of the wafer [37,38].

Gas phase nucleation of particles in silane chemistries has been thoroughly studied and is fairly well understood. It is believed that anions are the major precursor to particle formation, and the process occurs by anionic clustering of molecules [39]. Gas phase nucleation studies of plasma gases other than SiH_4 are rather limited and appears to be due to the inherent difficulty of working with the gases and due to electronegativity. Electronegativity occurs when the molecular species in the plasma are likely to form negatively charged ions. The negative ion concentrations can often exceed the electron concentration and are very difficult to measure while the plasma is ignited. Recall from Chapter 2.1 that the positive ions will travel down the potential gradients and accelerate towards the electrodes. This feature makes positive ion extraction for spectroscopic measurement relatively easy. Negative ions, on the other hand, will not accelerate to the walls, but will remain in the bulk plasma. In electronegative plasmas, the negative ions may be significant contributors to particle formation. However, detection is very difficult while the plasma is ignited and precursor identification remains a challenge. In addition,

the presence of the negative ions in the plasma causes difficulties when making experimental electrical measurements. For these reasons, chemistry models which could be used to predict precursors to particle formation cannot be readily experimentally verified.

2.3 Particle Charging

Particles in a plasma are floating potential bodies. The surface of the particle immersed in a plasma will see a flux of charged and neutral species. In general, the mobility of the electrons in the presence of an electric field is much greater than the mobility of the ions due to mass considerations. For this reason, the electrons will have a much higher flux to the surface of the particle than will the ions. However, the charged specie flux must balance for charge neutrality, so the particle must charge negatively in order to repel some of the electrons. Only the highest energy electrons will be able to overcome the repulsive negative particle-electron forces. In some cases, the high energy electron-particle collisions can result in the ejection of electrons from the surface of the particle, and the particle might exhibit a positive charge. This is not common in plasmas used for semiconductor processing; the particle usually charges negatively.

Ions and electrons will recombine on the surface of the particle, therefore the charge of the particle is not constant. However, the charge fluctuations are small relative to the time averaged surface charge, so the particle charge can be considered to be at quasi-steady state. Whipple performed some of the pioneering work in determining

particle charge [40]. Carlile and Nowlin [41] used Coulomb potential theory to determine the charge of a particle immersed in an argon plasma:

$$Q_p = -5 \times 10^{-12} (d_p / 2) T_e^{0.85} T_i^{0.15} \quad [2.3.1]$$

where d_p is the particle diameter in cm and T_e and T_i are in eV. Particle charge has also been evaluated experimentally [42,43].

2.4 Particle Trapping

Suspension of particles in localized regions of the plasma comes from a zero net force acting on the particles. There is agreement throughout the literature [25, 44-46] regarding the primary forces acting on the particles. These include electrostatic, neutral drag, neutral collision, ion collision, ion orbital, thermophoretic, and gravitational forces. It is often assumed that the trapped particles do not interact with each other, so each particle can be modeled as an isolated system in the plasma. This assumption is reasonable for determining the long time average locations of the particle trap, but is not valid when particle motion is described. In the following sections, a mathematical description of the forces acting on the particles is presented along with estimates of the magnitude of the force acting on 10.2 μm polystyrene latex (PSL) spheres. Additionally, the forces will be

classified as isotropic, in that they act uniformly over the surface of the sphere, or as directional, thus having the tendency to push the particle in a particular direction.

2.4.1 Electrostatic Forces

In Chapter 2.3, it was shown that the particles will tend to charge negatively in order to balance the flux of mobile electrons and heavy ions to its surface. As a result, the charged particles will respond to the electric field strength, \mathbf{E} . The force, \mathbf{F} , acting on the particle is:

$$\mathbf{F}_E = Q_p \mathbf{E} \quad [2.4.1]$$

Again, Q_p is the net charge of the particle from Equation 2.3.1. The electrostatic force is the predominant force acting on the particles and to first order can be used in a force balance with gravity to approximate the particle trapping locations in the plasma chamber. The field due to an electric field strength of 1600 V/m is approximately 8×10^{-12} N. In a uniform gravitational field, the particles will trap where the potential of the plasma is the highest. Considerable research [22,23,47,48] has shown that the particles are not always located directly where the plasma potential is the highest due to the effect of other forces acting on the particle. The magnitudes of these forces are highly dependent on the

chamber conditions, i.e. temperature gradients, pressure, flow patterns, and hence the relative importance of each force varies from chamber to chamber.

2.4.2 Gravitational Forces

Gravity tends to pull the particles down to the electrode, and becomes an extremely important force in the afterglow (when the plasma is extinguished) of low pressure etch reactors. This is an unfortunate consequence of modern plasma reactor design, in that the primary force acting on the particles tends to induce contamination rather than prevent it. Naturally, many processing techniques have been developed to reduce this problem, but it remains that gravity is a difficult force to “turn off”, especially for large particles. The gravitational force acting on the particle is given by:

$$\mathbf{F}_g = m_p \mathbf{g} \quad [2.4.2]$$

where the mass of the particle, m_p is:

$$m_p = \frac{4}{3} \rho_p \pi r_p^3 \quad [2.4.3]$$

r_p is the particle radius (m) and ρ_p is the particle density (kg/m^3). A $10.2 \mu\text{m}$ PSL particle experiences a gravitational force having a magnitude of approximately $5.7 \times 10^{-12} \text{ N}$ and is directed axially down towards the electrode.

2.4.3 Ion Collisions

The charged particle radiates an electric field which affects nearby ions. The ions will accelerate through the local particle electric field and impact the surface at a speed higher than their neutral counterparts. The maximum velocity, u_B , that the ion will reach is given by the Bohm criterion [49]:

$$u_B = \sqrt{\frac{2k_B T_e}{m_i}} \quad [2.4.4]$$

where k_B is the Boltzmann factor and m_i is the mass of the ion. In an argon plasma with an electron temperature of $k_B T_e = 4 \text{ eV}$, the Bohm velocity is approximately $4,400 \text{ m/s}$. It is known that the presence of the particles has an effect on the average electron temperature, especially in the vicinity of the particle trap and is highly dependent on the concentration of the trapped particles. At high particle concentrations, Bouchoule and Boufendi [50] observed that the local average electron temperature is approximately twice that of a pristine plasma, so one might expect that the Bohm velocity can extend up to 7000 m/s .

The force exerted on the particles due to ion-particle collisions [45] is given by:

$$F_i^c = n_i v_s m_i v_i \pi b_c^2 \quad [2.4.5]$$

where n_i is the ion concentration [$\#/m^3$], v_s is the mean ion velocity relative to the moving particle [m/s], v_i is the actual velocity of the ion relative to the particle, and b_c is a collisional frequency coefficient related to the charge on the particle and its associated collision cross section. The mean speed of the ions is given by:

$$v_s = \left[v_n^2 + v_i^2 \right]^{1/2} \quad [2.4.6]$$

where v_n is the average neutral gas thermal velocity:

$$v_n = \left(\frac{8k_B T_i}{\pi m_i} \right)^{1/2} \quad [2.4.7]$$

Equation 2.4.6 can be rearranged to include the Bohm velocity:

$$v_s = u_B \left[\frac{4}{\pi} \left(\frac{T_i}{T_e} \right) + \left(\frac{v_i}{u_B} \right)^2 \right]^{1/2} \quad [2.4.8]$$

The ion temperature is near room temperature for cold plasmas (0.0258 eV), whereas the electron temperature is on the order of 4 eV, so $T_i/T_e \approx 0$, hence $v_s \approx |v_i|$. In order to characterize the full range of ion velocities in the vicinity of the particle, the lower limit is selected as the neutral thermal velocity (350 m/s) and the upper limit is taken as the Bohm velocity (~4000 m/s).

The collision frequency parameter, b_c , is given by:

$$b_c = r_p \left[1 - \frac{2qQ_p}{4\pi\epsilon_0 m_i v_s^2 r_p \left(1 + \frac{r_p}{\lambda_D} \right)} \right]^{1/2} \quad [2.4.9]$$

where ϵ_0 is the vacuum permittivity ($8.8542 \times 10^{-12} \text{ C}^2/\text{N}\cdot\text{m}^2$) and λ_D is the Debye length given by:

$$\lambda_D = \left(\frac{\epsilon_0 k_B T_e}{n_e q^2} \right)^{1/2} \quad [2.4.10]$$

where n_e is the electron density ($\#/m^3$). If it is assumed that the electron temperature is 4 eV and the electron concentration is $1 \times 10^{16} \#/m^3$, the corresponding Debye length will be 149 μm . Low pressure capacitively coupled rf glow plasmas are only partially ionized and

typical ion concentrations are typically on the order of $1 \times 10^{16} \text{ \#/m}^3$ whereas the neutral atom concentration at 10 mTorr is approximately $5 \times 10^{20} \text{ \#/m}^3$.

The maximum force due to ion collisions, also called “ion wind”, is approximately equal to $3.2 \times 10^{-12} \text{ N}$ for the conditions listed. If the electron temperature is assumed to increase to 10 eV due to high particle concentration effects, the maximum force increases to $7.1 \times 10^{-12} \text{ N}$. A minimum force of $2.2 \times 10^{-12} \text{ N}$ occurs if all of the ions hitting the particle surface exhibit the neutral thermal velocity. The flux of positively charged species is in the direction towards the electrodes, so the force acting on the particles is also in the direction towards the electrode.

2.4.4 Ion Orbital Forces

Barnes *et al.* [45] proposed a second ion-related force acting on the particles. This force is due to ions orbiting around the particle:

$$\mathbf{F}_i^o = 4\pi n_i m_i v_i v_i b_{\pi/2}^2 \Gamma \quad [2.4.11]$$

where $b_{\pi/2}$ is a cross section determined by the ratio of the energy of the field to the energy of the ion moving around the particle and is given by:

$$b_{\pi/2} = \frac{qQ_p}{4\pi\epsilon_0 m_i v_s^2} \quad [2.4.12]$$

Γ is an interaction parameter relating the size of the amplified cross section, $b_{\pi/2}$, to the Debye length, λ_D , and the ion collision cross section, b_c , and is given by:

$$\Gamma = \frac{1}{2} \ln \left[\frac{(\lambda_D / b_{\pi/2})^2 + 1}{(b_c / b_{\pi/2})^2 + 1} \right] \quad [2.4.13]$$

As before, if it is assumed that the maximum force occurs if the orbiting ions have velocities equal to the Bohm velocity, then the force acting on the particles is 3×10^{-11} N. This force acts uniformly over the entire surface of the particle with no directionality.

2.4.5 Neutral Collisions

Neutral molecules can collide with the particle and impart a force on it:

$$F_n^c = n_n m_n v_n^2 \pi r_p^2 \quad [2.4.14]$$

where n_n , m_n , and v_n are the neutral molecule concentration, mass, and relative velocity, respectively. The neutral molecules, moving at their thermal velocity, collide uniformly

over the surface of the particle. The neutral molecule velocity is assumed to move much faster than the particle as predicted by Equation 2.4.7.

At low pressures, the neutral molecules are assumed to behave ideally, so the neutral gas density can be found from the ideal gas law. The magnitude of the total force acting on the surface is approximately 2.6×10^{-10} N. This is a strong force compared to the ion forces and the gravitational force. However, since it acts uniformly over the particle surface, it does not contribute to particle trapping. It may be partly responsible for the Brownian motion of the particle. This force is strong because of the high concentration of neutral atoms in the presence of the particle as compared with the ion concentration. The force could be even stronger if the neutral particles had a higher velocity in the presence of the charged particle.

2.4.6 Charged Particle-Induced Dipole Forces

The high concentration of neutral argon atoms may collide with the particle at velocities higher than the neutral average thermal velocity if they become polarized by the electric field and then accelerate due to electrostatic interactions. There are two electric fields in the plasma chamber which may polarize an argon atom: the outside plasma electric field and the inside particle electric field. Consider the following situation as shown in Figure 2.4.1.

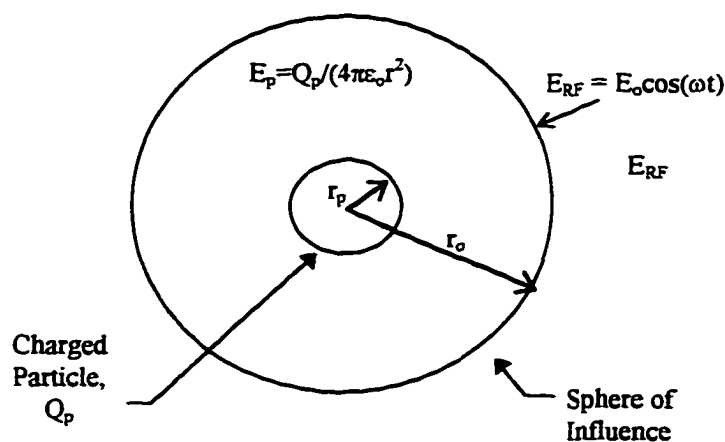


Figure 2.4.1 Schematic representing the electric field sphere of influence surrounding a charged particle

There is a sphere of influence with a radius, r_o , surrounding the particle. All of the argon atoms outside this sphere will be strongly affected by the time varying rf electric field and will only be slightly influenced by the field radiated from the charged particle. All of the argon atoms inside of the sphere of influence will be strongly affected by the constant field radiated from the charged particle and only slightly influenced by any rf time varying components. In the presence of the electric fields, the argon atom can polarize and instantaneously produce a dipole moment (μ):

$$\mu = \alpha_{Ar} |E| \quad [2.4.15]$$

where $E = E_{RF} = E_0 \cos(\omega t)$ outside the sphere of influence and $E = E_p = Q_p / 4\pi\epsilon_0 r_p^2$ inside the sphere. Outside the sphere of influence, the polarization of the argon atoms is switching at the frequency $\omega = 13.56$ MHz and has no net effect on the transport of argon atoms in the bulk plasma. Inside the sphere of influence, it is assumed that almost every argon atom polarizes and remains so until reaching the particle. To validate this last concept, a criterion for the size of the sphere of influence must be established and the probability that the polarized molecule does not de-polarize must be evaluated.

The boundary of the sphere of influence is determined by equating the two fields acting on the argon atoms where E_{rf} is the outside time varying field, and E_p is the field radiated from the charged particle.

$$E_{rf} = E_p \quad [2.4.16]$$

which gives:

$$\frac{Q_p}{4\pi\epsilon_0 r^2} = E_0 \cos(\omega t) \quad [2.4.17]$$

The sphere has a time varying radius depending on the sign of $\cos(\omega t)$, but if the $\cos(\omega t)$ term is taken to be unity, then the radius is approximately equal to $(Q_p / 4\pi\epsilon_0 E_0)^{1/2}$. For a particle charge equal to 4.9×10^{-15} C in a plasma with a field strength of approximately

100 V/m, the radius of the sphere of influence is approximately 650 μm . If the field strength increases to 1000 V/m, then the radius of the sphere of influence decreases to 210 μm .

If it is assumed that every atom within the sphere of influence is polarized, it is possible to calculate the interaction potential between the charged particle and a polarized argon atom. The electrostatic force acting on the polarized atom can be determined from the interaction potential. A force balance on the polarized atom gives the velocity of the atom at the instant that it collides with the particle. The interaction potential, Γ_{*p} between the charged particle and the induced dipole is:

$$\Gamma_{*p} = -\frac{1}{2} \frac{Q_p}{r^2} \left(\frac{Q_p \alpha_{Ar}}{4\pi\epsilon_0 r^2} \right) \quad [2.4.18]$$

where α_{Ar} is the polarizability of an argon atom [51] in an electric field ($16.3 \times 10^{-25} \text{ cm}^3$) and r is the distance along the line of centers. The force due to this interaction is found by taking the derivative of Equation 2.4.18 with respect to the separation distance:

$$F_{n*}^c(r) = -\frac{Q_p^2 \alpha_{Ar}}{2\pi\epsilon_0 r^5} \quad [2.4.19]$$

where the subscript n^* refers to the polarized species and the superscript, c , refers to the force due to a collision.

The polarized atoms may de-polarize within the sphere of influence if they collide with other atoms. The mean free path, λ , of a gas molecule in the plasma chamber is:

$$\lambda = \frac{1}{\sqrt{2}\pi d_o^2 n} \quad [2.4.20]$$

where d_o is the molecular diameter and n is the gas concentration. At 10 mTorr, the mean free path is on the order of 5 mm, so it is not likely that random polarized molecule collision will occur at an appreciable frequency. Therefore, it is likely that once the atoms polarize in the presence of the particle, they will remain so until colliding with the particle.

By performing a force balance on the argon atom,

$$F(r) = m_r \frac{dv}{dt} = -\frac{\alpha_{Ar} Q_p^2}{2\pi\epsilon_o r^5} \quad [2.4.21]$$

the polarized atom's velocity can be determined as a function of distance away from the surface of the charged particle. The reduced mass of the system, m_r , is found by the resistive addition of the mass of the argon atom and the charged particle, and is

approximately equal to the mass of the argon atom. To solve Equation 2.4.21, the time derivative must be transformed into a spatial derivative:

$$\frac{dv}{dt} = \frac{dv}{dx} \frac{dx}{dt} = v \frac{dv}{dx} = \frac{1}{2} \frac{d(v^2)}{dx} \quad [2.4.22]$$

subject to the condition that at the boundary of the sphere of influence, r_o , the argon atom is at its neutral thermal velocity, v_n . The velocity of the argon atom as a function of separation distance is found to be:

$$V_{Ar} = \left[V_o^2 + \frac{Q_p^2 \alpha_{Ar}}{4\pi\epsilon_o m_{Ar}} \left(\frac{1}{r^4} - \frac{1}{r_o^4} \right) \right]^{1/2} \quad [2.4.23]$$

Equation 2.4.23 is plotted in Figure 2.4.2 assuming an initial molecular velocity, V_o , equal to the neutral thermal velocity and assuming that the initial polarization occurs at approximately 170 μm away from the center of the particle (radius of sphere of influence at $E_o = 1500 \text{ V/m}$).

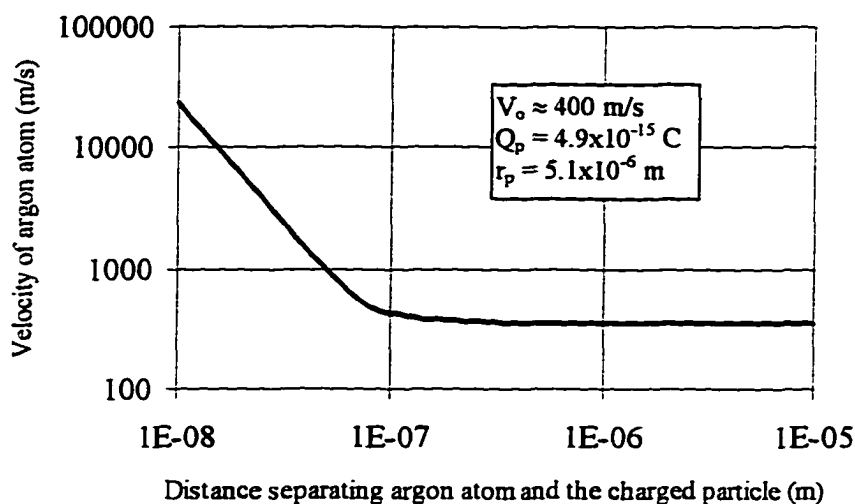


Figure 2.4.2 Velocity of polarized argon atoms interacting with a negatively charged particle

The velocity of the polarized atoms at the point of collision exceeds the neutral thermal velocity. Therefore, it is reasonable to assume that the neutral collision force will be enhanced by electrostatic interactions between the charged particle and the polarizable argon atoms. The probable velocity of the polarized argon atom approaches the Bohm velocity upon collision with a charged particle.

To obtain an estimate of the force imparted on the particles due to collisions with polarized argon atoms, the ion collision force, Equation 2.4.5, can be modified to reflect the fact that polarization greatly increases the concentration of molecules undergoing electrostatic interactions with the particle. It is assumed that the collision cross section for a polarized argon collision with a charged particle increases beyond the geometric cross section (used for a neutral collision) because of the electrostatic interactions and is

identical to the ion-particle collisional cross section. The maximum force occurs if all of the polarized species impact the particle surface at the Bohm velocity. The force acting on the particles due to polarized molecule interactions in a constant field is approximately 9×10^{-8} N, and is uniform over the surface of the particle. This is a 350X enhancement over the magnitude of the neutral, un-polarized argon atom collision force. The force is very strong but it does not contribute to the overall location of the particle because it is a uniform force. This force may be important for determining the Brownian motion of the particle. Furthermore, this interaction may be important in describing the instantaneous surface potential on the particle and in performing thermal analysis to predict the temperature of the particle which are important issues but are not explored in this research.

2.4.7 Thermophoretic Forces

The thermophoretic force is a result of a hot particle trying to come into equilibrium with the surroundings. Experimental evidence [26] suggests that by cooling or heating the electrodes, the particles can be moved. Graves and Daugherty [52] have performed experiments showing that metal particles immersed in a plasma are about 75 K above the neutral gas temperature. They attributed this effect to exothermic ion-electron recombination reactions on the surface of the particle, energy transfer from ion collisions,

radiation, and Knudsen cooling. If the chamber walls are at the neutral gas temperature, the warm particle experiences a force:

$$F_t = d_p^2 p \lambda \frac{\nabla T}{T_p} \quad [2.4.24]$$

where d_p is the particle diameter, p is the chamber pressure, λ is the mean free path, T_p is the particle temperature, and ∇T is the applied temperature gradient. If the particle temperature is 375 K, the magnitude of the thermal force as a function of the applied temperature gradient can be plotted (Figure 2.4.3). This force is somewhat large relative to the other forces observed thus far and is highly dependent on the applied temperature gradient. The force can be considered uniform over the surface of the particle assuming a uniform temperature gradient extending radially outward from the particle, although it is directional if there exists unequal temperature profiles along the chamber walls.

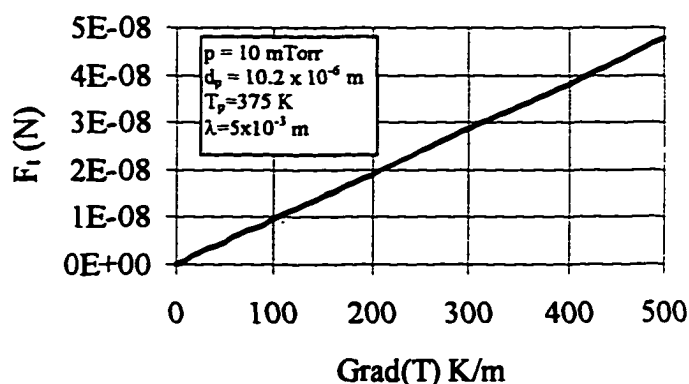


Figure 2.4.3 Thermophoretic force versus applied temperature gradient.

2.4.8 Neutral Drag Forces

Another force acting on the particles is the drag force associated with the directed flow of gas past the particle:

$$F_d = \frac{3\pi\mu_g(u - v_p)d_p}{C_c} \quad [2.4.24]$$

where μ_g is the gas viscosity, u is the gas velocity, v_p is the particle velocity, and C_c is the non-continuum Cunningham correction factor, which is given by:

$$C_c = 1 + \frac{2\lambda}{d_p} \left[1.257 + 0.4 \exp\left(\frac{-1.1d_p}{2\lambda}\right) \right] \quad [2.4.25]$$

The Cunningham correction factor is very large, on the order of 3000 for a chamber pressure of 10 mTorr. The argon gas viscosity is determined from the kinetic theory of gases, and is found to be 7.5×10^{-10} Pa-s. If the particles are in a quiescent medium, the drag force is on the order of 2×10^{-19} N assuming a particle velocity of 1.8 cm/s [53]. In order for the drag force to balance gravity, or any other force of similar magnitude, the gas velocity must be on the order of 2×10^7 m/s. This velocity is very large and at first glance unreasonable. It is justified because at 10 mTorr, there are simply not enough gas

molecules in the path of the particle to slow it down. The effect of drag becomes more important at higher pressures (~ 1 Torr) as seen in other microelectronics applications, but is not an issue for the low pressure applications like plasma etching. The drag force acts to oppose the motion of the particle in the quiescent medium.

2.4.9 Summary of Forces

Two types of forces acting on the particles have been evaluated thus far: those that are uniform across the surface of the particle, and those that are directional. The directional forces are the forces due to electrostatic interactions, gravity, ion collisions, fluid drag, and thermophoresis (depending on the structure of the temperature gradient). The continuous forces are ion orbital, neutral collisions, polarized collisions, and thermophoretic forces (again depending on the structure of the temperature gradient). For the experimental conditions listed in Chapter 2 and for $10.2 \mu\text{m}$ PSL particles, the strongest contributors to the location of the trap (directional forces) are electrostatic (8×10^{-12} N), gravitational (5×10^{-12} N), and ion collisional (3×10^{-12} N), assuming no applied temperature gradient. Balancing these forces indicate that the location at which the particles are trapped must have an electric field strength of at least 1500 V/m. The relative importance of the directional forces changes as a function of particle size indicating that smaller or larger particles will likely trap in locations slightly different than the $10.2 \mu\text{m}$ particles. The directional forces are not important for describing how the particles will

move in a plasma, rather will only describe the most probable location where they will trap in the chamber.

The directional forces are small in comparison to the uniform forces imparted on the surface of the particle. For a 10.2 μm PSL particle, the uniform forces are: neutral collisional (2.6×10^{-10} N), polarized collisional (9×10^{-8} N), and ion orbital (3×10^{-11} N). The uniform forces provide possible explanations for why particles move in a plasma. The relative importance of each of these forces will vary with particle size. In the next section, the movement of the particles due to atom-particle collisions will be evaluated for PSL particles with diameters of 10.2 μm and 100 nm. The first proposed mechanism for particle motion is Brownian motion which is a continuum theory. The second proposed mechanism is based on billiard ball collisions of argon atoms and charged particles.

2.5 Brownian Particle Motion

The particles are observed to move in the particle trap and the movement generally appears to be random. It is important to understand how and why the particles are moving in the particle trap because this directly impacts how the particles agglomerate. Boufendi *et al.* have performed 1-D Laser Doppler Anemometer measurements of particles moving in the axial (vertical) direction in an ignited plasma [53]. They assumed that the particles are in thermal translational equilibrium with the surrounding gas and their movement is

Brownian. They propose that the velocity of the particle can be described by thermal energy considerations:

$$\frac{1}{2}m_p\langle v^2 \rangle = \frac{1}{2}k_B T \quad [2.5.1]$$

By measuring the average velocity of the trapped particles, assuming a temperature, and assuming a particle mass density, the size of the particle can be determined:

$$r_p = \left(\frac{3k_B T}{4\pi\rho_p\langle v_z^2 \rangle} \right)^{1/3} \quad [2.5.2]$$

They found experimentally that the root mean square velocity of particles generated in a plasma was 1.8 cm/s, assumed the particles to be amorphous silicon with a density of 1.9 g/cm³, and assumed a particle temperature of 300 K, resulting in a particle diameter of approximately 230 nm. They verified this prediction by checking the particle size using Transmission Electron Microscopy and had excellent agreement.

In this work, it is important to describe how the particles are moving rather than predict particle size. Equation 2.5.1 can be used to approximate the velocity of the particle given the particle density and size, and the gas temperature. For the PSL particles used in

this work, the expected velocity due to thermal energy considerations is shown as a function of particle radius in Figure 2.5.1.

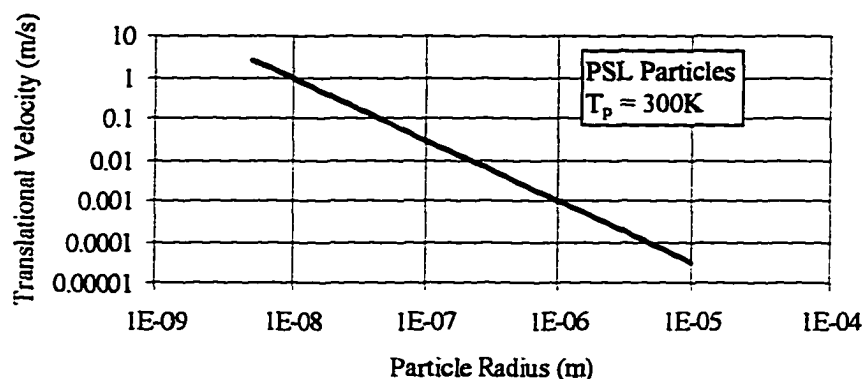


Figure 2.5.1 Translational velocity versus particle size assuming motion due to thermal energy considerations

As expected, this theory suggests that as the particles size increases, or as the particles get more massive, the translational velocity in any particular direction decreases. For the 10.2 μm PSL particles used in this work, the expected translational velocity is approximately 85 $\mu\text{m/s}$, which suggests that the probability of two large charged particles colliding is very small because the particles would never have enough kinetic energy to overcome electrostatic repulsive forces. It is expected that the average velocity of a 50 nm diameter PSL particle would be approximately 9 cm/s. At these velocities, it is very likely that the small particles can overcome electrostatic interactions and collide.

As suggested by Graves and Daugherty [52], the particle temperature might be 100 K above the neutral gas temperature. According to Equation 2.5.1, the particle velocity might extend up to 97 $\mu\text{m/s}$ for the 10.2 μm particle and 10 cm/s for the 100 nm

particle. The particle velocity from thermal energy considerations is not greatly effected by the range of expected particle temperatures. In Chapter 5, experimental evidence is presented showing that large trapped particles do move at appreciable velocities (much greater than the predicted 80-100 $\mu\text{m/s}$), and as a result other theories for explaining particle motion in a plasma chamber are necessary.

2.6 Atom-Particle Collisions

The forces suggested in Chapter 2.4 that act on the particle will contribute directly to the motion of the particle in the plasma chamber. The strongest of the forces presented is due to charged particle-induced polarized argon interactions. To obtain an estimate of the highest bound on the particle velocity, the polarized argon collision force is considered. This force is uniform over the particle surface, and the net force is zero; however at an instant in time, the instantaneous force due to a single collision is directional. Because this force is not continuous over very small increments of time (on the order of the inverse of the charged particle-polarized argon collisional frequency), a mean displacement of the charged particle from an initial point and the particle velocity can be determined. At the next instant of time, there is another particle-polarized argon collision which has the tendency to move the particle in a direction other than its original direction of travel. For each instant of time, the charged particle-polarized argon interaction can be described by a billiard ball collision. If a 10.2 μm PSL particle which

weighs approximately 5.83×10^{-13} kg is not initially moving has a collision with a polarized argon atom moving at the Bohm velocity, the maximum velocity that the particle will obtain is approximately 5×10^{-10} m/s assuming that all of the kinetic energy of the atom is transferred to the particle and that there are no energy losses as a result of the collision. The frequency of particle-polarized argon collisions is given by the flux of polarized argon atoms to the particle surface times the particle surface area:

$$v_c = n_n * u_b \pi r_p^2 \quad [2.6.1]$$

Assuming a polarized argon concentration equal to the neutral gas concentration yields a collision frequency of 1×10^{14} Hz, or one molecule strikes the surface of the particle every 1×10^{-14} s. If the particle instantaneously assumed the velocity of 5×10^{-10} m/s, it would take approximately 20 million instantaneous collisions along a single direction over the period of a microsecond for the particle to gain a velocity in excess of 1 cm/s as seen in [53]. The molecular collisions are not unidirectional, so it can be assumed that the movement of large particles due to polarized argon collisions is negligible.

The collision theory may be accurate in describing the motion of small particles. The 50 nm PSL particle is significantly impacted by a single collision with one polarized argon atom, approaching a velocity of 1.5 m/s if the polarized argon atom transfers all of its energy to the particle. The kinetic theory is valid in describing the motion of small particles which is reasonable because as the particle size gets smaller, it is more likely that

the particles will behave like a gaseous species. However, because the kinetic theory or the collision theory do not properly explain the motion of large particles in a plasma, it is necessary to develop a new particle motion theory. It is also necessary to determine over what size ranges that the kinetic theory or the new theory will dominate particle motion.

2.7 Coulombic Interaction

If the charged particles are allowed to interact coulombically while trapped in an equipotential region in the plasma, the monopole repulsive force acting on one particle relative to the other is:

$$F_{12} = \frac{1}{4\pi\epsilon_0} \frac{Q_{p,1}Q_{p,2}}{x^2} \quad [2.7.1]$$

where x is the separation distance in meters and Q_i is the charge on particle (i) in Coulombs. Consider the following scenario: at some initial time, two charged particles are infinitely separated from each other. Assume that the particles are both moving in the system and begin to approach each other. At some time, t_0 , the particles are positioned a distance x_0 away from each other. The particles are both charged negatively, so as they move closer together, they will tend to repulse each other. The position, x_0 , is taken to be the separation distance at which the particles will both have a zero velocity with respect to

each other before changing directions and traveling away from each other. The goal of the present theoretical development is to evaluate the velocity of the electrostatically interacting particles as a function of distance away from each other given an initial separation of x_0 .

If it is assumed that the localized region where the particles trap has a constant electron energy, density, potential, etc., then the charge on each particle is constant. Performing a force balance on the particles yields:

$$m_p \frac{dv^2}{dx} = \frac{1}{4\pi\epsilon_0} \frac{Q_p^2}{x^2} \quad [2.7.2]$$

The coordinate system is referenced to the center of particle 1, so $V_1 = 0$, and V_2 is the velocity relative to particle 1. In this model, only one-dimensional interactions between the two particles are considered. Equation 2.7.2 is subject to the boundary conditions that at some instant of time, the particles are located a distance x_0 away from each other and the velocity of particle 2 is zero, which is referring to the point at which two particles that are approaching each other change directions as a result of repulsive interactions.

The velocity of particle 2 with respect to particle 1 is found by solving Equation 2.7.2:

$$v_2 = \left[\frac{Q_p^2}{4\pi\epsilon_0 m_p \lambda_D} \frac{1}{x^*} \left(\frac{x^*}{x_o^*} - 1 \right) \right]^{1/2} \quad [2.7.3]$$

where x^* and x_o^* are the separation distances normalized to the Debye length, λ_D . Experimental techniques for measuring particle velocity do not allow measurement of one particle with respect to another particle. The absolute velocity of particle two or particle one (which is the negative of the velocity of particle one) referenced to a fixed point in space is found by multiplying the right hand side of Equation 2.7.3 by 1/2. Once the average velocity of a particle is known, it is possible to explore a variety of conditions where important parameters are varied. For example, it is possible to determine the effect of particle size, which will allow for a direct comparison to the thermal energy motion of a particle as proposed by Boufendi *et al.* [53], as well as the effect of initial particle separation distance. It is assumed initially that the plasma parameters do not change as a function of the size of the particle. The assumption of constant plasma parameters can be relaxed and will be investigated further in Chapter 5.7.

If the closest point of approach is a Debye length (the point where two particles traveling towards each other come to rest and then change directions of travel), the velocity of particle two once it has traveled a second Debye length away from particle one due to repulsive interactions can be determined as a function of particle size. Particle size factors into Equation 2.7.3 through the particle mass, m_p , and the particle charge, Q_p .

Figure 2.7.1 shows the velocity of particle two as a function of particle size given a 4 eV argon plasma at 10 mTorr with an electron and ion concentration of 10^{16} 1/m^3 .

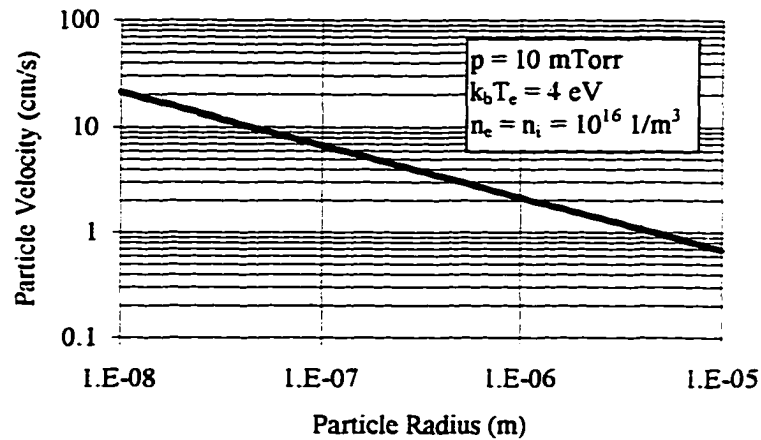


Figure 2.7.1 Particle velocity versus PSL particle radius predicted by Coulomb interactions

Recall that Boufendi *et al.* [53] have previously reported that the axial mean square velocity of particles in their system is approximately 1.8 cm/s. They reported an average electron temperature of 3 eV, a chamber pressure of 0.12 Torr, an electron density of $6 \times 10^8 \text{ 1/cm}^3$, from which a Debye length of 528 μm is calculated. Figure 2.7.2 is the predicted velocity as a function of particle size using the Coulomb theory and the thermal kinetic energy theory (Equation 2.5.1) for the experimental conditions used by Boufendi *et al.* They report a particle diameter of $230 \pm 60 \text{ nm}$ using Transmission Electron Microscopy and this is reflected by the dotted lines.

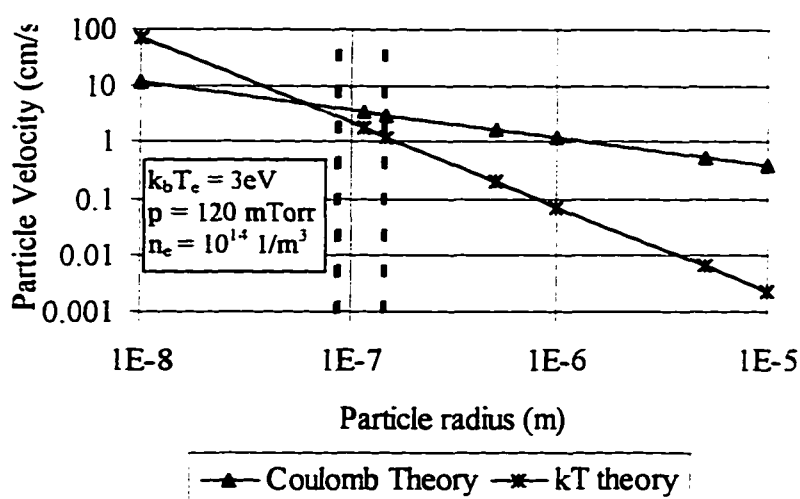


Figure 2.7.2 Comparison of the Coulomb theory and the kinetic energy theory to explain the experiments of Boufendi *et al.* [53].

The predicted velocity range for the thermal kinetic theory is 1.3-2.9 cm/s and the velocity range for the Coulomb theory is 3.1-4.1 cm/s. There is reasonable agreement between the two theories, and for the given experimental conditions, both accurately represent the data. It is important to note that complications in predicting the velocity reported by Boufendi *et al.* may be due to using a one dimensional model when the particles are actually moving in three directions. If the model is assumed to be correct, than the accuracy of the reported plasma parameters and particle velocity may come into question. Specifically, Boufendi *et al.* report a root mean square particle velocity of 1.8 cm/s, however their data (Figures 2 and 3 in [53]) span velocities between ± 5 cm/s. By averaging all of the positive and negative values of velocity, they end up with a smaller root mean square velocity than if they averaged just the positive velocities together and just the negative velocities together. In Chapter 5.5, it will become evident why averaging

only the positive or negative velocities is more representative of the average particle motion than averaging both the positive and negative values together. To this end, the predicted velocity of the particles using the Coulomb theory is in excellent agreement with the experimental data in [53].

It is clear in Figure 2.7.2 that for very small amorphous silicon particles having diameters less than a tenth of a micron, Brownian motion as described by the continuum kinetic theory is the mechanism governing particle motion. For particles larger than a tenth of a micron, the coulomb electrostatic particle interaction theory appears to be the dominating mechanism. The transition from one mechanism to another will depend on the density of the particle. Experimental evidence is presented in Chapter 5 which reinforces the fact that the Coulomb theory is the appropriate mechanism for describing large particle motion in a plasma.

The Coulomb theory particle velocity used in the above comparison with the kinetic theory is based on the velocity after a particle travels only one Debye length beyond an initial particle separation of one Debye length. It is important to evaluate the velocity as a function of separation distance for various initial separations (or closest points of approach). Figure 2.7.3 shows the predicted velocity behavior of two charged particles at various initial separations (denoted by the point where the velocity equals zero) for 10.2 μm PSL spheres in a 4 eV argon plasma. Note that for initial separations less than a Debye length, the particles initially accelerate to very high velocities and are repulsed from each other. This means that the particles must have a high kinetic energy

when traveling towards each other in order to initially approach closer than a Debye length before changing directions. When the particles do repulse each other, the electrostatic interactions will be very strong resulting in high departure velocities. The Coulomb model does not allow for induced electromagnetic dipole interactions to occur between the particles if they approached closer than a Debye length. Induced dipole interactions could cause the particles to attract one another instead of repulse each other.

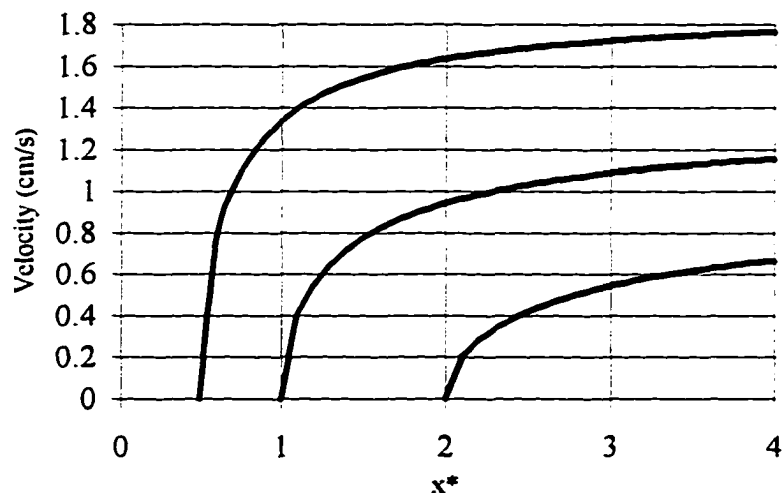


Figure 2.7.3 Particle velocity versus separation distance for 10.2 mm PSL particles in a 4 eV argon plasma

In order to account for the induced dipole interactions between particles, a different interaction potential must be used. A modified Kihara interaction potential [54] might be appropriate for describing repulsive interactions if the particle spacing is beyond a Debye length and attractive interactions if the particle spacing is within a Debye length. The

modification would have to account for the fact that the particles interact electrostatically with a r^{-4} dependence instead of due to dispersion which has an r^{-6} dependence. For separation distances much greater than the Debye length, a particle would tend to stay in motion until it approaches the field of another particle which would cause it to decelerate, come to rest, and then accelerate off into another direction. If the particle exhibited a low kinetic energy, interaction with another particle would cause it to stop well short of a Debye length from the center of the second particle. If the particle had a very large kinetic energy, it could overcome the potential field of the second particle and collide with it.

2.8 Coulombic Particle Theory

Ikezi [55] theoretically predicted that the charged particles trapped in the plasma could order and form lattice structures. These structures are analogous to how matter is classified: Coulombic gases have no long or short range order, Coulombic liquids have short range order, and Coulombic solids have long range order. This phenomena was not experimentally observed in a laboratory plasma until just recently in 1994 by Thomas *et al.* [56] and Chu and I [57]. Coulombic interaction with particles in a laboratory plasma parallels particle interactions in space (i.e. Saturn's rings, the tails of comets, etc.). This phenomena is not only of academic interest, but has substantial relevance to industrial applications. Particles in a Coulombic solid are fixed in space, and therefore cannot collide with a neighboring particle. Particles in a Coulombic gas move randomly and do have the

opportunity to collide with a neighboring particle leading to particle agglomeration. Understanding under what experimental conditions a Coulombic gas, liquid, or solid will occur may help in determining final morphologies of contaminant particles in a plasma [58].

Transitions between the Coulombic structures (called Coulombic melting) can be described by a dimensionless coupling parameter [59], β :

$$\beta = \frac{Q_p^2}{4\pi\epsilon_0 dk_B T_p} \quad [2.8.1]$$

which relates the kinetic energy of the particle to its coulombic energy. In Equation 2.7.1, d is the interparticle spacing and T_p is the particle temperature. The critical value for the coupling parameter at which a transition from a Coulombic liquid to a Coulombic solid has numerically been observed to occur at $\beta = 172$ [60].

2.9 Summary

Understanding the conditions under which the particles will collide and agglomerate is critical for predicting the morphology of the contaminants in the plasma. It has been shown theoretically that the polarization of argon and subsequent electrostatic interaction with a nearby charged particle is important in characterizing total species flux

to the surface of the particle and the transfer of energy to the particle. The particle-polarized argon kinetic energy transfer mechanism is important for describing the motion of small particles (less than $0.1 \mu\text{m}$ diameter), however, cannot explain the experimentally observed motion of large particles (greater than $0.1 \mu\text{m}$ diameter) trapped in a plasma. In an attempt to explain experimental observations of large particles, the coulombic interaction theory has been suggested. In this thesis, experimental evidence is presented which will suggest that the Coulomb particle interaction mechanism is appropriate for describing the motion of large particles in a plasma, and hence governs particle agglomeration.

CHAPTER 3

Experimental Diagnostic Theory

The process of experimentally characterizing the electrical and chemical properties of a plasma remains an arduous task despite the considerable efforts of numerous researchers. One critical reason that explains the difficulties of experimental characterization studies is that the capacity of current diagnostic tools to measure properties of the plasma is quite limited. For example, a set of diagnostic tools used to study gas phase chemical reactions often cannot be used in a plasma environment. This may occur for several reasons, including the presence of an rf electric field, the chemical reactivity of the plasma, and the ability, or lack thereof, to measure isolated properties of a plasma. Many fundamental properties of the plasma, i.e. electron energy distribution function, electron density, positive and negative ion density, and free radical concentrations are highly coupled in a nonlinear fashion resulting in difficulties in establishing basic experimental correlations with these properties.

To date, the diagnostic tool set that can be used to characterize plasmas has produced a very limited quantity of usable data. An immediate consequence of this is that it remains difficult to verify plasma models. Additionally, it is readily seen that the

“design” of a plasma from a verified fundamental perspective remains to be performed. In this context, “design” is referring to the engineering design of a chemical process which is typically performed on any critical manufacturing process, chemical process, or otherwise. This results in plasma processes which are highly inefficient and not fully optimized. Another important implication of interest to this research is that the limited ability to study plasma chemistry has prevented necessary advances in studying plasma induced particle formation and associated issues with micro-contamination.

This chapter will discuss the basic theoretical properties of the diagnostic tools that are used in this work. Chapter 3.1 will discuss the fundamental aspects of Optical Emission Spectroscopy. In Chapter 3.2, Laser Light Scattering techniques will be reviewed. Chapter 3.3 will discuss the laser Doppler technique that is used to study particle-particle interactions in a plasma.

3.1 Optical Emission Spectroscopy

Light emission is a characteristic feature of plasmas, the color of which can be used to identify the type of processing gas that is used in the chamber. Some of the atoms and molecules in a plasma are in the excited state as a result of a previous collision with an electron, a collision with another atom or molecule, or a dissociative chemical reaction. Independent of why the atom or molecule is in the excited state, the electron in the excited orbital will eventually decay to a ground state orbital. To account for the energy loss in

such a transition, an energetic photon is emitted whose wavelength is characteristic of the electron energy transition, according to the Bohr equation:

$$\varepsilon = h\nu \quad [3.1.1]$$

where ε is the energy of the emitted photon (which is equal to the energy of the electron in an upper orbital level minus the energy of the electron in a lower orbital level), h is Planck's constant ($h = 6.6262 \times 10^{-34}$ J-s) and ν is the classical frequency [61]. The photon wavelength is related to the frequency by:

$$\lambda = \frac{c}{\nu} \quad [3.1.2]$$

where λ is the wavelength, and c is the constant speed of light. If it is possible to collect the emitted photons and identify the associated wavelengths, it is possible to then calculate the energy transition that led to the emission of the photon. It is fortunate that the energy transitions of atomic species are discrete and unique, in that an electron orbital transition for argon has a specific energy that is not exactly shared by orbital transitions with other atomic or molecular species. This makes species identification possible from spectroscopic measurements.

3.1.1 Atomic Emission

In this chapter, the generation of the emitted photon is discussed along with spectroscopic interpretation. Many excellent introductory texts are available in this area [62]. The reader is encouraged to refer to these texts for a formal discussion of atomic and molecular emission.

An atom in its ground state is defined by all of its electrons existing in their lowest energy state configurations. If the atom undergoes a collision with another atom, another electron, a photon, or any other body, it is possible that the atom will gain energy. This energy is stored by transferring an outer electron existing in a ground state to a higher energy level. Recall that the energy transitions of electrons are quantized, so the electron transition is a result of a discrete energy transfer. For most cases, the excited electron is not stable in the higher energy configuration, and will eventually decay back to the original ground state configuration. The associated energy loss is balanced by the emission of a photon. A schematic energy level diagram is given in Figure 3.1.1. Represented are five possible cases. In case (a), an excitation results in an electron being promoted from the E_0 to the E_1 energy level. This is followed by a subsequent electron decay and a photon emission. In cases (b), (c), (d), and (e), the electron is promoted to the E_3 energy level. Each of the five cases represents a probability of electron decay. The electron can cascade down successive energy levels as shown in cases (b), (c), and (d), resulting in multiple

photon emission. Additionally, the electron can decay immediately back to the ground state, (e).

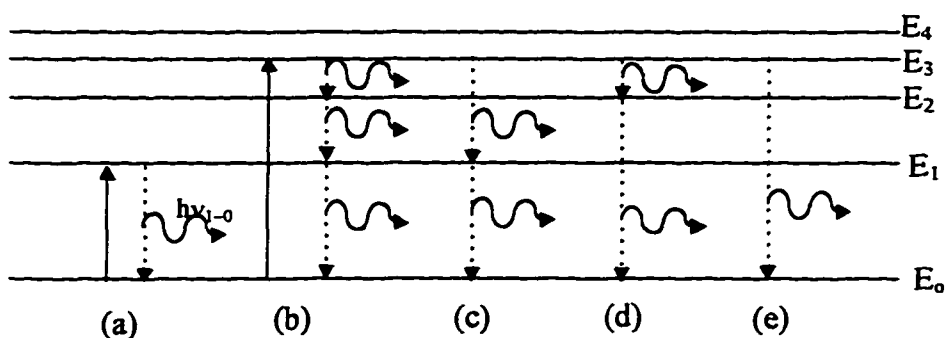


Figure 3.1.1 Schematic energy level diagram depicting quantized excitations and decays
 (a) single excitation, one photon emission
 (b) multi-level excitation, three photons emitted
 (c,d) multi-level excitation, two photons emitted
 (e) multi-level excitation , one photon emitted

The probability or possibility of each of the decay occurrences is determined by a set of selection rules [62]. The multiple emission of photons from cascade events results in very complicated emission spectra. In the case of a plasma excited argon gas, over 150 emission peaks are observed in the optical range (200-800 nm) [63]. A representative argon emission spectra is depicted in Figure 3.1.2 accompanied by Table 3.1.1.

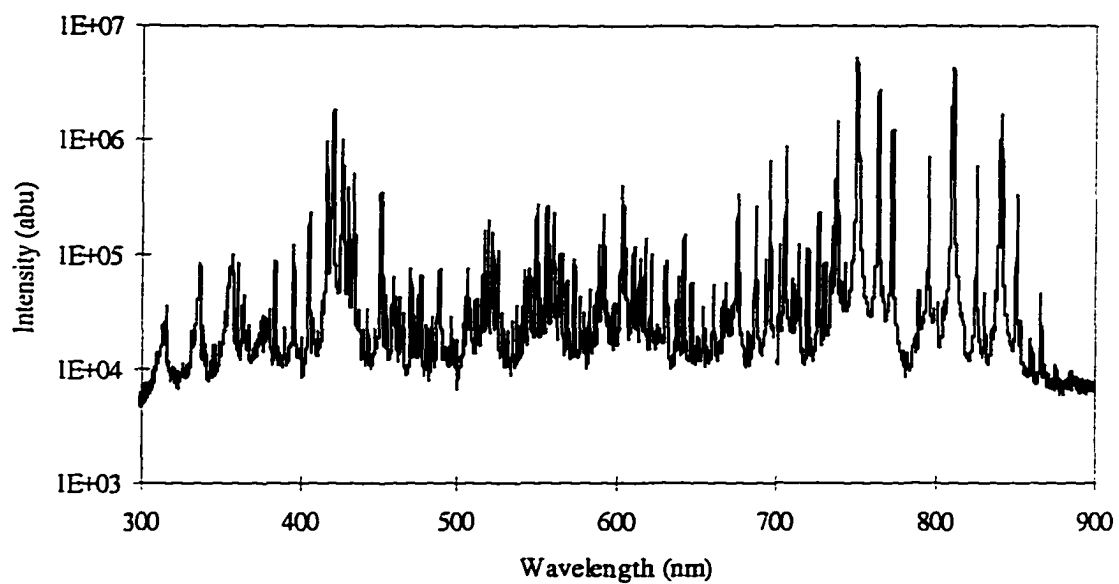


Figure 3.1.2 Representative argon emission spectra, 50 sccm (standard cubic centimeters per minute), 15 mTorr, 200W

Table 3.1.1 Argon emission intensities and peak locations for Figure 3.1.2

Wavelength (nm)	Intensity (abu)	Wavelength (nm)	Intensity (abu)
315.569	37090	511.881	41372
336.859	85352.5	515.183	67973
355.506	79956.5	516.118	163794
357.268	100627	517.767	49388.5
360.645	85356.5	518.772	197629.5
363.889	36889	522.075	153102.5
365.05	45039	525.233	108583.5
380.32	34028	537.294	36696.5
383.55	90251.5	541.027	35191
395.002	121917.5	542.175	72263
404.48	229373	544.185	60458
415.805	947331.5	545.19	76644.5
418.128	5255333	545.765	65316.5
419.000	579326	549.641	273566.5
419.871	1855325	550.646	96579
425.098	147805.5	552.513	41587.5
425.824	994608.5	553.518	35275.5
427.131	601631.5	555.958	259795
429.89	383663.5	557.251	122214.5
430.18	235562	558.973	37095
433.375	504289	559.835	83301
434.536	149763.5	560.696	230880.5
451.089	343889	562.276	39144
459.656	64557.5	563.999	43433
462.85	42503.5	535.147	99487.5
470.255	75513	566.009	35708.5
475.337	44570	568.306	46679
476.79	67932.5	569.024	58525
487.825	73608	574.049	90777.5
488.841	74738	577.351	42744.5
504.989	43448.5	580.366	31320.5
506.138	74045.5	583.525	50098
507.286	41014.5	586.109	35980.5

Wavelength (nm)	Intensity (abu)	Wavelength (nm)	Intensity (abu)
588.981	123.965	693.933	90972.5
591.278	222479	695.353	49408.5
593.001	117644.5	686.63	673775.5
594.293	39659.5	703.062	123662.5
598.887	38434.5	706.57	893311.5
600.036	35778.5	710.639	62738.5
603.37	395792	712.463	54979
604.363	262372.5	714.568	123475
605.357	64636.5	715.691	40712
605.925	11084135	720.462	111250.5
609.189	37415.5	727.057	232419.5
609.899	86443.5	730.986	85849.5
610.609	116248.5	735.055	176611.5
612.738	42498	737.16	361139.5
614.583	93889.5	738.143	1453015
615.577	53201.5	741.089	58148
617.281	135812	742.354	57275.5
621.255	98353.5	743.335	76009
629.63	79259.5	750.211	5279315
630.766	789395.5	751.333	2729325
631.476	35123	756.385	39078.5
636.87	38818.5	763.401	2717065
638.431	63193	764.243	129582
641.554	148057.5	766.769	53345
616.664	56291	772.382	1213230
653.762	34462	789.221	47527.5
660.433	55444.5	794.834	691084.5
666.395	39508	801.525	37603.5
667.815	57066.5	804.992	38918.5
669.944	33032	809.985	2018725
672.073	36195.5	811.095	4242285
674.202	46288	826.074	602390.5
675.338	334975	831.345	45691.5
676.758	70780.5	837.864	48291.5
687.262	259055	840.499	989958
688.823	58885.5	842.164	1676745

If an energetic photon having an energy which will cause an energy transition (E_0 to E_1) collides with a molecule, depending on the cross section of that interaction, that photon can be absorbed. This is actually the underlying principle behind a technique called absorption spectroscopy. For emission spectroscopy, the photon is emitted from the atom and is collected in the spectrometer. This introduces the fact that the medium through which the emitted photons are traveling must be optically thin. In other words, the probability of the emitted photon interacting with another atom and causing a secondary electron excitation and subsequent photon absorption is low. If a photon is generated in the middle of a chamber, the optically thin approximation says that the photon will exit the chamber or will collide with the walls before it is absorbed by a neighboring atom. For low pressure chambers, this is a reasonable approximation. The nearest neighbor atom to the atom emitting the photon has a mean separation distance given approximately by the mean free path. Estimating the worst case scenario, the probability of a photon being reabsorbed by another non-excited molecule could be represented by the number of molecules in the optical path of the photon. If there were ten molecules in the way, then the chance of externally observing the photon might be one in ten. This is given by the ratio of the mean free path to the chamber radius, assuming that the generation of the photon is in the center of the chamber. For the experimental conditions used in the work, this worst case estimate is approximately 3%.

3.1.2 Molecular Emission

When two or more atoms join to form a molecule, the energy levels for the electrons become much more complicated. The electrons do not remain in their previous energy shells, but rather move into new energy level shells based on the properties of the molecule. The differences of discrete energy required for an electron to move to one energy level or to the next highest energy level are very small, resulting in a nearly continuous spectrum of energy transitions. The peaks in this spectrum are very broad and low in intensity compared to the atomic counterparts. Identification of the heavy molecular weight molecules is difficult and quantitative analysis is nearly impossible using emission spectroscopy. A preferable method for identifying heavy molecules is infrared spectroscopy where molecular vibrations and rotations are measured.

Emission spectroscopy still remains useful for the lighter molecular weight molecules, which in a plasma tend to be the free radical fragments of the larger, more stable parent molecules. These free radicals are difficult to detect with mass spectrometry because they are short lived, although they are detectable using emission spectroscopy. The only difficulty is that the position of the characteristic identification peaks must be known *a priori* to performing species identification. Both experimental and theoretical techniques have been used to determine where these peaks lie, however a concentrated effort in evaluating emission spectra for common semiconductor processing gases is lacking.

3.1.3 OES Instrumentation

Although there are many different methods for making spectroscopic measurements, in this work, only diffraction gratings were used and will be the only method discussed. The reader interested in a discussion of the various emission spectroscopic techniques in use today is referred to a summary written by A. Strasheim from the University of Pretoria, South Africa [64].

There are a few basic concepts to Optical Emission Spectroscopy which will be discussed here. In order to analyze the wavelengths of a light source, the light must be collected, split into an optic beam, collimated into a parallel beam, dispersed, refocused, and measured. The OES can be separated into three components: a light gathering system, a wavelength separation system, and a light measuring system.

The light source, in this case a plasma, emits light which passes through a quartz viewport, and enters an optic fiber. The optic fiber is a bundle of UV-grade fused-silica glass fibers covered by an opaque sheath that serves to transfer the light from the light source to the wavelength separation system. In this system, the light is passed through a slit in a plane which produces a narrow optic beam.

The light is reflected off a second plane with very narrow slits which cause the light to diffract. Constructive and destructive interference of the diffracted light causes dark and light bands to appear on a plane (Figure 3.1.3).

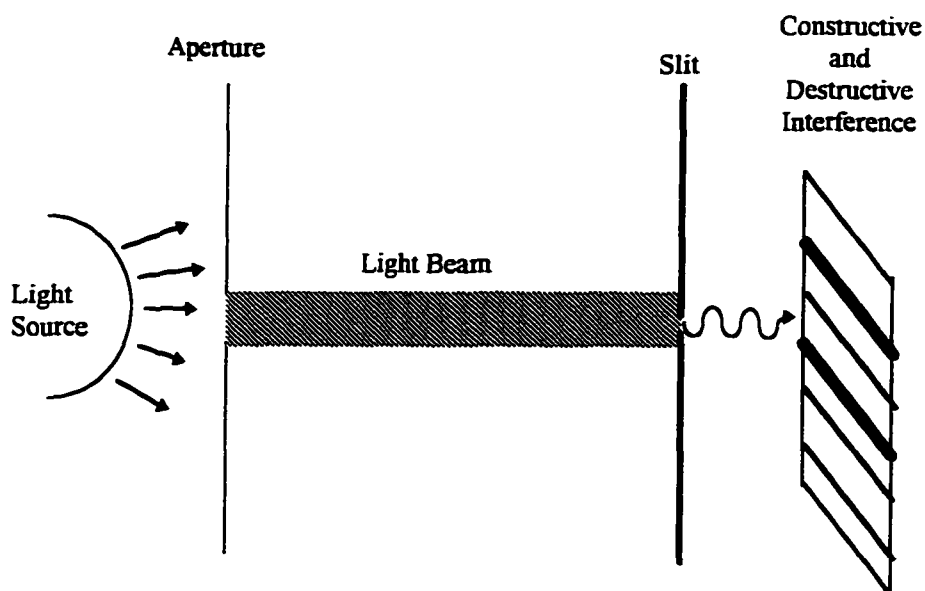


Figure 3.1.3 Diffraction interface

By passing the light through multiple slits in a plane (diffraction grating), it is possible to decrease the width of the light bands and increase the intensity per peak which results in increased resolution. The separation between the gratings is called a grating constant. The emission spectrograph used in this work is a triple spectrograph; the light source can be passed through one of three different diffraction gratings, depending on the desired resolution and width of a particular emission scan. For example, one of the diffraction gratings has 1200 slits per millimeter.

There are two methods for collecting the diffracted light. First, by scanning a lens system across the diffracted light pattern, each beam can be focused into a photomultiplier tube which converts the photons into an electrical current. The current is then amplified and the resulting signal is interpreted as the intensity of the particular band. This method requires a reliable traversing mechanism which has high positional accuracy. Additionally,

the photomultiplier method requires a finite amount of time to complete a particular scan. The second method is to direct the diffracted light onto a light detector which consists of a photodiode array. The narrow light beams will induce a current proportional to the beam intensity at the location on which the light falls on the photodetector. Likewise, the dark regions will cause no current on other parts of the detector. By reconstructing at what location on the photodetector a signal was generated, it is possible to determine beam intensity and location of the beam. This system requires no moving parts and allows a full spectrum scan (of a pre-selected width) to be instantaneously captured.

3.1.4 Instrument Resolution and Limitations

Resolution of an emission spectrometer describes the ability to distinguish two peaks that are very close in wavelength, and is defined as:

$$R = \frac{\lambda_{AVE}}{\Delta\lambda} \quad [3.1.4]$$

where λ_{AVE} is the mean wavelength of the two peaks, and $\Delta\lambda$ is the wavelength separating the two peaks. Resolution is operationally dependent on the quality of the optical system, slit dimensions, and number and size of gratings. Resolving power is typically reported as the full width of the peak at half of its maximum intensity (FWHM), where a smaller

FWHM indicates better resolution capability. There are some theoretical limitations to how small the FWHM can be which are related to laws of diffraction according to Equation 3.1.5:

$$\text{FWHM}|_{\text{Theoretical}} = \frac{\lambda_{\text{peak}}^2}{nd} (\sin i + \sin \theta) \quad [3.1.5]$$

where λ is the wavelength of the peak of interest, i is the angle formed between the original light beam and the normal to the grating, θ is the angle formed between the normal to the grating and the diffracted light beam, n is the total number of illuminated gratings, and d is the spacing between the gratings.

The efficiency of a particular grating is based on the ratio of diffracted light to the light reflected off of an aluminized mirror. The efficiency of the grating at a particular angle is related to the blaze wavelength or the blaze angle. The spectral range over which one can expect greater than 50% efficiency of the grating is given by:

$$\left(\frac{2}{2n_r + 1}\right)\lambda_b < \lambda < \left(\frac{2}{2n_r - 1}\right)\lambda_b \quad [3.1.6]$$

where λ_b is the blaze wavelength, and n_r is the refractive index [64].

The limitations in the application of optical emission spectroscopy can be reduced to problems associated with the plasma and to the chamber that contains the plasma. Although it is often assumed that the plasma is symmetric and isotropic, this assumption is not exactly correct. This assumption has been imposed in the literature in order to simplify numerical calculations. However, the emergence of new diagnostic techniques for characterizing plasmas have successfully invalidated the wide spread use of this assumption. Spatiotemporal Optical Emission Spectroscopy has been used to show emission profiles in a plasma discharge [17, 65]. Similarly, Kang reports average electron temperature and ion concentrations as a function of location for an inductively coupled Ar rf plasma in a GEC reference cell [23].

3.2 Laser Light Scatter

Laser light scattering techniques can be used to visualize particle traps and make rough quantitative measurements. An incident beam of light with intensity, I_{inc} , that intersects a particle will induce an electromagnetic field in the particle. The strength of the induced electromagnetic field is dependent upon the polarizability of the particle, α . The induced electromagnetic field will propagate radially outward from the particle, having an intensity, I_s . The scattered intensity can be related to the incident beam intensity [64]:

$$\frac{I_s}{I_{\text{INC}}} = k_s^4 \frac{\sin^2 \theta}{R^2} \alpha^2 \quad [3.2.1]$$

where $k_s = 2\pi/\lambda$, $\lambda = \lambda_0/n_{ri}$, λ_0 is the incident beam wavelength, and n_{ri} is the index of refraction and equals unity in free space, R is the distance from the center of the particle, and θ is the angle between the incident and scattered beam.

If there are multiple particles, N , in a sampled volume, V , the scattered intensity becomes:

$$\frac{I_s}{I_{\text{INC}}} = k_s^4 \frac{\sin^2 \theta}{R^2} \alpha^2 \frac{N}{V} \quad [3.2.2]$$

It is possible to measure particle concentration, C , by measuring the ratio of the forward and scattered light intensity:

$$C = \frac{N}{V} = \frac{I_s}{I_{\text{INC}}} k_s^{-4} \frac{R^2}{\sin^2 \theta} \frac{1}{\alpha^2} \quad [3.2.3]$$

This equation is simplified in that the scattered intensity dependence on particle size and the resolution of the imaging system is not accounted for. The concentration measured in Equation 3.2.3 is only along the path of the laser beam. In order to determine particle concentration information throughout the chamber, the laser beam must be moved or

rastered. Beam rastering may present some experimental challenges, so an alternative method to particle illumination throughout the entire chamber is to manipulate the beam into a laser sheet by using a cylindrical lens. This technique allows for a continuous illumination of the entire sample volume, although, the signal intensity diminishes, which ultimately limits the minimum detectable size of the particles.

Laser light scattering techniques do provide information about particle concentration, however data processing and analysis is extremely difficult. Furthermore, when making concentration measurements, it is difficult to ascertain whether the scattered light intensity is from interaction with a few large particles or many very small particles, unless the imaging cameras are sensitive enough to resolve 1 μm particles. In Figures 5.2.1-8, examples of Laser Light Scattering images are shown. It is readily seen that LLS is not a very powerful tool for making spatially resolved particle concentration measurements. An alternative technique is Laser Doppler Velocimetry, which allows for simultaneous measurements of local particle concentration and particle velocity in the plasma chamber.

3.3 Laser Doppler Velocimetry

Laser Doppler Velocimetry (LDV) is a diagnostic technique by which velocities of individual particles passing through a point in space can be determined accurately. This technique has seen substantial use in experimental fluid mechanics, and has only recently

been extended to more challenging environments, e.g. two phase plasma-solid flows. Since LDV is a new diagnostic tool for the study of particles in plasmas, the theory governing the technique will be discussed in detail. A brief explanation of the principles will be discussed followed by a more thorough discussion of the optics system, signal detection, signal quality, and processing. More than one technique exists by which the laser signals can be processed. The method discussed here will be specific to LDVs manufactured by Aerometrics, Inc.[67]. The system has some limitations which are important for applications with plasmas. The LDV system used for this work is equipped with the capability for Phase Doppler Particle Analysis (PDPA), which allows for the determination of particle size based on the assumption of a spherical particle. PDPA was not used in this work and will not be discussed here.

3.3.1 General Laser Doppler Velocimetry Theory

In order to measure one dimension of a particle velocity, it is necessary to intersect two laser beams. The second beam is typically shifted 40 MHz from the original by a Bragg Cell. The intersection of the beams defines an interferometric probe volume which is ellipsoidal in shape. If the two laser beams are linearly polarized, coherent, and Gaussian, their intersection will result in a pattern of constructive and destructive interference (Figure 3.3.1).

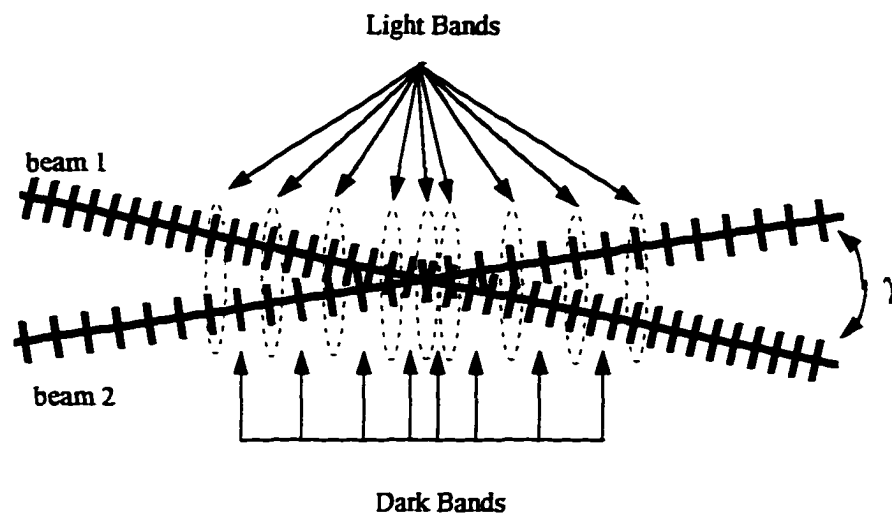


Figure 3.3.1 Laser beam intersection depicting constructive and destructive interference

If a flat plane were placed at the intersection region according to Figure 3.3.2, then a series of light and dark bands would be observed, giving evidence to the constructive (addition of light intensities) and destructive (canceling of light intensities). The fringe spacing (δ) between pairs of dark bands can be calculated:

$$\delta = \frac{\lambda}{2 \sin(\varphi / 2)} \quad [3.3.1]$$

where λ is the laser wavelength and γ is the beam intersection angle.

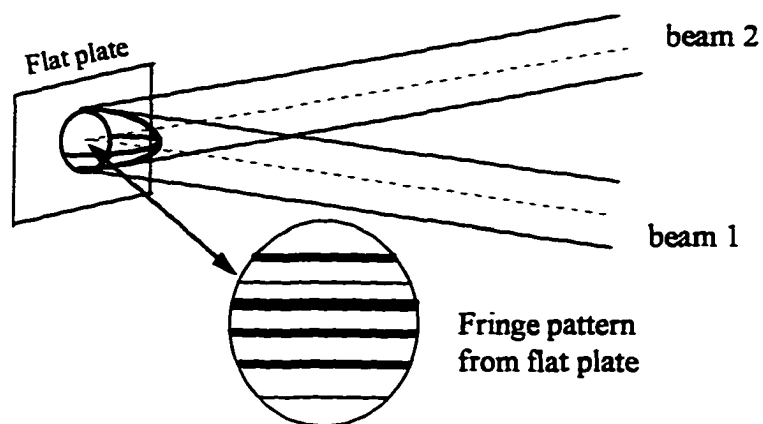


Figure 3.3.2 Intersection of probe volume with a flat plate

The laser intensity in the probe volume remains Gaussian as shown in Figure 3.3.3.

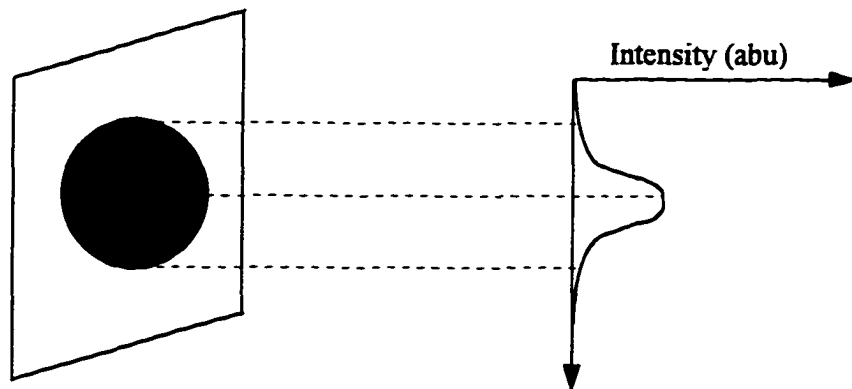


Figure 3.3.3 Gaussian intensity profile

If a particle traverses the interaction volume, it will pass through each fringe in the interaction volume resulting in an intensity maximum and minimum according to the angle of reflection off of the particle surface (Figure 3.3.4).

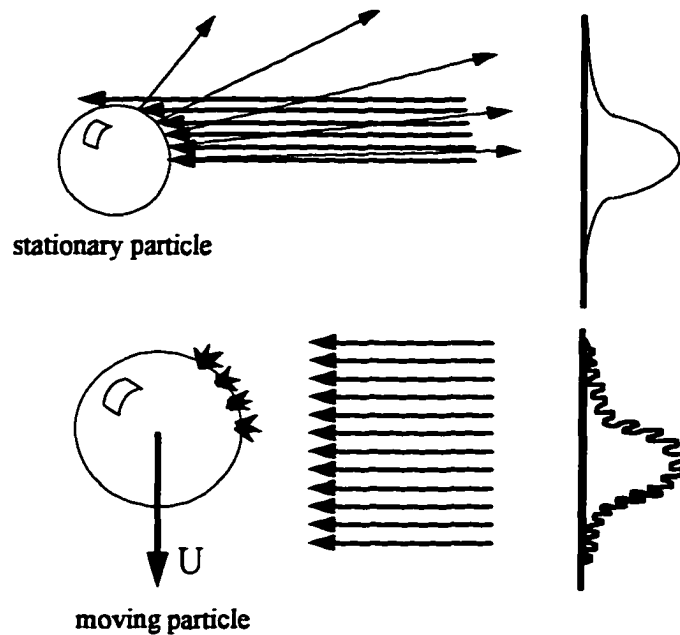


Figure 3.3.4 High frequency signal superimposed over the Gaussian signal from a particle moving at velocity U

The reflected optical signal is transmitted to the signal processor by a fiber optic cable which is converted to an electrical signal by a photomultiplier tube. If the electrical signal is passed through a high band pass filter, the Gaussian component of the signal is removed, resulting in a Doppler burst as shown in Figure 3.3.5.

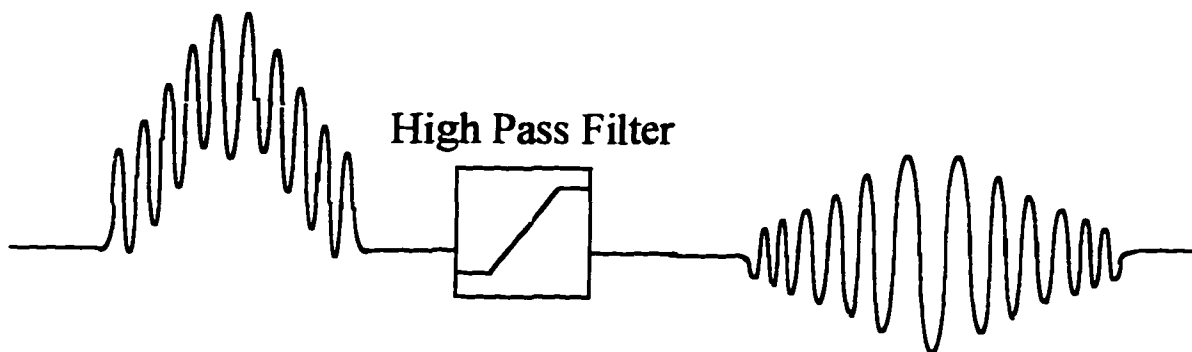


Figure 3.3.5 Signal processing to generate a Doppler burst

The temporal frequency (f) of this signal is related to the velocity (V_p) of the particles by multiplying by the fringe spacing according to:

$$V_p = f_i \delta \quad [3.3.2]$$

3.3.2 Extended LDV Hardware Theory

The previous chapter was an introduction to the principles of LDV measurement. In practice, velocity measurement is much more complex and therefore warrants further discussion. In this chapter, LDV will be described in the following order: laser requirements, optical manipulation, laser beam transmission, measurement, signal detection, and signal processing.

Recall from the previous discussion about atomic emission, electrons of excited atoms in the laser cavity tend to cascade down energy levels and emit multiple photons

having different wavelengths. For an unfiltered laser beam, there are many different wavelength lines coexisting with different intensities. The property of multiple wavelengths in the laser beam will be later utilized in the optics system so that multiple components of velocity can be measured simultaneously.

The laser beams that are used to establish the interference pattern must have temporal and spatial coherence. Temporal coherence exists if for all time or at any point along the path of the laser at any time, the phase and frequency of the beam is constant. Spatial coherence exists if the phase and frequency across the cross section of the beam are constant. Coherence is required to form an interference pattern which is needed in order to measure velocity as indicated in Equations 3.3.1 and 3.3.2. There is no way to guarantee that two beams could be intersected to form an interference pattern if the wavelength in Equation 3.3.1 was a function of distance along the laser beam.

An interesting note about the measurement capabilities of the LDV is that it is a single particle counter. In order to make a particle velocity measurement, it is required that only one particle pass through the interferometric probe volume at a time. Sankar *et al.* [68] have shown numerically that if two particles pass through the interferometric probe simultaneously, the superimposed scattered signal from the two particles will result in a signal that is virtually all noise and will not be detected by the electronic processors. In order to promote the case when only a single particle passes through the measurement volume at a particular time the size of the probe volume is reduced. This is done by focusing the laser beams and intersecting the laser beam pair at their respective beam

waists. At the beam waist, the electromagnetic waves will be parallel plane waves, which when intersected with another beam allow for sharp constructive and destructive interference patterns. These specifications for the interferometric probe volume mandate how the coherent laser beam, which starts out with multiple wavelengths is optically manipulated.

The original laser beam enters an optic system (called the 'Fiber Drive' on the Aerometrics LDV [69]) and is Bragg shifted by 40 MHz. The Bragg Cell uses acousto-optical frequency shifting to split the incident laser beam in half and shift the frequency of the second beam by electronically oscillating a piezo-electric crystal. The original beam and the second shifted beams are manipulated into a prism where the multiple lines of the original beam are separated into monochromatic lines of different wavelengths. Tiny mirrors are then used to pick off the desired monochromatic lines which are transferred to an optic coupler. Figure 3.3.6 is a schematic describing the optical manipulation system.

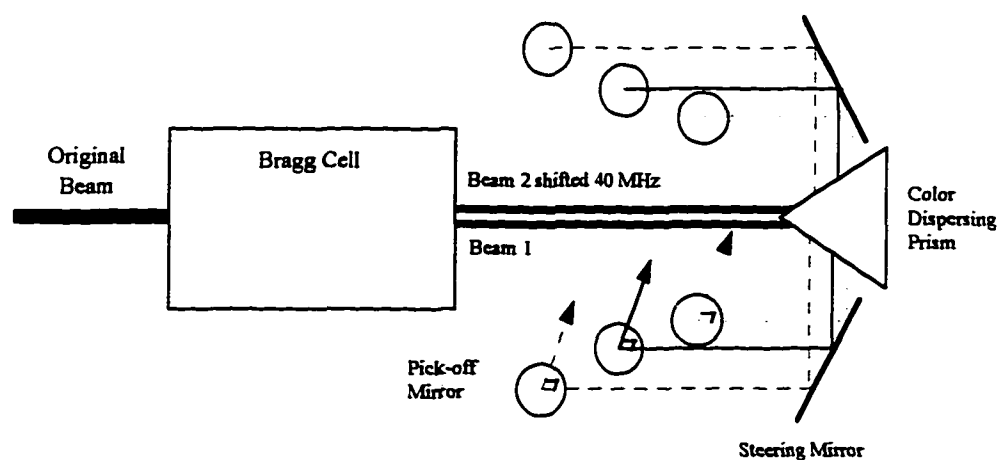


Figure 3.3.6 Schematic of optic manipulation in an Aerometrics Fiber Drive

The monochromatic lines are transferred to a transmitting lens system via fiber optic cables, one for each laser beam. The requirement of the optic fibers is that they maintain laser coherence during transmission. This is done by transmitting the laser beam in single mode through TEM₀₀ SMPP (Single Model Polarization-Preserving) fiber optic cables. The optic fiber which transmits laser light in only a single mode must have a diameter on the same order as the wavelength of the laser light. In order to couple the beam from the fiber drive with the 4 μm diameter optic fiber, fiber optic couplers are used. The couplers consist of a series of tunable mirrors which direct the beam into the optic fiber. The requirements of the couplers are that they focus the beam to a beam waist of no greater than 4 μm with a numerical aperture of 0.11. Typical efficiencies of intensity transmission are on the order of 50-60% for modern fiber optic coupling devices.

The two laser light beams (for 1-D LDV) exit the optic fibers in the transceiver. The beams are then crossed and focused at the crossing using a series of lenses. The axial distance to the crossover can be adjusted by changing the focal length of the final transmitter lens. One dimensional LDV theory is easily extended to measuring multiple components of velocity by adding pairs of laser beams aligned in the directions which will give rise to the appropriate velocity component measurement. When multiple components of velocity are to be simultaneously measured, different wavelengths for the laser pairs must be used.

The method of receiving the optic signal essentially happens backwards compared to that of the transceiver. There are a series of lenses and apertures to prepare the scattered light for transmission through a second optic fiber leading to a photomultiplier tube. The collected light is collimated and filtered so that only a monochromatic line having the appropriate wavelength used for each of the respective velocity components is transmitted to the appropriate photomultiplier tube.

The principle behind the photomultiplier tube (PMT) is that a beam of light containing energetic photons impacts a metal plate. If there is a voltage potential placed on the plate, then the electron excitation in the metal atoms due to photon interactions will result in a current. The intensity of this current can then be processed using analog electrical devices.

Recall from Figure 3.3.4, the signal due to a particle traversing the interferometric probe volume will have a Gaussian profile with a higher frequency signal superimposed. In order to measure the frequency, the signal is sampled using a fast Fourier transform (FFT). This is a very intensive computational method if high resolution is desired; 20 million frequency measurements per second are made using 32 measurement points per sample with each signal being measured four times and averaged to determine a final frequency [70]. A signal burst detector can be used to initiate FFT frequency measurement. Ibrahim and Bachalo [71] have measured the performance of numerous signal burst detectors, and as a result, have included a Fourier transform burst detector and an analog burst detector in parallel to determine and validate the presence of a particle and initiate frequency

measurement. The burst is considered valid only if the analog signal and the Fourier transform are both triggered simultaneously, otherwise the signal is rejected.

The raw frequency measurement is then sent to the computer for processing and regression. From the frequency measurement, the velocity is calculated. When multiple velocities are measured simultaneously, coincidence of measurements (two or more components of velocity measured for the same particle) is determined either by comparing the arrival of frequency signals to the computer or by comparing the times when the Fourier transform burst detector is activated for each of the directional velocity channels.

3.3.3 LDV Data Reduction

The velocity of a particle is calculated by multiplying the temporal frequency by the average spacing of the fringes. The velocity measurements are stored in bins so that a frequency of particles having a certain measured velocity is reported. The gate time is measured as the transit time for the particle through the measurement probe volume. The interarrival time is the time lapsed between measurements of particles in the measurement volume. The data rate is the total number of particles sampled divided by the total time of reaction.

Of interest to this work is the local particle concentration, the total number of particles in the plasma, and the average interparticle spacing. The literature demonstrates multiple ways for determining local particle concentration. One of the biggest difficulties is

determining what the measurement volume cross section is for the particular location which the particle passes. For dense particle clouds, the problem of determining local particle concentration becomes increasingly more difficult because the probability of more than one particle existing in the measurement volume increases. Recall, multiple particles in the measurement volume will not give a useful signal, so these particles are not counted, hence the measured concentration is much lower than the real concentration. This problem is avoided by making sure that the percent validation (particle signal / particle signal attempted) is in the range of 90% or higher. The first method [72] for measuring local concentration (C) in units of m^{-3} is given by:

$$C = \frac{1}{A_{mv} \bar{z}} \quad [3.3.3]$$

where, the average interarrival spacing (\bar{z}) is given by:

$$\bar{z} = \overline{V_z t_d} \quad [3.3.4]$$

where t_d is the interarrival time or time between particle arrivals to the measurement volume. The cross sectional area of the measurement volume (A_{mv}) is taken to be that of a circle [73, 74] having a diameter (D_{mv}) approximated by:

$$D_{mv} = \max[V(j) t_g(j)] \quad [3.3.5]$$

where $V(j)$ is the vector velocity field, and t_g is the gate time for particle i in the measurement volume. Equation 3.3.3 gives the interparticle spacing averaged number density. Alternatively, the concentration can be determined by:

$$C = \frac{1}{t_{tot}} \sum_i \frac{\sum_j t_g(i, j)}{PV_i} \quad [3.3.6]$$

where t_{tot} is the total measurement time, PV_i is the probe volume for a particle class i , and the summation over j accounts for each particle in a particle size distribution, j . Equation 3.3.6 is the method used by the LDV manufacturer and is the average over the gate time. The difficulty in calculating this is predicting the volume of the measurement probe for a particular particle class. This method was not used because it required using the PDPA so particle size could be measured. Finally, one can predict the concentration according to:

$$C = \frac{1}{\Delta t} \sum_i \left(\frac{1}{V_i A_i} \right) \quad [3.3.7]$$

which is a time averaged concentration for different size particles [75] assuming a uniform density of particles in time. The concentration is determined over all of the particle

velocities (V_i) having different probe cross sections (A_i) over a time increment Δt . Because a monodisperse particle was used, it was unnecessary to include any particle size class information in determining the particle concentration, hence the first method was used in this work to calculate the local concentration .

It is important to measure the particle concentration because it indicates how many particles are in a plasma trap, given the volume of the particle trap, which can be predicted with intensive modeling or by traversing a laser sheet through the trap and recording exactly where the particles are. Also, note the importance of the interparticle spacing (z). The average of this quantity indicates how far each particle is from its nearest neighbor. This is important when considering how the near neighbor particle distance compares with the Debye length, which indicates the length over which the particle Debye sheath extends.

CHAPTER 4

Experimental Setup

Numerous experimental modifications were made to the plasma chamber in order to accommodate the Laser Doppler Velocimeter. In this chapter, the base configuration of the system will be discussed in addition to basic operating procedures. The types of modifications that were implemented will be presented as well as the motivation behind each modification.

4.1 Base Configuration

The plasma chamber used in this research is a modified form of a Tegal MCR-1 RIE (Magnetically Confined Reactor, version 1, Reactive Ion Etcher). A general schematic of the chamber is shown in Figure 4.1.1.

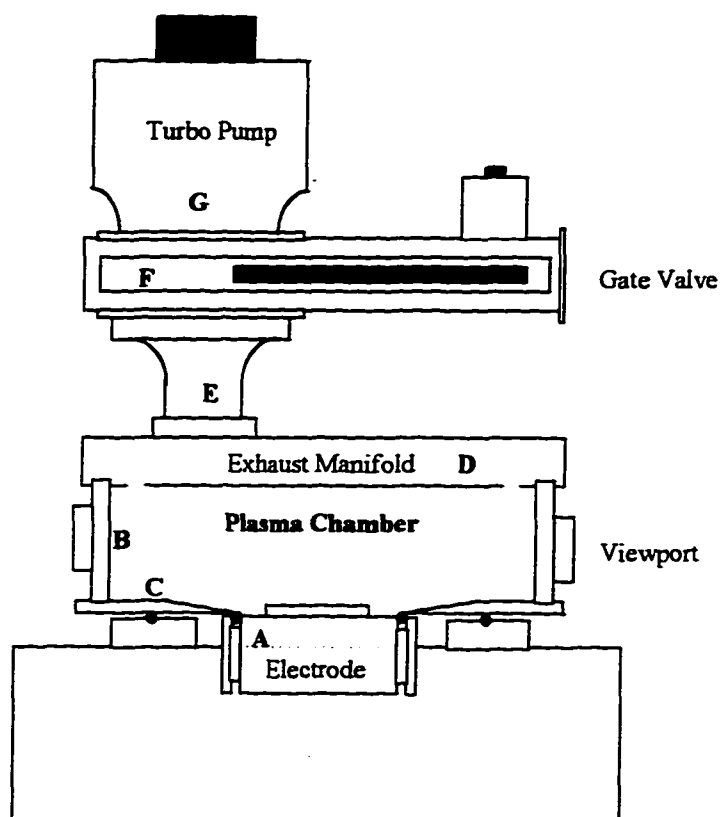


Figure 4.1.1 Tegal MCR-1 modified plasma etcher

The basis of this chamber is a Tegal 1511 four inch diameter, water cooled electrode (Part A in Figure 4.1.1). The electrode is machined from aluminum, and is vacuum sealed to the chamber by means of four o-rings. Due to the rapid advancement of the semiconductor industry and a necessity to use larger silicon wafers for increased product yield, the generation of four inch etch tools has quickly become obsolete. For general studies of plasma induced contamination, the tool is ideal and remains relevant.

The chamber shell is a custom designed stainless steel cylinder with a height of 11.8 cm., an internal diameter of 25.6 cm, and a wall thickness of 2.45 cm, (Part B). There

are four access ports located at 0° , 45° , 90° , and 180° . The ports are all welded to 4.5 inch MDC conflat flanges to which viewports can be attached and diagnostic equipment can be interfaced with the chamber. The custom shell does not have inserts where magnets could be placed in order to magnetically confine the plasma as was the case with the original un-modified chamber. Although this could result in a lack of plasma confinement, with proper grounding, this is not an important issue.

Between the chamber shell and the electrode is an electrically insulating disk made of macor (Part C). This disk serves three purposes. First, it provides a vacuum sealed interface between the four inch diameter electrode and the twelve inch shell. Second, it provides an electrical insulation between the powered electrode and the cylindrical shell which must be grounded. Finally, it serves as a process gas introduction stage. Figure 4.1.2 highlights the interface between the components and depicts how the gas is introduced to the chamber.

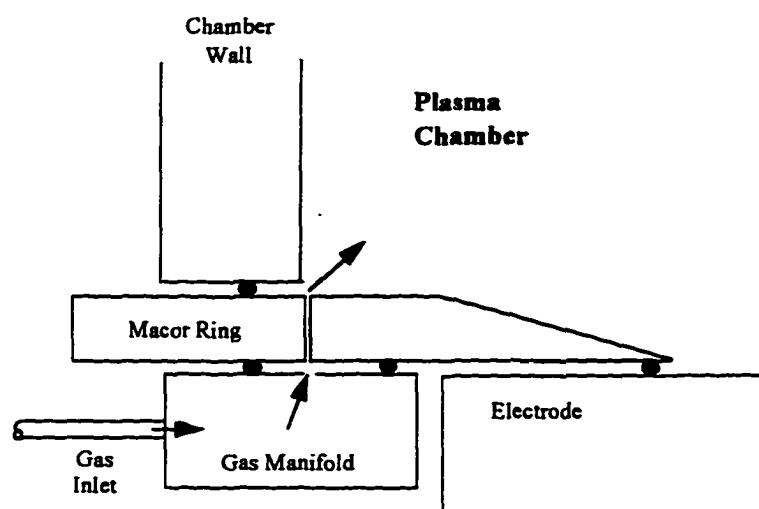


Figure 4.1.2 Gas flow path into plasma chamber

Above the stainless shell is a pumping stack manifold (Part D in Figure 4.1.1). The manifold interfaces the vacuum pumping units with the chamber. The manifold also serves as the grounded electrode for the plasma. The spacing between the powered electrode and the grounded electrode is 9.7 cm. The gas exits the chamber through the grounded electrode by means of four equally spaced slots having dimensions as indicated in Figure 4.1.3. The slots are covered with a steel mesh which serves to contain the plasma within the chamber, preventing any secondary plasmas in the manifold or pumping stack.

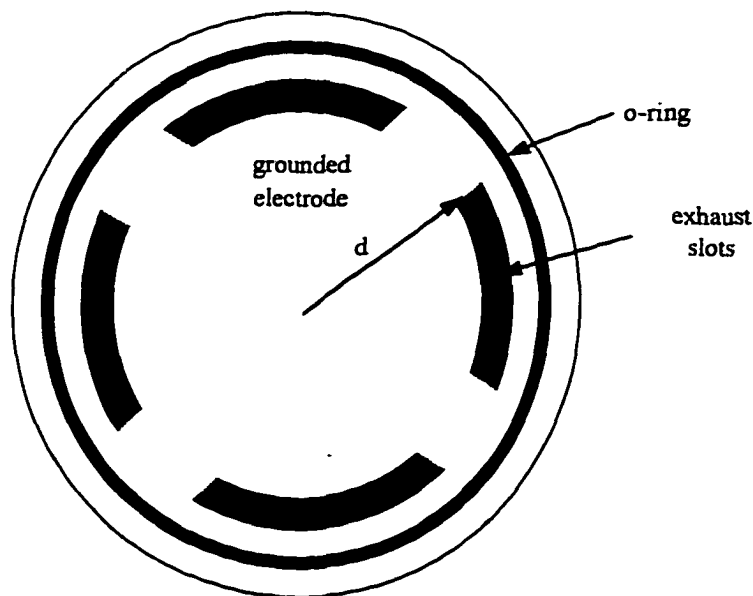


Figure 4.1.3 Gas exit slots in exhaust manifold

The gas exits the manifold off axis and enters the pumping stack (Part E in Figure 4.1.1) which serves to interface the chamber with the throttle control valve and the two stages of pumps. The throttle control valve (Part F) is a VAT model F 40425-01 which is

electronically manipulated in order to decrease pumping speed and increase pressure in the chamber. The chamber is evacuated by means of two pumps in series. A Leybold DC-30A mechanical pump is used to initially pump the chamber down from atmospheric pressure to the 100-200 mTorr range. The mechanical pump is lubricated with Dupont Krytox pump oil which has a low vapor pressure and is not reactive with fluorine (a typical byproduct of etch plasma chemistries). The second stage pump is a Leybold 1000C Turbo Molecular pump (Part G). The turbo pump is activated once chamber pressures reach 200 mTorr, at which time the roughing pump changes functions and becomes a backing pump.

The chamber is brought up to a standard operating pressure for experimentation by introducing argon. The gas is controlled by a mass flow controller (Unit UFC-1000 0-100 sccm), passed through a Pall 0.01 μm particle filter, and then introduced to the chamber through the gas inlet discussed previously. Calibration of the mass flow controller was recently checked using a bubble column method. A calibration curve for argon is shown in Figure 4.1.4.

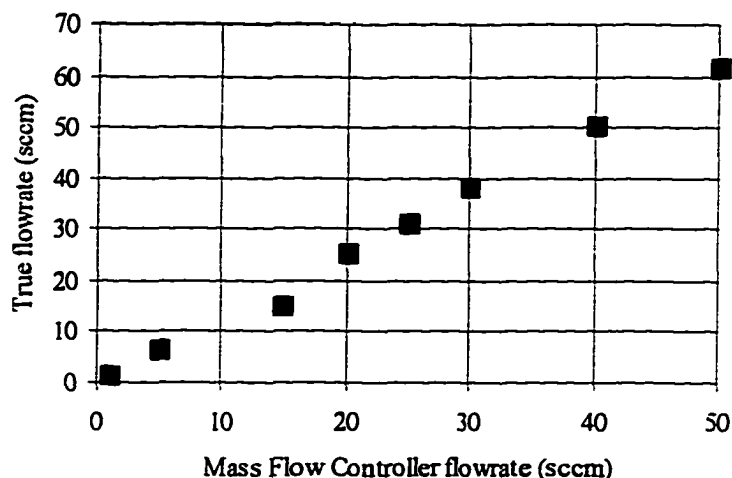


Figure 4.1.4 Calibration curve for argon mass flow controller

The plasma is generated in the chamber by passing a high frequency (13.56 MHz) current through the powered electrode. Two different radio frequency (rf) power generators have been used in the course of this research. The first rf generator (ENI HF-1) is a continuous wave generator with a power output range of 0-1000 Watts. The second generator is a Hewlet Packard 3314A function generator coupled to an ENI power amplifier (A-300 REF), where output power, frequency, and duty cycle can be controlled. The forward power was measured by a Bird Wattmeter model #43. In order to obtain the most efficient coupling possible, the impedance of the generator should match that of the plasma. To achieve that goal, the generated signal is passed through a matchbox with variable capacitance. The capacitance is tuned to minimize the amount of reflected power

due to impedance mismatch. In most cases, the reflected power was under 10% of the forward power.

Pressure in the chamber is measured by three methods. Currently, a single pressure gauge does not exist which will accurately measure pressure over the range exhibited by this chamber. Therefore, different measuring techniques must be employed in order to determine chamber pressure. All three gauges used in this work were located on the exhaust manifold or on the pumping stack. The gauges were not placed directly on the core chamber in order to avoid interference with and possible damage caused by the plasma. It is assumed that the pressures measured in the pumping stack are representative of the pressures inside the core chamber.

For high pressures (1000 mTorr-50 mTorr), a thermocouple vacuum gauge (Varian 0531) is used. This gauge relies on measuring the thermal conductivity of the gas, which is a function of pressure in this range. Although these gauges are not very accurate, they are an excellent means for determining how well the chamber is pumping down from atmospheric pressure.

A capacitance manometer (MKS 227A) is used for measuring chamber pressure during plasma operations. This gauge can be used in the 10-1000 mTorr range and is very sensitive and accurate. Capacitance manometers measure the capacitance between a fixed plate and a thin walled diaphragm which is allowed to deform under an imposed pressure gradient. By measuring the capacitance and knowing a reference pressure on one side of the diaphragm, the chamber pressure on the other side of the diaphragm can be

determined. A distinct advantage of using this gauge is that the pressure measurement is independent of the type of gas being measured. It is interesting to note that this gauge is susceptible to rf interference from leakage currents. For this reason, this gauge was an excellent diagnostic tool for determining how well the chamber was grounded. The issue of electrical grounding of the chamber will be discussed later in Chapter 4.4.

For pressures below 1 mTorr, a cold cathode ion gauge (Varian NRC 840) is used. This gauge is capable of measuring pressures down to 10^{-10} Torr and relies on measuring the number of gas molecules in a region by ionizing them and then collecting them on a grid. The indicated pressure measurement is sensitive to the type of gas that is in the chamber and is normalized to nitrogen.

Base pressure in the chamber, as determined by the ion gauge, is in the region of 10^{-6} Torr. The base pressure of this chamber is not very good for vacuum processing equipment and can be attributed to gas permeation through the many o-rings used on this system.

The chamber is equipped with a wafer transfer load-lock system. Because of substantial chamber modifications, it was not possible to utilize this feature. In order to insert or remove silicon wafers, it was necessary to vent the chamber to atmosphere and then disassemble it. Although this disassembly process was inconvenient and cumbersome, it allowed for frequent chamber cleanings and opportunities to clean the viewports which could become clouded by particle contamination.

Optical access to the chamber is made possible by fitting the access ports on the shell with flanged viewports. The viewports used in this work are MDC Del-Seal zero profile quartz. The flange diameter is 4.5 inches, the quartz viewport diameter is 2.69 inches, and the quartz thickness is 0.5 inches. The viewports have 90% transmission over the range of 0.26 μm to approximately 2.5 μm . It was found that the optical properties of the viewports degrade quickly in a fluorine environment which is present in SF_6 plasmas. Six viewports were purchased for this work. Three were used for pure argon plasmas and three were used for plasmas containing fluorine.

4.2 Experimental Diagnostic Equipment

Many diagnostic tools were made available for this work including Optical Emission Spectrometry, Mass Spectrometry, Laser Light Scatter, 3-D Laser Doppler Velocimetry/Phase Doppler Particle Analysis, and Field Emission Scanning Electron Microscopy. This rather complete diagnostic tool set allowed for a thorough characterization of particle behavior over a wide range of operating conditions.

4.2.1 Optical Emission Spectroscopy

Plasma induced emissions are monitored using an EG&G Princeton Applied Research Optical Emission Spectrometer (Model 1470). The gratings are 147.5, 600, and

1200 gratings/mm and are blazed at 300 nm, 500 nm, and 240 nm, respectively. The highest reported resolution for this equipment is 0.5 nm. Emission spectra were collected by interfacing a 125 mm fiber optic cable to one of the viewports, external to the chamber. A two-dimensional schematic of the region over which plasma emissions are collected is shown in Figure 4.2.1. It is assumed that the signal measured over the region shown represents average properties of the bulk plasma. Included software (Process Vision 3.1) is used to gather and process emission signals.

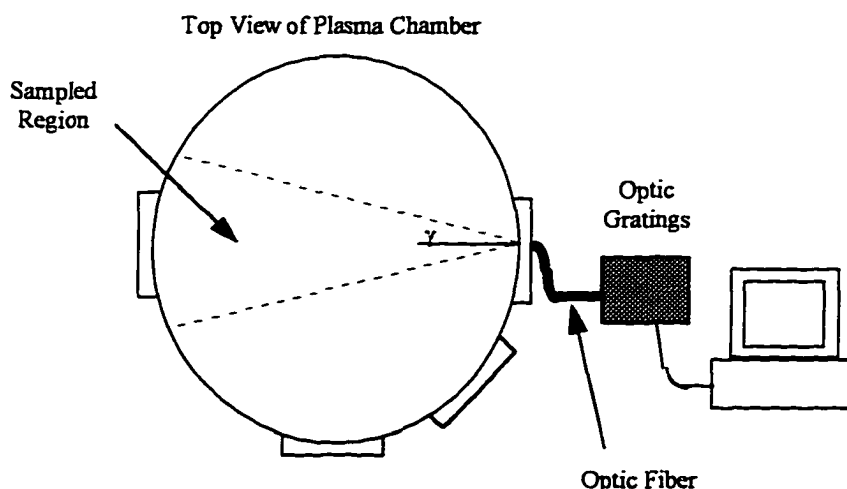


Figure 4.2.1 Emission collection region in plasma

4.2.2 Laser Light Scatter

Particles in the plasma are visualized using Laser Light Scattering. A Spectra Physics model 127 35 mW He-Ne laser is reflected off a rotating mirror in order to raster

the beam. The beam is then passed through a quartz cylinder (6 mm diameter) in order to produce a rastered laser sheet. The sheet is introduced into the chamber in order to illuminate any particles that may be present in the plasma. The scattered light from the particles is captured with a CCD camera (Sony DXC-750) equipped with a telescopic lens (Canon sx 12) and is recorded in S-VHS (Panasonic PV-S4864). This method has been used to identify primary particle trapping regions in the plasma and shifts in the particle trapping locations as a function of the operating parameters: power, gas flow rate, and pumping speed.

4.2.3 Laser Doppler Velocimetry/Phase Doppler Particle Analysis

Once the location of the particles has been identified, it is possible to measure simultaneously three-dimensional velocities and the particle size using 3-D Laser Doppler Velocimetry/Phase Doppler Particle Analysis. An Aerometrics 3-D LDV/PDPA is used in this work and has been instrumental in characterizing the behavior of particles in the particle trap. A water-cooled argon-ion laser beam (maximum power of 5 W) is split into three beams having wavelengths of 476.5 nm, 488.0 nm, and 514.5 nm. The laser was typically operated at a total power of 1 W. The three beams are then split and Bragg shifted 40 MHz from the original beam frequency. The six beams are optically coupled to two transceivers where the green (514.5 nm) and the blue (488.0 nm) beams are coupled to transceiver #1, and the violet beams (476.5 nm) are coupled to transceiver #2. The

beams in each of the transceivers are focused to a single point by transmitting the factory aligned beams through a 250 mm focal lens. The crossover of the beams defines the point at which measurements take place. Transceiver #1 is capable of measuring two directions of velocity in a plane parallel to the focal lens (Figure 4.2.2).

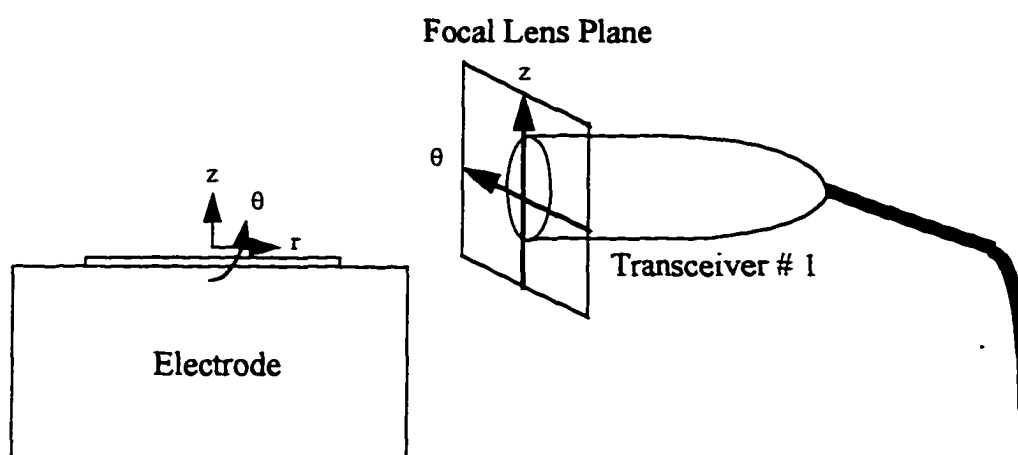


Figure 4.2.2 Measurement coordinate reference frames for LDV

Transceiver #2 can be positioned at an angle off the optical axis of Transceiver #1 to measure a third dimension of velocity. The majority of experiments in this work utilized only two dimensional velocity capabilities in order to simplify the measurement process.

The transceiver can be scanned through the chamber by manipulating a two stage traverse mounted vertically on a rail system. This system has $25 \text{ mm} \pm 1 \mu\text{m}$ translation capabilities in both the radial and vertical direction with respect to the coordinate system.

For all of the data that was collected with the LDV and is presented in this thesis, the following hardware and signal processing parameters were used. These parameters were selected to give optimal signal quality for application on dusty plasmas. The mixing frequency was 40 MHz, the sampling frequency was 0.625 MHz, the high pass filter was 1.25 MHz, the signal to noise ratio was 65, the burst threshold was 0.5 mV, and the high voltage applied to each of the photomultiplier tubes was 500 V and 600 V for the green and blue beams, respectively.

The entire chamber and laser system has been placed on a custom built, pneumatically-controlled table to dampen out vibrations inherent to clean room environments. The table, however, was not an optic table, so laser alignment with respect to the chamber was an issue. To align transceiver #1, an alignment tool with cross hairs was placed on the electrode. The transceiver was rotated such that the green beams lay vertical and perpendicular to the electrode and the blue beams lay horizontal and parallel to the electrode. The laser beams were passed through the 0 degree viewport and reflected to the opposite access port located at 180 degrees. The transceiver was aligned normal to the viewport by ensuring that the green laser beams (parallel to the electrode) began reflecting off the copper gasket on the 180 degree access port at exactly the same time during a vertical traverse. If the transceiver was not normal to the viewport, then one laser beam would begin reflecting before the other during the vertical traverse. The transceiver was aligned parallel with the electrode by lowering the beams to graze the electrode. The pitch was adjusted until the grazed reflection shone across the entire length of the

electrode. If the transceiver was not exactly parallel to the electrode, then the beam would only graze a fraction of the chuck.

4.2.4 Scanning Electron Microscopy

After the plasma has been extinguished, the particles can be collected for ex-situ analysis. Many types of microscopic analysis have been used for this work. For morphological analysis, a Hitachi Field Emission Scanning Electron Microscope (S-4500) is used. The distinct advantage of this microscope is that it is a low voltage microscope. The particles used in this work are refractory and build up an electrostatic charge which deflects the incoming electron beam. Low voltage electron guns aid to prevent charging.

4.3 Electrode Configuration

There have been many internal modifications to the chamber in order to accommodate the different types of diagnostic equipment used for this work. In general, these modifications include reducing the electrode spacing by fitting the top of the powered electrode with a raised aluminum chuck. This also served to shift the position of the particle traps to a region in the chamber that is visible.

The addition of the modified stainless steel chamber shell resulted in a very large electrode spacing, almost twice that used in comparable plasma etchers. The electrode

spacing was reduced by adding a raised chuck to the electrode. An insulating ceramic disk was placed over the electrode to cover the region not already covered by the raised chuck. The silicon wafer was then placed atop the raised chuck as shown in Figure 4.3.1.

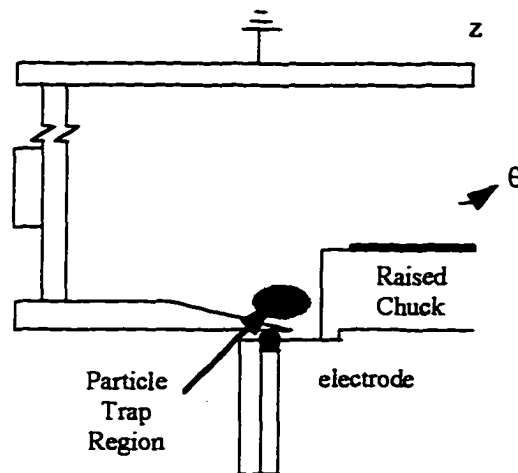


Figure 4.3.1 Base configuration with raised chuck

It was anticipated that the raised chuck would move the particles towards the middle of the plasma chamber. If the particles were towards the bottom of the chamber, the only means for visualizing them was to scatter light off the chamber wall and then off the particles (Figure 4.3.1). Using the configuration noted above, the particles sat near the base of the chamber, out of direct visible range. This resulted in extreme difficulty in making LDV measurements which require line of sight measurement of the particles.

The solution to this problem was to insulate the outer surface of the raised chuck with a hollow ceramic cylinder. Subsequently, a new raised chuck was designed in order to accommodate larger diameter silicon wafers. A ground plane consisting of a disk sitting

atop a hollow cylinder was used to move the particle trap region towards the vertical center of the chamber. The ground plane was built to lie flush with the raised chuck-insulator assembly. As a result, the particles were confined to two trapping regions: a powered electrode trap (region A) and a grounded electrode trap (region B) as shown in Figure 4.3.2.

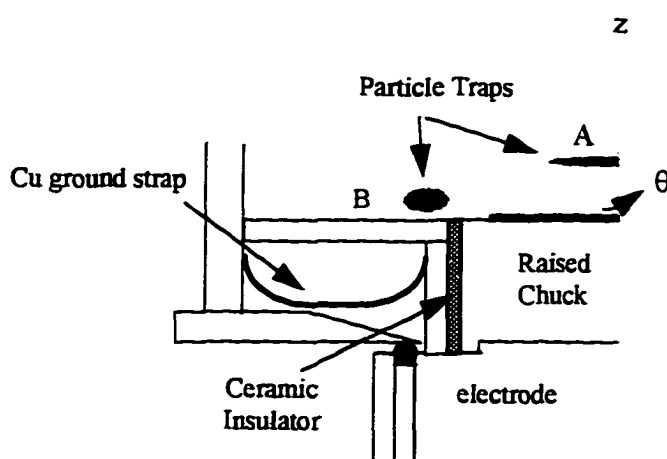


Figure 4.3.2 Modified chamber schematic

4.4 Grounding

The topic of rf grounding is largely an art rather than a science. It is definitely important because the effects of an improperly grounded rf system can be devastating. RF currents can penetrate diagnostic equipment in the room resulting in erroneous but consistent results, making detection difficult. In this section, the method by which the chamber was grounded against rf interference is explained.

The observation that the capacitance manometer varied by approximately 10 mTorr from true pressure and that the peaks for mass/charge ratios in an in-line mass spectrometer shifted by approximately 100 amu suggested a potential problem of rf leakage. A long copper strip (1 inch wide) was grounded to a copper pipe located outside the clean room. Lead solder was placed on the contact surface of the copper strip to increase conductivity. A series of copper strips was then branched off the single long strip and joined to various metal parts on and near the chamber. If that new branch resulted in a decrease in the error for the mass spectrometer and capacitance manometer, it was retained. An oscilloscope tuned to 13.56 MHz was used to identify any other rf leakage current problems throughout the room. One must be careful to avoid using too many grounding straps, otherwise internal grounding loops will be formed which will again disrupt any equipment on that grounding line.

CHAPTER 5

Trapped Particle Characterization

For the experimental configuration used throughout this work, particles were observed to trap in two primary locations. The first location was a cusp shaped cloud that existed over the powered electrode. The second trap was a toroidal ring that existed above the annular grounded electrode (Figure 5.0.1).

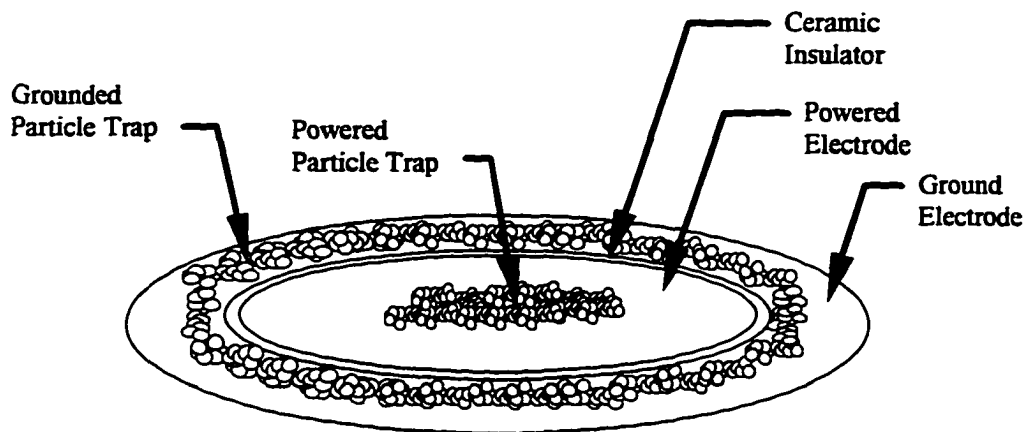


Figure 5.0.1 Particle trap locations

In this chapter, the behavior of the electrostatically trapped particles in an argon rf plasma is examined using two methods: Laser Light Scatter and Laser Doppler Velocimetry. Both methods have been discussed in Chapter 3. Specifically, the particle trap size, bulk particle velocity, and bulk trap particle concentration will be evaluated as a function of generated rf power and chamber pressure.

The outline of this chapter is as follows: the experimental method will be explained, the experimental results will be presented, and appropriate conclusions will be drawn. The experimental trends will be compared with three descriptions of particle-particle interactions which were theoretically presented in Chapter 2: thermal kinetic motion, motion due to individual particle-molecule collisions, and motion due to electrostatic repulsion, in order to give experimental evidence in support of the appropriate mechanism by which large particles move in the localized particle trap. An extension of the appropriate theory will be used to propose a mechanism by which large particles (greater than 0.1 μm in diameter) agglomerate in the plasma for a given set of reactor conditions.

5.1 Seeded Particles

The plasma was seeded with monodisperse 10.2 μm polystyrene latex spheres obtained from Duke Scientific. The motivation for seeding the plasma was to maintain a

constant concentration of particles in the plasma and to maintain a constant particle diameter.

If a dispersed size particle seed was added to the plasma or if particles were grown during the reaction, the charge on the particles and hence the electrostatic forces between the particles would not be constant. Since the interest is in studying the effects of varying reactor operating conditions on particle behavior, it would be difficult to ascertain from the experimental data whether observed trends are due to the changes in the operating condition or due to the variable particle size, unless particle size is held constant. For this reason, the monodisperse particle was selected and all major sources of particle nucleation and growth (i.e. the presence of a silicon wafer or fluorine containing parent gas) were removed from the reactor.

The 10.2 μm particle is a very large particle compared to industrial standards on the size of an actual contaminant. The primary reason for selecting this size particle is to ensure that there is a good scattered intensity signal for the Laser Doppler Velocimeter when performing experiments in a harsh plasma environment. It is assumed that the behavior of the large 10.2 μm particle will scale with particle size as was theoretically shown in Equation 2.7.3 and Figure 2.7.1 for all particle sizes greater than approximately 0.1 μm , where it was theoretically shown that Coulombic particle-particle interactions tend to dominate particle motion. A second reason for using a large particle was to increase the probability that only one particle was in the probe volume at a time given a fixed inter-particle spacing. Recall that Laser Doppler Velocimetry is a single particle

counter. For that reason, the highest confidence in the experimental measurements occurs when only one particle is in the interferometric probe volume at a given time. Laser Doppler Velocimetry measurements of smaller particles, $O(1\mu\text{m})$, tended to have a much lower statistical quality compared to larger particles, $O(10\mu\text{m})$, because there was often more than one particle in the control volume. The $10.2\mu\text{m}$ particle was chosen so as to be consistent with current *in situ* dusty plasma research [59, 76] and perform successfully with the Laser Doppler Velocimeter.

Initially, the particles as shipped by the manufacturer were suspended as 10% solids in DI water. In this suspension, the particles agglomerated as shown in Figure 5.1.1.

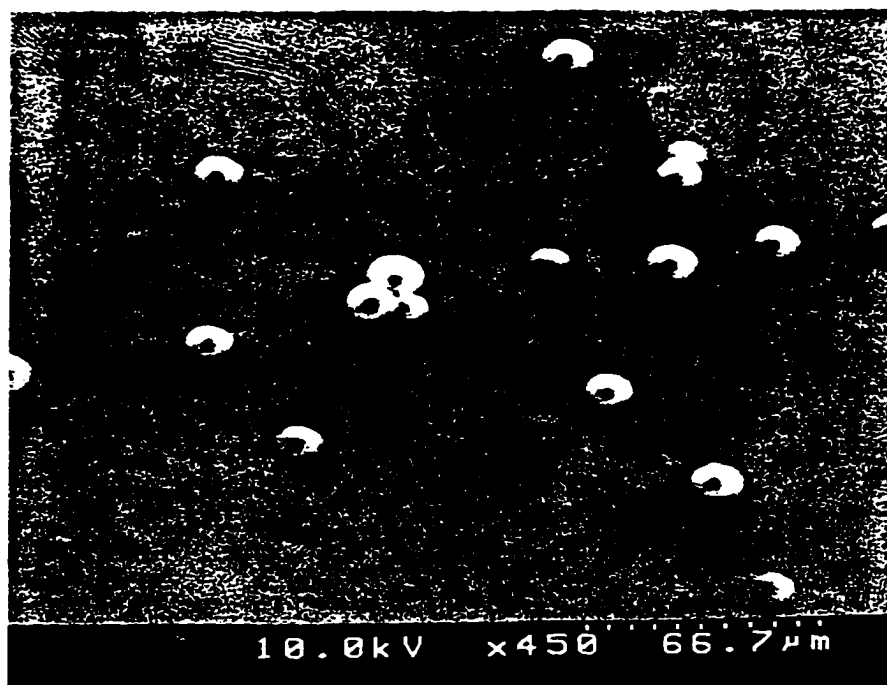


Figure 5.1.1 FESEM micrograph of agglomerated PSL particles

This diminishes the apparent advantage of working with a monodisperse particle as discussed previously, so efforts were taken to prevent this agglomeration. It was found that the following recipe was sufficient for preventing agglomeration: 1) centrifugate solid-water solution at 15,000 RPM for ten minutes, 2) remove water and re-suspend the settled particles in isopropyl alcohol (IPA), 3) re-centrifugate solid-IPA solution, remove separated IPA, and re-suspend in IPA to remove any residual water, and 4) sonicate solid-IPA solution for 10 minutes. A sample of particles collected on a copper substrate after this preparation is shown in Figure 5.1.2, showing very little particle agglomeration.

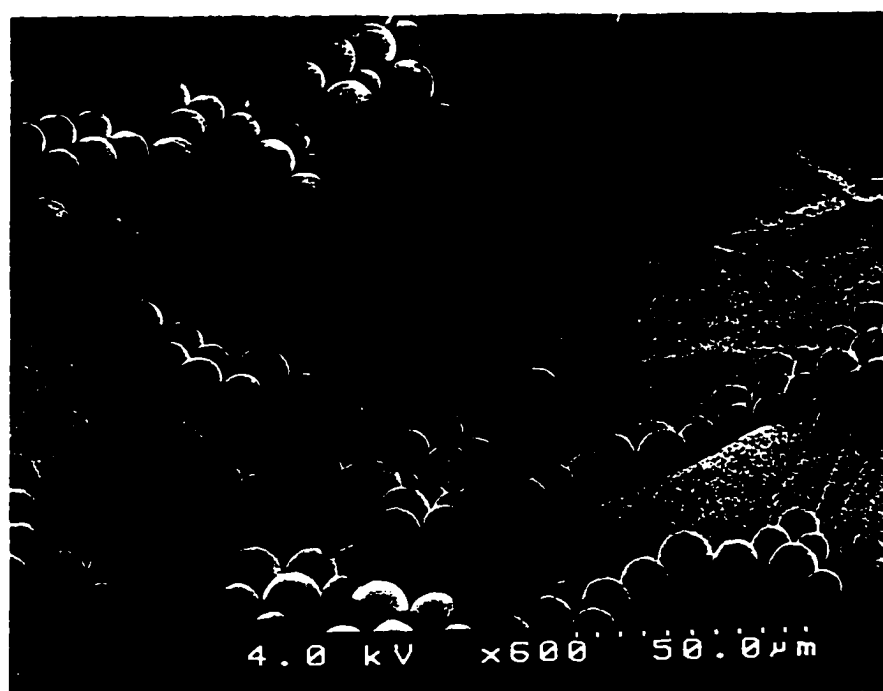


Figure 5.1.2 FESEM micrograph of monodisperse PSL particles

The particles are introduced to the plasma chamber by means of a particle injector (Figure 5.1.3). The method of particle injection relies on fluid flow induced by a pressure gradient established by chamber vacuum on the downstream side of the particle injector and pressurized argon on the upstream side. Two to three drops of the particle-IPA solution are placed on the upstream side of the particle injector. The IPA is driven off by heating the injector with a hot air dryer. The upstream portion of the injector is flushed with argon gas before being sealed and pressurized to just above atmospheric pressure. To introduce the particles to the plasma chamber, a pneumatic valve separating the two pressure regions is quickly opened and closed. A plasma must be ignited in order to charge and trap the particles. If a plasma is not ignited, the injected particles will travel diametrically across the chamber and collide with the opposite wall. Varying concentrations of particles were loaded in the chamber by toggling the injection valve for short (low concentrations) or long times (high concentrations). Visual inspection of the intensity of the scattered light off of the trapped particles indicated whether there were high concentrations (high intensity) or low concentrations (low intensity) of trapped particles.

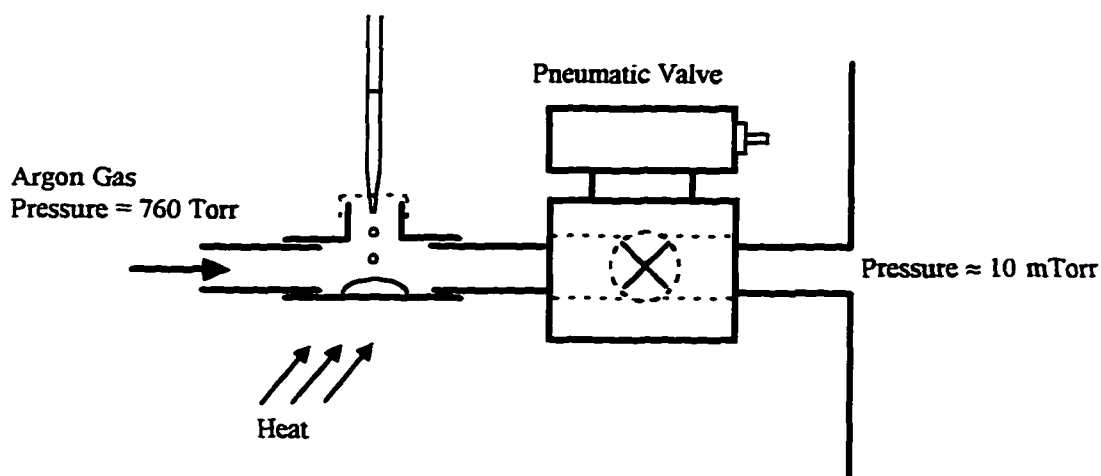


Figure 5.1.3 Schematic of the particle injector

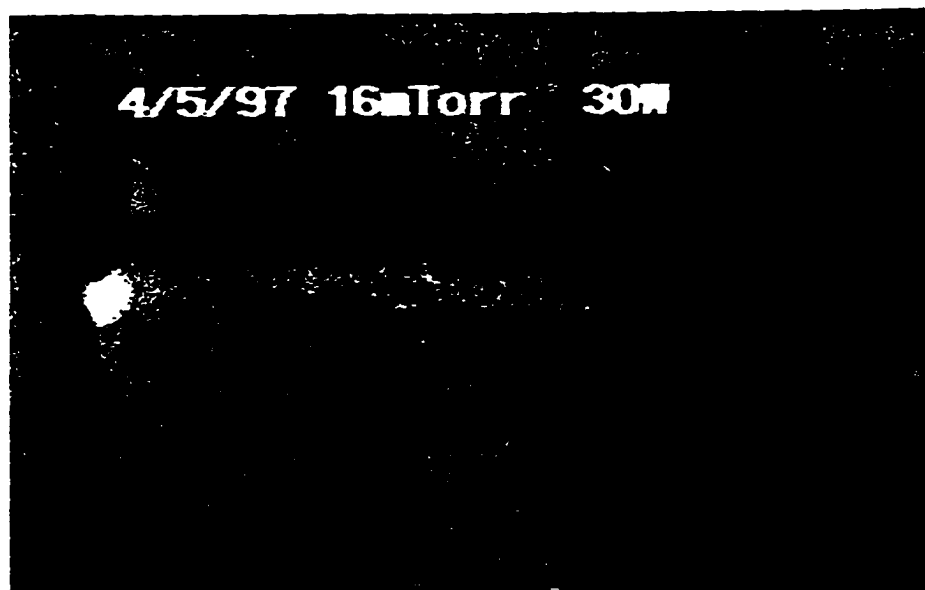
5.2 Laser Light Scatter

The visualization of trapped particles is important in order to realize bulk behavior of the particles. Laser light scattered from the surface of the trapped particles allows for particle behavior visualization. Typically, it is useful to visualize an entire section of the particle trap rather than just the particles passing through a single laser beam. This can be done by either rastering a laser beam through the plasma chamber or by sending the laser beam through a quartz cylinder which splits the beam into a laser sheet, as previously discussed in Chapter 3.2.

Simple behavioral trends of the particle trap can be determined by taking videographic images of the particles illuminated by laser light. In the following figures,

basic trends of particle behavior are shown as a function of increasing pressure and power for particles in the powered electrode particle trap, Figures 5.2.1-4 and Figures 5.2.5-8, respectively. In this set of experiments, an argon plasma was ignited, PSL particles were injected, and for reasons which will be discussed later, the reactor was allowed to run uninterrupted for a thirty minute time period. After this thirty minute time period, the pressure and power were varied with the expectation that time was no longer an important factor. In the discussion that follows, the number of particles in the plasma was not changed although the local particle concentrations did change with plasma parameter variations. The particles were visualized by passing a laser sheet through the powered electrode particle trap. Two observations can be readily made from the Laser Light Scattering experiments. First, as either power or pressure is increased, the region of space occupied by the particles reduces. The scattered light intensity is proportional to the concentration of particles in a localized region, so regions of high intensity indicate a high particle concentration; low intensity indicates low particle concentration. From the simple LLS experiments, it is observed that with an increase in power at constant pressure (Figures 5.2.1-4), the local particle trap concentration appears to increase. With an increase in pressure at constant power (Figures 5.2.5-8), it is observed that the local particle trap concentration first increases over the range of 9 to 18 mTorr, then decreases for further increases in the pressure. The 9 mTorr example is not shown, but the particles occupied a large region in the plasma and there was a low scattered intensity from the particles. The following images were recorded with the imaging system discussed in

Chapter 4 and were digitally captured off of the video and printed by Biomedical Communications at the University of Arizona.



Figures 5.2.1 LLS image of 10.2 μm PSL particles at 30 W and 16 mTorr.

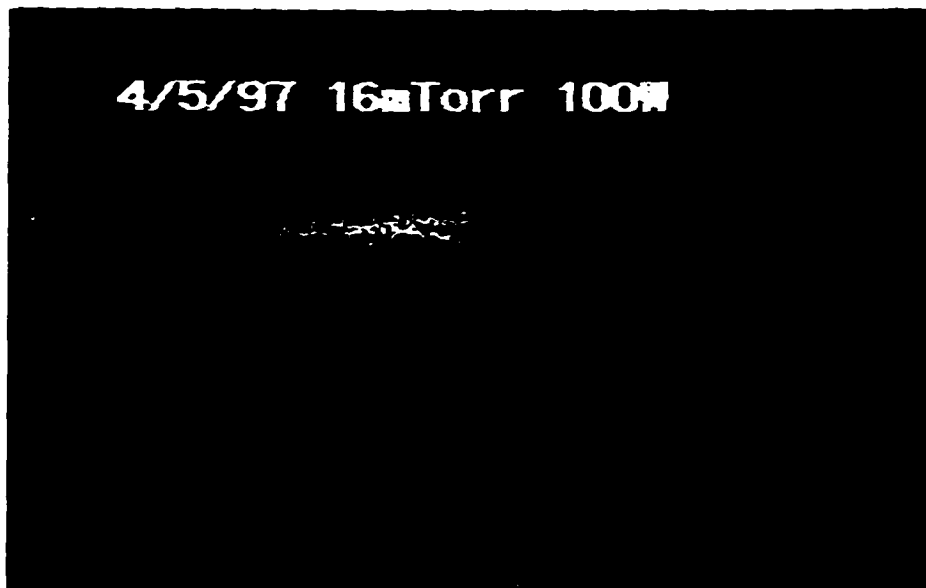


Figure 5.2.2 LLS image of 10.2 μm PSL particles at 100 W and 16 mTorr.

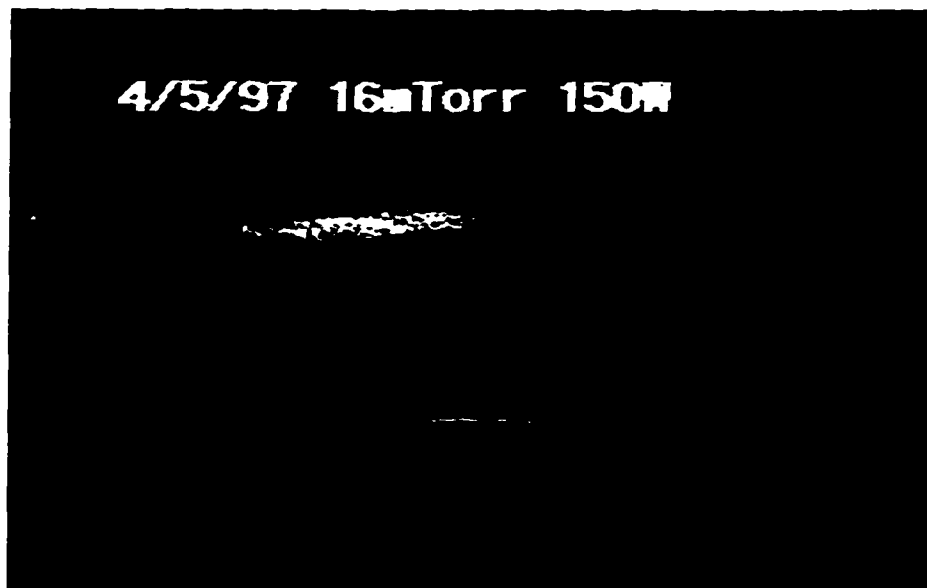


Figure 5.2.3 LLS image of 10.2 μm PSL particles at 150 W and 16 mTorr.

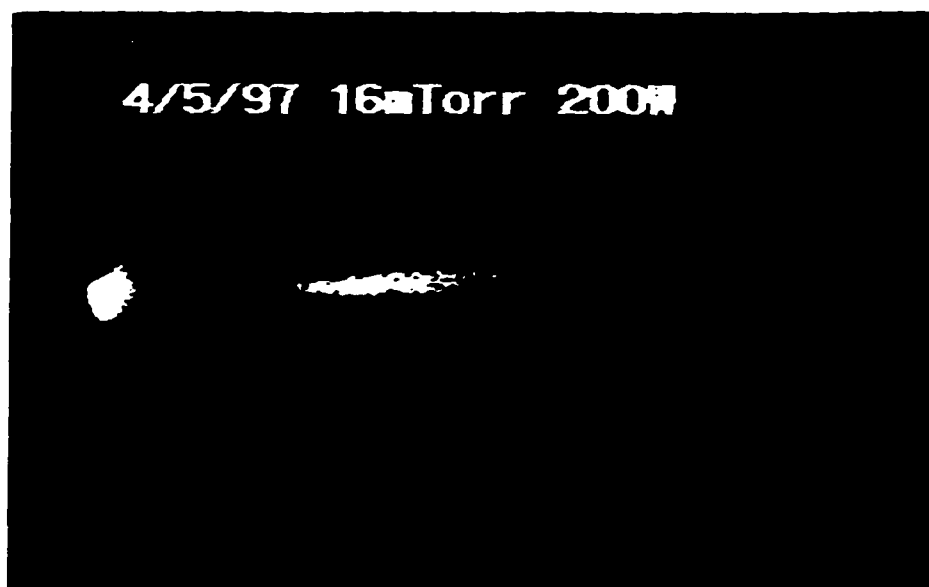


Figure 5.2.4 LLS image of 10.2 μm PSL particles at 200 W and 16 mTorr.

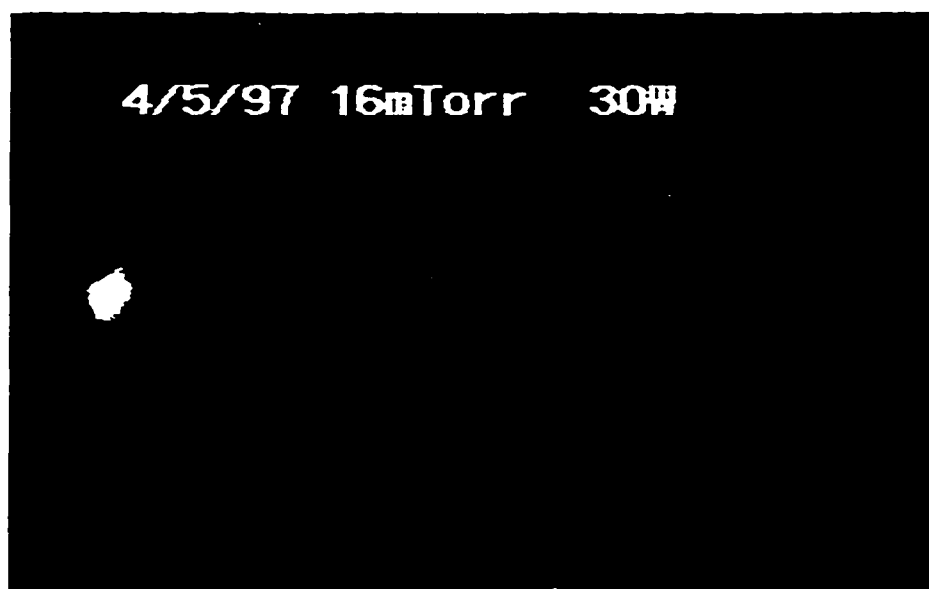


Figure 5.2.5 LLS image of 10.2 μm PSL particles at 30 W and 16 mTorr.

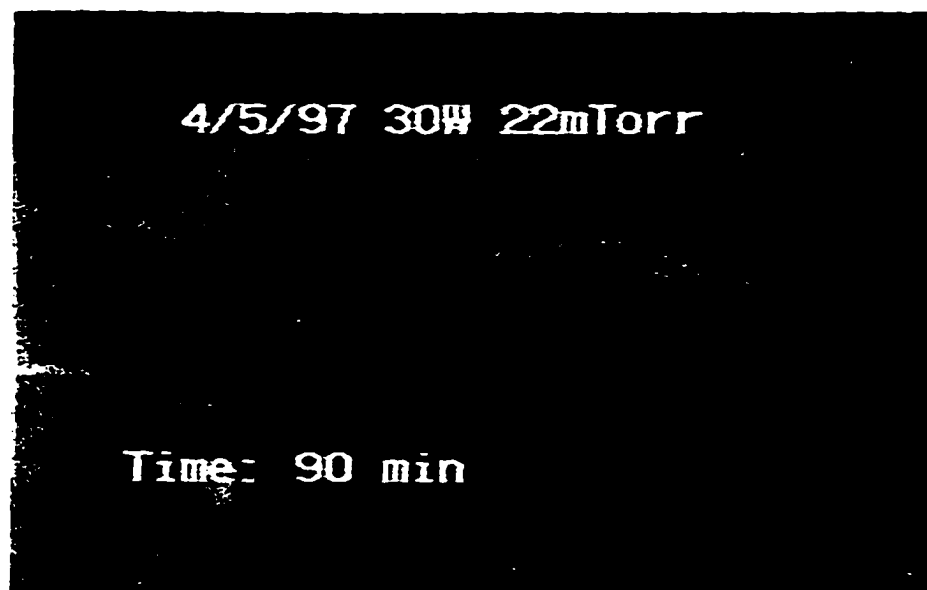


Figure 5.2.6 LLS image of 10.2 μm PSL particles at 30 W and 22 mTorr.

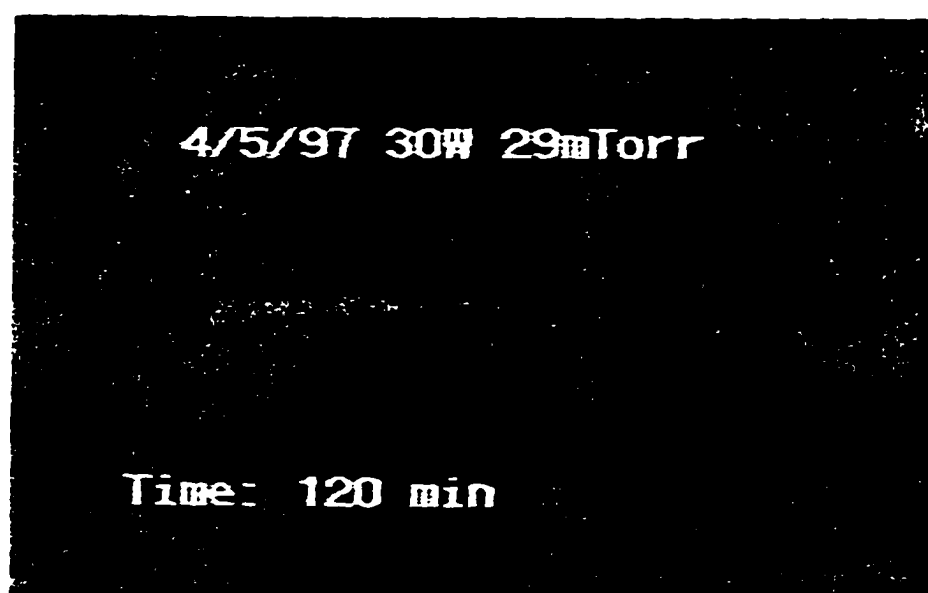


Figure 5.2.7 LLS image of 10.2 μm PSL particles at 30 W and 29 mTorr.

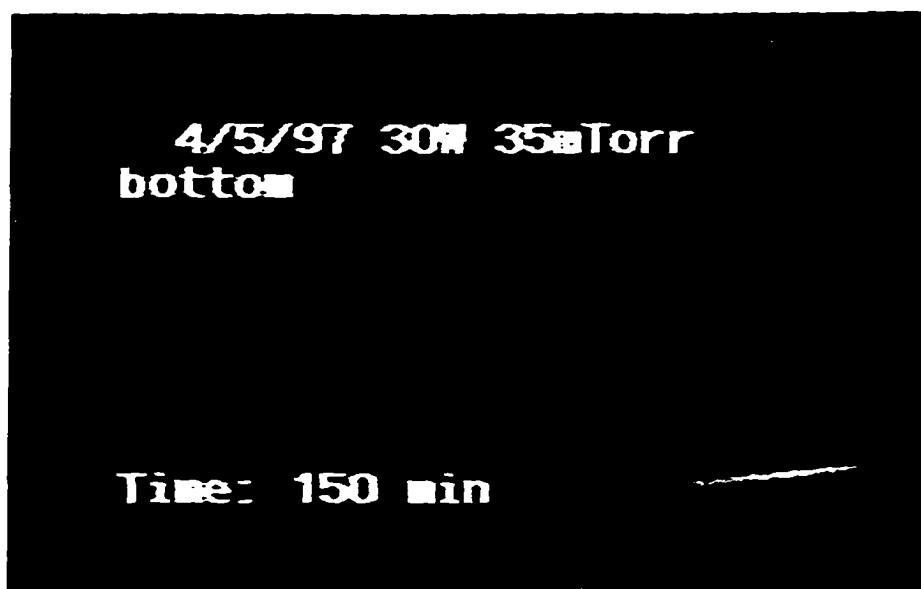


Figure 5.2.8 LLS image of 10.2 μm PSL particles at 30 W and 35 mTorr.

Unfortunately, it is very difficult to obtain an accurate representation of distance in the video images, and hence changes in trap size or particle concentration are difficult to quantify. For this reason, a technique was developed which combined the LLS/LDV technique to serve as a single particle counter. In the method discussed for Laser Doppler Velocimetry in Chapter 3, two laser beams are crossed to form an interferometric probe volume. When a particle passes through that volume, light will be scattered from the surface of the particle. Using the detection and electronic processing capabilities of the LDV, it is possible to determine the temporal frequency (data rate) of particles passing through the probe volume.

The laser transmitter was placed on a home-built two stage manipulator so that the interferometric probe volume could be traversed throughout the chamber (Figure 5.2.9).

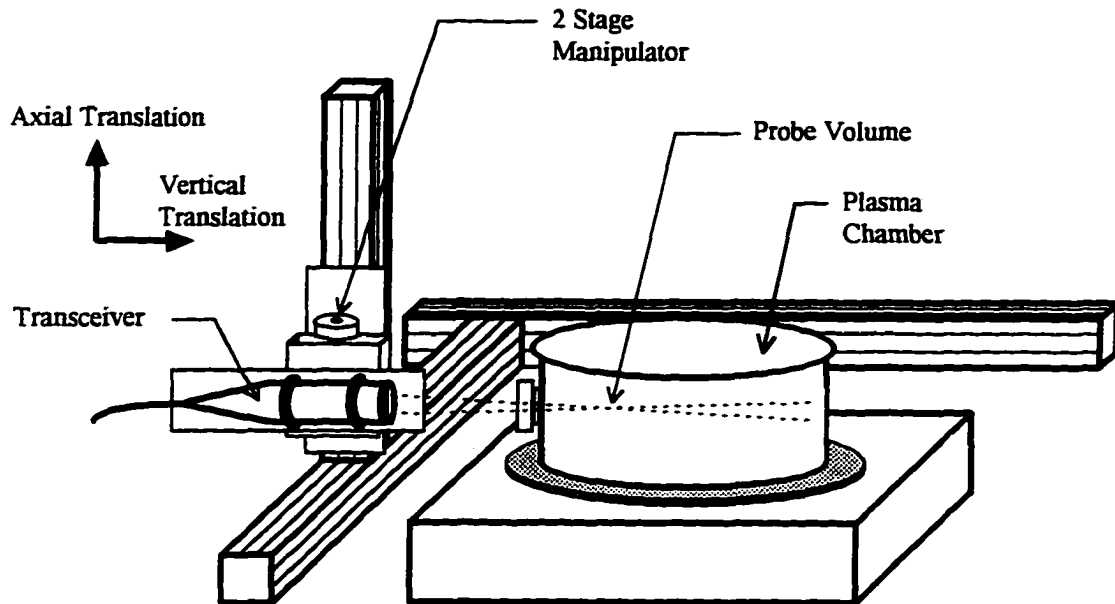


Figure 5.2.9 LDV traversing system

The traverse system spanned a distance of 25 mm in the axial direction and 25 mm in the radial direction with a tolerance of $\pm 1\mu\text{m}$. In this method, the data rate of particles passing through the interferometric probe volume could be spatially resolved in the particle trap. One such example of the spatially resolved data rate through a ground plane particle trap is shown in Figure 5.2.10.

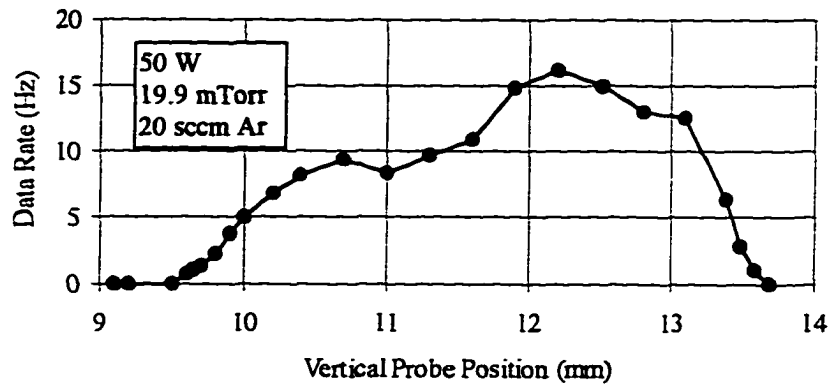


Figure 5.2.10 Spatially resolved data rate for PSL particles in a ground plane particle trap. The Data Rate is plotted versus the vertical positioning of the interferometric probe volume above the surface of the grounded electrode.

For this experiment, the plasma rf power was 50 W, the chamber pressure was 19.9 mTorr, the flowrate was 20 sccm Ar (standard cubic centimeters of argon per minute), the maximum data rate was approximately 20 Hz, and the maximum local particle concentration was approximately $3 \times 10^{10} \text{ \#/m}^3$. It is readily observed that the total thickness of the trap can be represented at a 1 Hz data rate. Figure 5.2.11 represents the relative error in measuring the particle trap thickness determined by a particular data rate relative to the thickness determined by the lowest detectable data rate ($\sim 0.1 \text{ Hz}$).

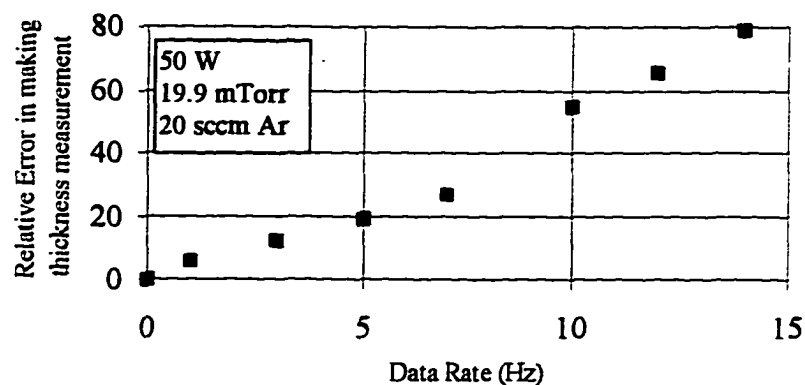


Figure 5.2.11 Error in making trap boundary measurements at a data rate other than the lowest detectable rate, taken from the data in Figure 5.2.10

It is observed that with this particular experiment, the error associated with making the thickness measurement at 1 Hz compared with the thickness at 0.1 Hz is approximately 6%. This error is consistent over the range of reactor operating conditions.

Using the particle counting method, it is possible to define the outer boundaries of the particle trap simply by traversing the laser probe through the entire cross section and recording the locations at which approximately a 1 Hz data rate occurs. This method can be used to characterize either the powered electrode particle trap or the grounded electrode particle trap. Typically, the cross section of the former was larger than the 25 mm radial traversing capabilities, hence requiring substantial hardware modification during an experiment in order to characterize the cross section of the entire trap. However, the radial and axial dimensions of the cross section of the ground plane trap were less than the maximum 25 mm. In addition, no matter what point was sampled in the ground plane trap,

the laser beams were never blocked by the chamber, as was unfortunately the case with some locations in the powered particle trap. For the reasons of having easily characterizable dimensions and for always being in the field of view of the measurement apparatus, the ground plane trap cross section was extensively studied in these experiments.

A representative figure of the shape of the cross section of the toroidal ground plane particle trap is shown in Figure 5.2.12 for the conditions of 50 W, 19.9 mTorr, 20 sccm Ar, and a maximum local particle concentration of $3 \times 10^{10} \text{ \#/m}^3$. The shape of the particle trap for this example was determined after the plasma had been ignited for over thirty minutes. In the figure, the edge of the powered electrode is located at (0,0) and the distances refer to positions located vertically above and radially outward from the electrode.

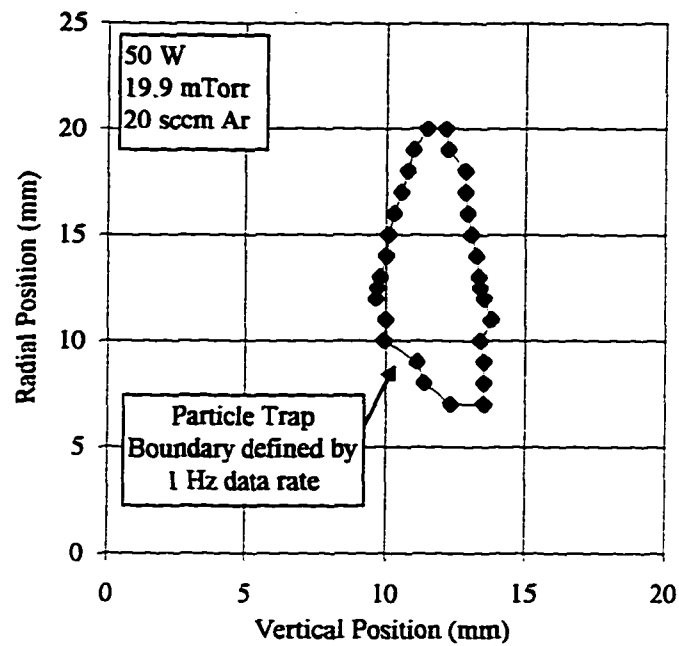


Figure 5.2.12 Representative outline of the ground plane trap cross section

For a variety of experimental conditions, generating plots similar to Figure 5.2.12 would require an inordinate amount of time. Considerable simplifications can be made by realizing that the cross section of the particle trap is approximately polyhedral, and that the cross sectional area (A) can be approximated by:

$$A = 1/2 \Delta r \Delta z \quad [5.2.1]$$

where Δr is the radial thickness and Δz is the axial thickness. This calculation is reasonable insofar as effort is taken to ensure that the maximum axial and radial thickness are sampled for each of the experimental conditions. It was found that the shape of the particle trap remained polyhedral for all time that the plasma was ignited.

In some initial experiments, it was recognized that the trap cross section area is a function of many parameters including power, pressure, particle concentration, and time. Particle trap size dependence on power, pressure, and particle concentration is not a surprising result, but the dependence on time is and is troubling in that it complicates experimentation. To speculate, a dependence in time might occur for any of four reasons: 1) the effective number of particles decreases due to particle agglomeration hence the particles take up less space in the reactor, 2) the particles continuously move close together over time and occupy less space, 3) the particles are relocating to another more preferred particle trapping location in the plasma, or 4) the particles are falling out of the particle trap during plasma ignition at a certain rate. The underlying cause will be explained by experimental evidence presented over the rest of the chapter. Figure 5.2.13 is a representative plot showing how the trap cross section changes with time for an experiment with 30 W generated rf power, 16.5 mTorr chamber pressure, and 20 sccm Ar.

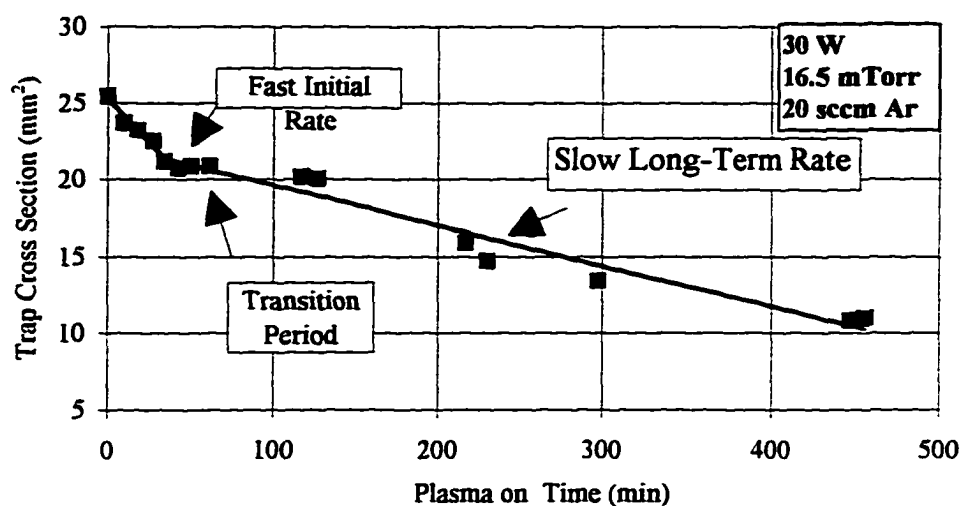


Figure 5.2.13 Representative particle trap cross section decay in time

Initially, the trap cross section decreases at a rate on the order of $0.1 \text{ mm}^2/\text{min}$ followed by a slower cross section decrease rate of approximately $0.02 \text{ mm}^2/\text{min}$ in the long term. This indicates that there are at least two dominant physical phenomena which govern the shape of the particle trap during the different time scales.

Notice that the experiment in Figure 5.2.13 was carried out for 450 minutes. Clearly, etch reactions in industrial plasma processes do not normally occur for 450 minutes. The motivation behind conducting the long experiments is to give substantial time for the trap to change significantly beyond measurement tolerances.

The present goal is to understand what the dominating physical phenomena are in the short and long time scales. Physical insight to the initial transient behavior of the trap

may be gained by evaluating the transient behavior of the plasma using Optical Emission Spectroscopy.

5.3 Optical Emission Spectroscopy (OES)

Optical Emission Spectroscopy (OES) is used to track the temporal behavior of emitting species in the plasma. For the argon plasma of interest, a resonant argon emission line is found at 750.4 nm. The emission intensity is a function of the electron energy distribution function [77]:

$$I = an_{Ar} \int [\sigma(\epsilon, i) \epsilon^3 f_e(\epsilon)] d\epsilon \quad [5.3.1]$$

where a is a constant, σ is a cross section for photon emission, and ϵ is the electron energy. The electron energy distribution function, $f_e(\epsilon)$, will develop over time after the plasma is ignited, indicating that it takes a finite amount of time for the electron concentration and the energy of the electrons to reach quasi-steady state. Accordingly, the temporal behavior of the intensity of the 750.4 nm emission line, dI/dt , reflects how the electron energy distribution function, $f(\epsilon)$, changes with time:

$$\frac{dI}{dt} = an_{Ar} \int_0^{\infty} \sigma(\epsilon, i) \frac{d}{dt} [\epsilon^3 f_e(\epsilon)] d\epsilon \quad [5.3.2]$$

In Figure 5.3.1, the emission intensity of the 750.4 nm argon emission line as a function of time for a seeded dusty plasma at 50W, 27 mTorr, and 40 sccm is shown.

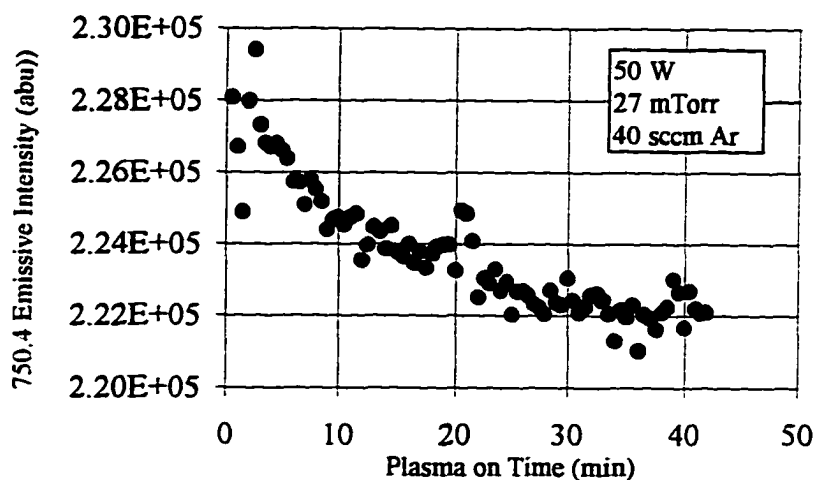


Figure 5.3.1 Emission intensity of 750.4 nm argon line as a function of time

The emission intensity reaches a steady state value after approximately 25 to 30 minutes, which indicates that the electron energy distribution function reaches quasi-steady state. The time for the electron energy distribution function to reach quasi-steady state is similar to the time at which a transition occurred between the initial and long-term cross section area loss rates as seen in Figure 5.2.13. The time to reach quasi-steady state is heavily influenced by the presence of particles over the pristine (no-particle) case as shown in Figure 5.3.2, however does not appear to be a strong function of the concentration of particles present (Figure 5.3.3).

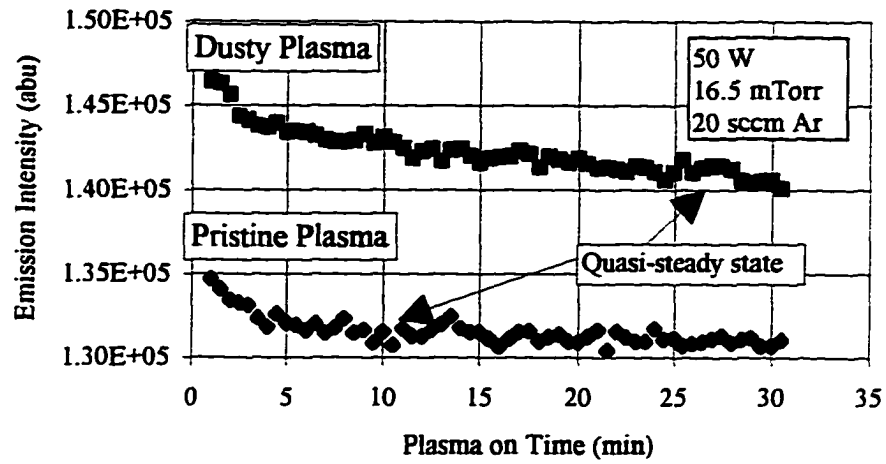


Figure 5.3.2 Comparison of emission-time profiles for dusty and pristine plasmas

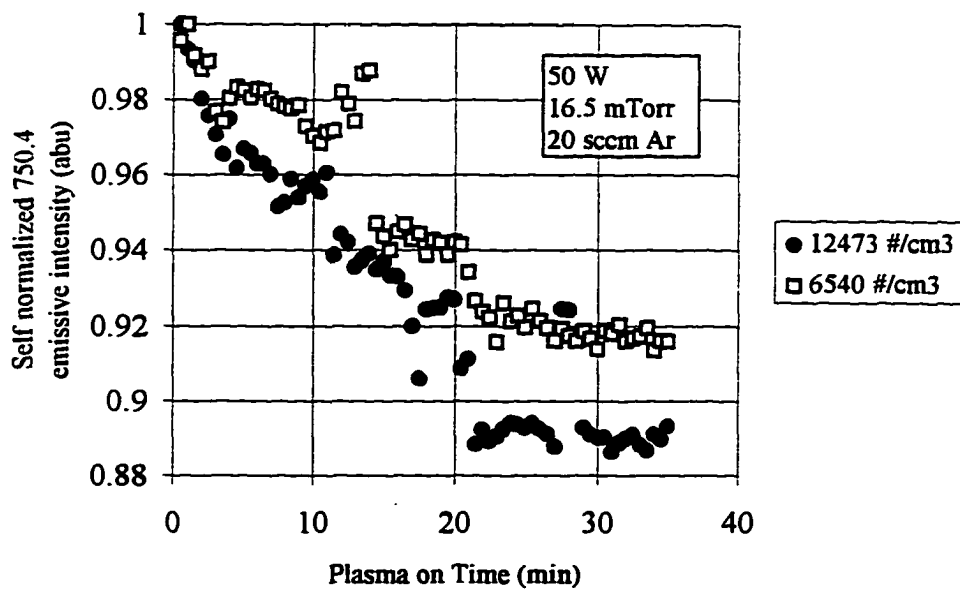


Figure 5.3.3 Intensity-time profiles for high and low total particle concentrations

The equilibrium time depends both on power (Figure 5.3.4) and pressure (Figure 5.3.5), and generally decreases for an increase in either power or pressure. The equilibrium time is taken as the transition periods from the particle trap cross section plots as shown in Figure 5.2.13 and from OES intensity plots as shown in Figure 5.3.1.

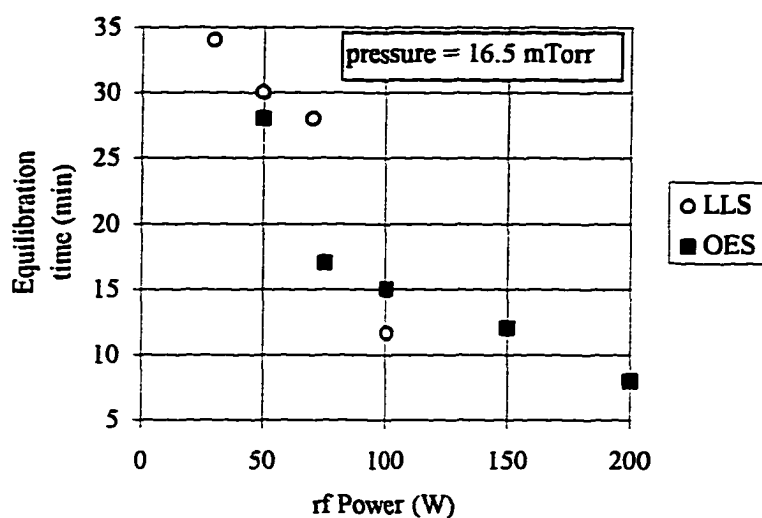


Figure 5.3.4 Equilibrium time dependence on power at constant pressure

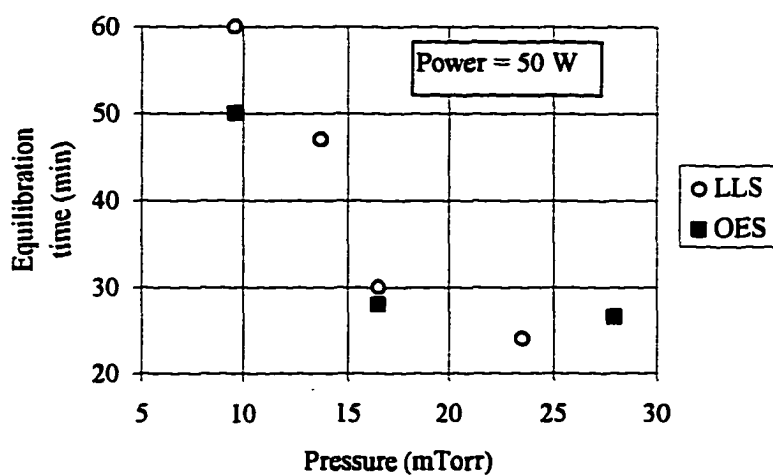


Figure 5.3.5 Equilibrium time dependence on pressure at constant power

The initial compression of the particle trap appears to be directly related to the plasma achieving quasi-steady state. However, once the plasma has reached quasi-steady state, it is important to know whether changes in reactor operating conditions induce a secondary transient response in the plasma and hence cause a high particle trap area compression rate. To study this, two experiments were performed where pressure and power were varied. Two time scales are of interest. The first time scale is the time required for the plasma and the emission intensity to respond to a sudden change in the power or pressure, termed here the immediate response time. The second time scale is the time it takes for the emission intensity to asymptote to a steady state value after the immediate response time, referred to as the secondary quasi-steady state time.

In one experiment, the plasma was ignited at 16 mTorr, 20 sccm, 50W and allowed to run undisturbed for approximately 50 minutes. The pressure in the chamber was then reduced to 9 mTorr where it was held constant for 25 minutes, after which time the pressure was returned to 16 mTorr for another 25 minutes. The pressure was then increased to 29 mTorr for 10 minutes followed by a return to 16 mTorr. Figure 5.3.6 shows the results of the 750.4 Ar emission intensity as a function of time for this particular reaction. Note that there was an initial temporal response of approximately 25 minutes where the plasma went to quasi-steady state. A change in pressure resulted in a change in the emission intensity, which had an immediate response time constant of less than one minute. The emission intensity at 16 mTorr was found to be independent of the prior chamber pressure, hence no hysteresis due to pressure changes is observed.

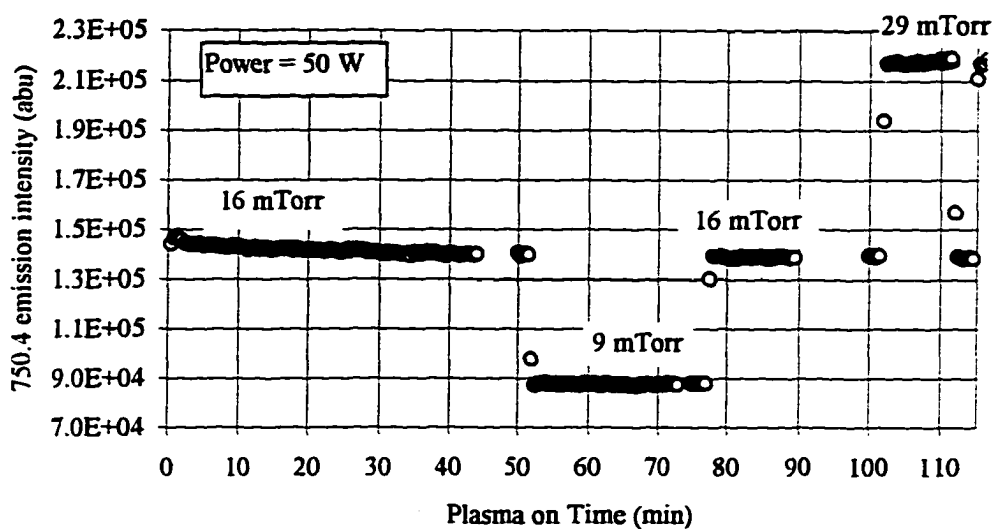


Figure 5.3.6 Evaluation of secondary emission response as a function of pressure

A second experiment was performed for variations in the plasma power (Figure 5.3.7). The base pressure and power were 16.5 mTorr and 50 W, respectively. The power was varied as follows: 50 W for 40 minutes, 25 W for 15 minutes, 50 W for 15 minutes, 75 W for 10 minutes, 50 W for 20 minutes, 100 W for 15 minutes, 50 W for 15 minutes, 150 W for 15 minutes, and 50 W minutes for 30 minutes.

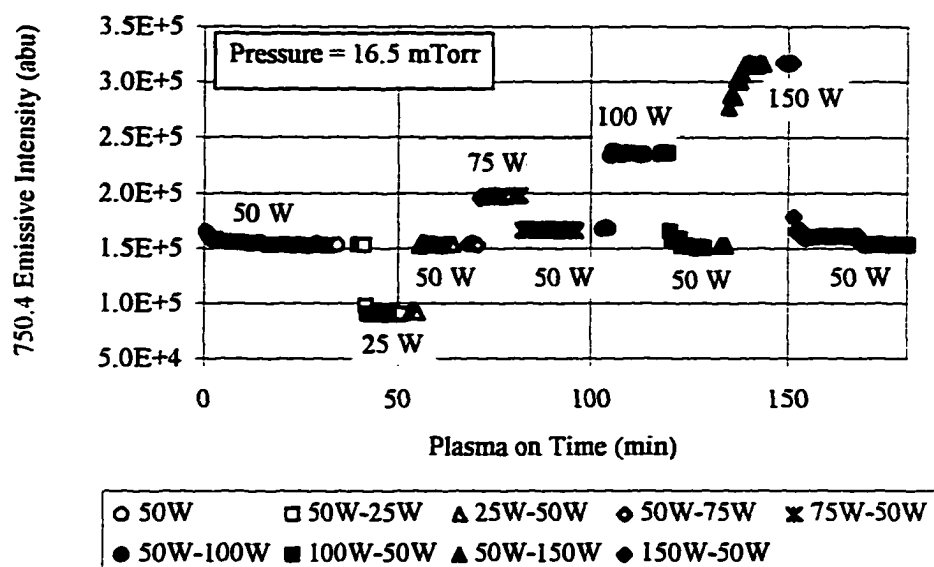


Figure 5.3.7 Evaluation of secondary emission response as a function of power

The emission intensities were observed to change directly with a change in power, although the immediate response time increased with higher powers reaching approximately five minutes at a power of 150 W. In addition to the immediate response time, the plasma did go through a secondary transient to re-establish quasi-steady state. This effect was prevalent only during large power changes and lasted on the order of ten minutes, compared with the initial quasi-steady state time constant of approximately 30 minutes. Power fluctuations appear to have a dramatic impact on both the immediate response time and the secondary quasi-steady state time constants. This behavior was also observed with power fluctuations in a pristine plasma, and therefore it can be concluded

that this behavior is not due to the presence of the particles. Originally, it was thought that the transient behaviors might be due to the presence of the particles since it is probable that there is residual water adsorbed on the surface of the particles which would desorb at high plasma power. This would temporarily result in high concentrations of water in the plasma until the water is completely pumped out of the chamber. The fact that the transient behaviors exist independent of the presence of the particles indicates that the presence of any water on the surface of the particles is not substantial enough to cause a shift in the quasi-equilibrated state of the plasma. Furthermore, it can be concluded that the presence of any water on the surface of the particles cannot be used to explain the increased initial quasi-steady state time constant for a dusty plasma over a pristine plasma as shown previously in Figure 5.3.2.

5.4 Long Term Particle Trap Behavior

After the plasma has reached quasi-steady state, the particle trap still exhibits a reduction in time, however at a much slower rate than the initial behavior. The initial and long term particle trap compression rates are shown as a function of power and pressure in Figures 5.4.1 and 5.4.2, respectively.

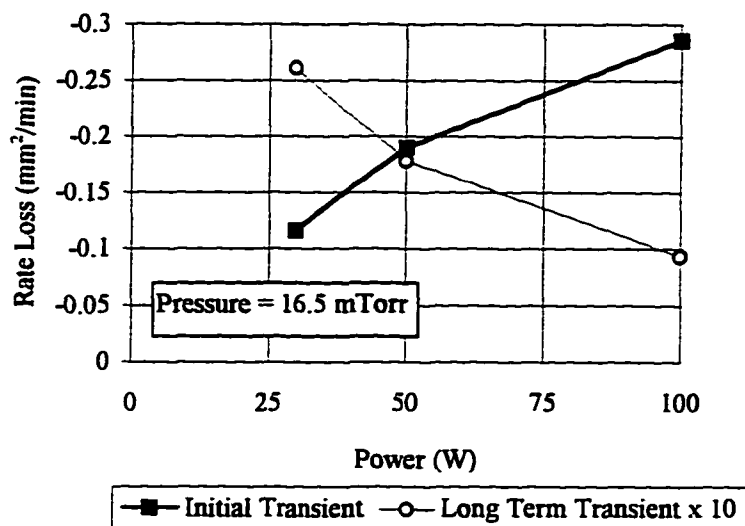


Figure 5.4.1 Cross section rate loss as a function of power at 16.5 mTorr

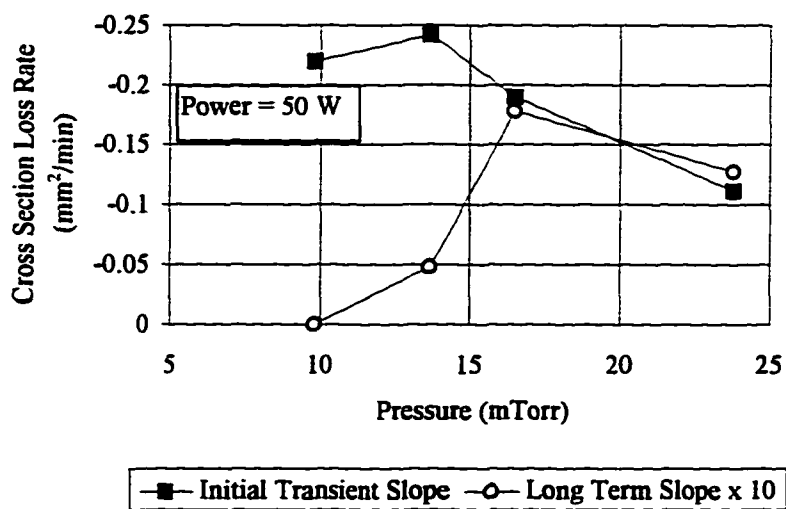


Figure 5.4.2 Cross section rate loss as a function of pressure at 50 W

For an increase in power, the rate of change in the particle trap cross section increases during the short time scale, but decreases in the long-time scale. The short time scale result is consistent with the observation that the rate of change of the plasma emission intensity as the plasma tends towards quasi-steady state increases as the power is increased at a pressure of 16.5 mTorr (Figure 5.4.3).

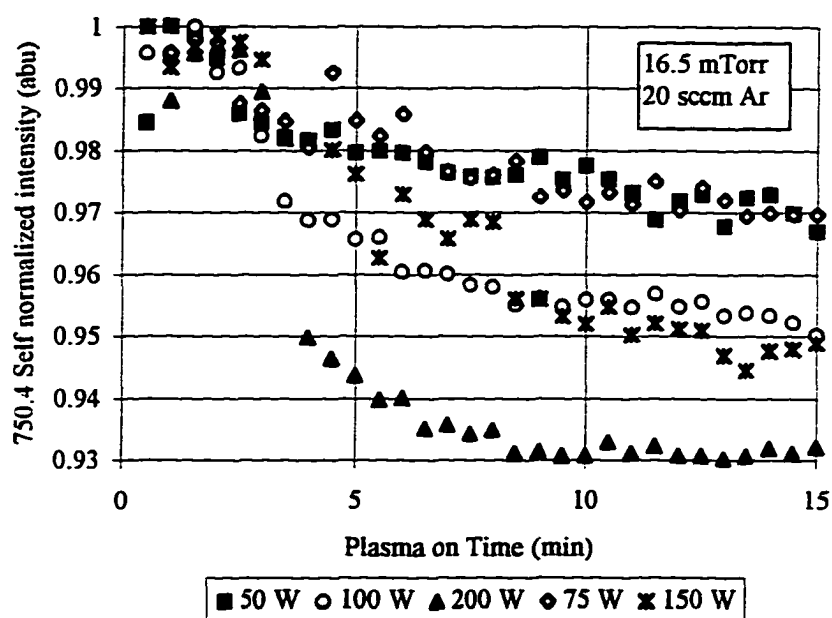


Figure 5.4.3 Emission-time profiles for varied power at constant pressure

The physical phenomena which governs the long term particle trap behavior appears to damp at high powers. For an increase in pressure, the particle trap compression rate decreases in the short time but experiences a non-linear behavior in the long term. Again, the initial compression rate behavior is consistent with the fact that the initial rate of

change of the emission intensity decreases for increases in pressure (Figure 5.4.4). The long term behavior suggests that at low pressures (8 mTorr) and at high pressures (28 mTorr), there is a dampening of the force driving the compression rate, however at medium pressures (16 mTorr), the driving force is strong.

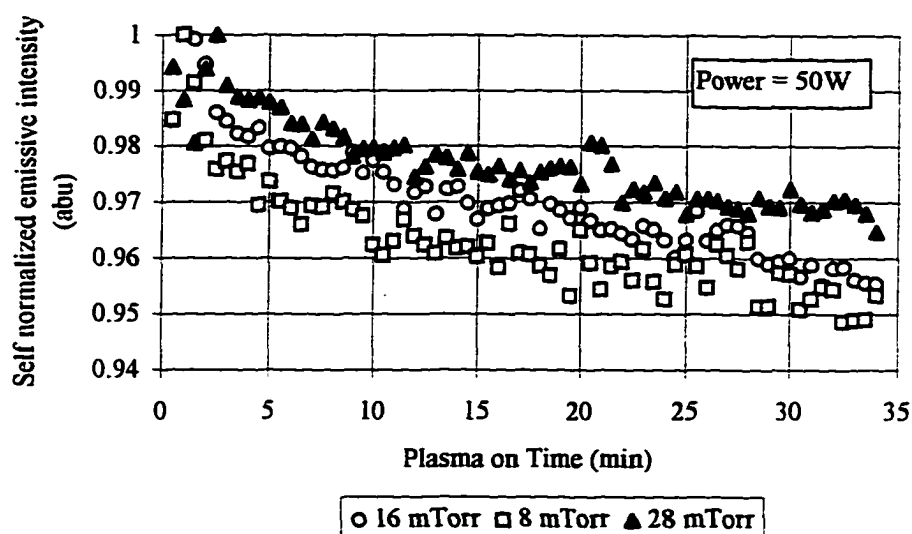


Figure 5.4.4 Emission-time profiles for varied pressure at 50 W

The dependence of the particle trap area on plasma power and pressure can be determined once the plasma has reached quasi-steady state as long as the variations in trap size due to changes in power or pressure are much greater than the time dependent compression of the trap that occurs over the course of the experiment. In the figures to follow, measurements were taken once the plasma reached quasi-steady state, approximately thirty minutes after initial ignition. Figures 5.4.5 and 5.4.6 show the dependence of the equilibrated particle trap cross section for variations in power and

pressure, respectively. In both cases, two experiments were performed with low and high concentrations of particles injected in the plasma.

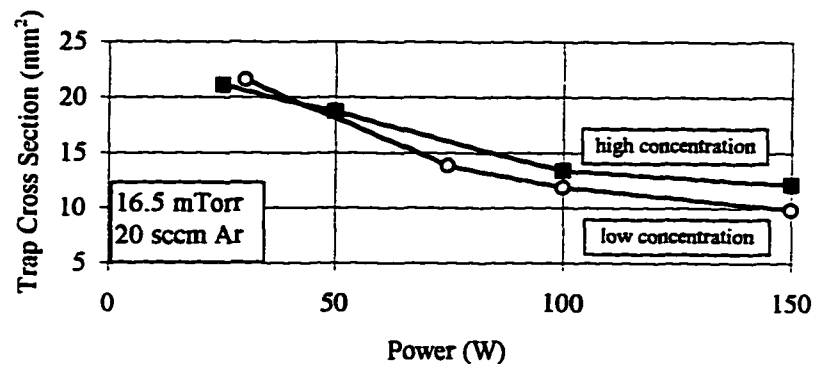


Figure 5.4.5 Variation of trap cross section with power at 16.5 mTorr

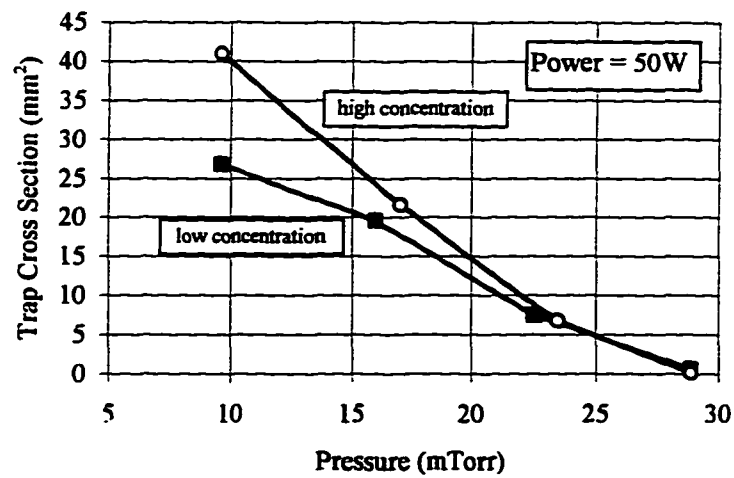


Figure 5.4.6 Variation of trap cross section with pressure at 50 W

It is observed that the particle trap size decreases for an increase in either power or pressure. The concentration of the particles does have an effect on the size of the trap and to what extent it changes with variations of the operating parameters, however, the basic trend of decreasing size with increasing pressure or power holds independent of the concentration of particles. Because the particle trap cross section changes similarly for power and pressure, it was realized that by choosing an appropriate combination of variables, the dependence on power and pressure can be expressed in a single equation. A multiplicative combination of variables was chosen because of mathematical similarity to the dependence of plasma parameters on power and pressure as described in Chapter 2.1. The resulting empirically derived equation is:

$$\text{Area} = \kappa - \frac{(W^{1/4}P)}{2} \quad [5.4.1]$$

where κ is a constant, power is in Watts, pressure is in mTorr, and Area is in square millimeters. Recall from the discussion of coulombic particle theory that the particle-particle spacing is approximately equal to the Debye length (λ_D). Assuming a uniform particle spacing, constant particle concentration, n_p , and the polyhedral cross section as shown in Figure 5.2.12, the trap cross section can be approximated as:

$$\text{Area} = \frac{n_p \lambda_D^2}{2} \quad [5.4.2]$$

For a constant concentration of particles, it appears that:

$$\lambda_D^2 \propto \kappa' - (W)^{1/4} P \quad [5.4.3]$$

Recall that the Debye length is given by:

$$\lambda_D = \left(\frac{k_B T_e}{4\pi n_e q^2} \right)^{1/2} \quad [5.4.4]$$

Hence the electron temperature and the electron density can be experimentally related to power and pressure as:

$$\frac{T_e}{n_e} \propto \kappa' - W^{1/4} P \quad [5.4.5]$$

over the range of pressure (9-30 mTorr) and powers (30-150 W) used in this particular system. From this evaluation, it is found that as pressure or applied power are increased, the average electron energy increases but the total electron density decreases. This is an

interesting concept in that it allows the functionality of the plasma energetics and the reactor operating conditions to be determined by experimentally evaluating the behavior of the particles. It has been only recently observed that the particles will confine in localized regions where the plasma potential is the highest in the chamber [78]. A natural extension of this result is the concept of possibly measuring the potential of the plasma by observing the behavior of the trapped particles.

Equation 5.4.5 is purely an empirical result. To validate this result, one must turn to the parametric plasma relationships discussed in Chapter 2.1. Recall Equation 2.1.8 which relates the average electron density to power and pressure:

$$\bar{n}_e = \frac{W}{qV(4 \times 10^{-10})} \frac{p^{1/2}}{E^{3/2}} \left(\frac{2m_e}{c} \right)^{1/2} \quad [2.1.8]$$

A theoretical relationship for T_e/n_e can be constructed by dividing Equation 2.1.7 by Equation 2.1.8:

$$\frac{T_e}{n_e} = \frac{qV(4 \times 10^{-10})c^{1/2}}{(2m_e)^{1/2}} \frac{E^{5/2}}{Wp^{3/2}} \quad [5.4.6]$$

To first order, the electric field can be approximated from a particle force balance:

$$Q_p E = \frac{\pi}{6} \rho g d_p^3 \quad [5.4.7]$$

Substituting for the charge per particle and solving for E yields:

$$E = \frac{\pi}{6} \rho g d_p^3 \frac{1}{5.13 \times 10^{-12} \frac{d_p}{2} T_e^{0.85} T_i^{0.15}} \quad [5.4.8]$$

The electron temperature is a function of the electric field and the chamber pressure, Equation 2.1.7. Substituting Equation 2.1.7 into Equation 5.4.8 and solving for E:

$$E = \Xi p^{0.85/1.85} \quad [5.4.9]$$

where Ξ is a constant for monodispersed particles. Substituting [5.4.9] into [5.4.6] reveals a theoretical relationship between T_e/n_e and power and pressure.

$$\frac{T_e}{n_e} = \frac{\xi}{Wp^{1/2}} \quad [5.4.10]$$

where ξ is combination of constants. The theoretical development is consistent with the empirical result in that as pressure or power increases, T_e/n_e decreases. It is troubling, that

the form of the empirical equation does not exactly match the theoretical result, and is likely due to the simplified assumptions made in the empirical development.

The issue that the particle trap size is changing in the long time scale must still be dealt with. Presumably, the force driving the compression rate of the particle trap in the long time scale exists during the short time scale. However the long term force cannot be readily observed in the short time with the present laser light scattering experiments because the effect of the force on the particle trap size is an order of magnitude smaller than that of the plasma coming into equilibrium. To elucidate the phenomena governing the long term trap behavior and to determine whether or not this phenomena actually occurs in the short time scale, it is necessary to evaluate particle-particle interactions rather than the bulk particle trap behavior. Laser Doppler Velocimetry was used to parametrically evaluate the behavior of the trapped particles.

5.5 Laser Doppler Velocimetry

An Aerometrics Laser Doppler Velocimeter (LDV) is used in this work to measure two directions of particle velocity and local particle concentration at discrete locations within a particle trap. The laser probe volume can be traversed throughout the particle trap as shown earlier in Figure 5.2.9. The use of Laser Doppler Velocimetry to characterize plasma contaminants has been used by one other research group [53]. The use of LDV to explicitly measure the behavior of trapped particles during plasma ignition is a new

approach and as such, caution was taken to ensure that all of the data were statistically meaningful.

The measurement of particle velocity and concentration has been discussed previously in Chapter 3. The probe volume is placed at a single location in the particle trap and the velocity of particles passing through it is recorded. A plot of the azimuthal velocity of particles passing through a fixed location in the ground plane particle trap is shown in Figure 5.5.1.

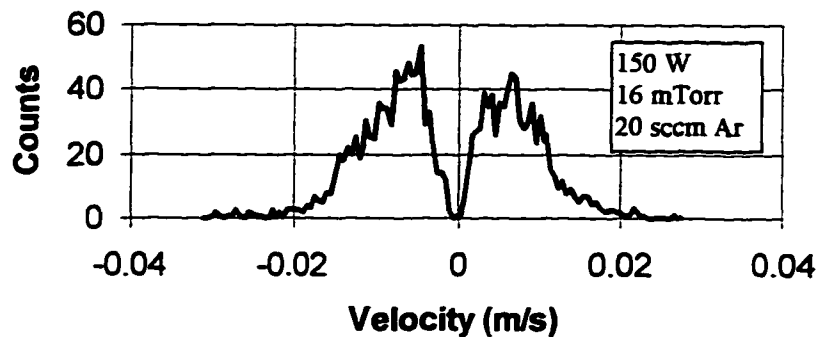


Figure 5.5.1 Azimuthal velocity histogram for ground plane particle trap

This representative histogram is taken from the center of the ground plane particle trap for a dusty plasma with 150 W continuous wave rf power, 16 mTorr, and 20 sccm Ar after the plasma has equilibrated. Note that the velocity histogram is bimodal. This bimodal behavior was independent of time. From this plot, it is difficult to reconstruct the path of the particles through the measurement volume; it appears that the particles are azimuthally oscillating. Considerable insight can be gained by simultaneously looking at a second dimension of the velocity. Figure 5.5.2 depicts the heads of two dimensional velocity vectors of 1000 particles passing through the control volume which is located in the center of the particle trap for the same experimental conditions as were used in Figure 5.5.1.

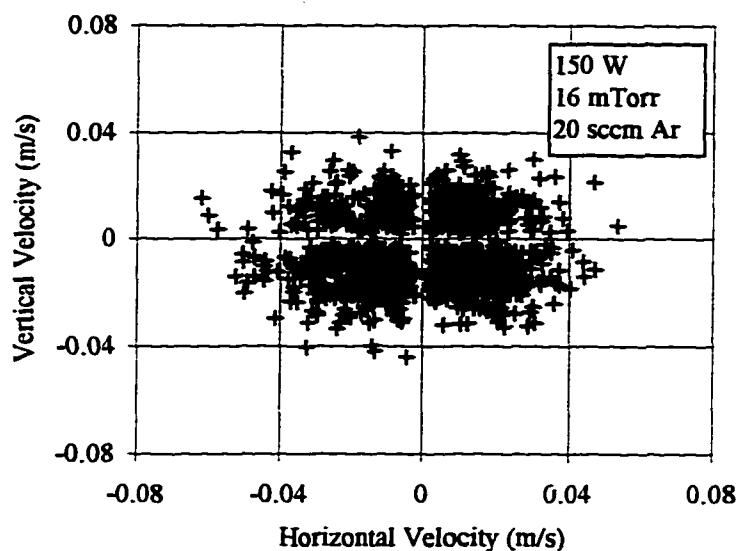


Figure 5.5.2 Velocity of particles passing through the LDV control volume

Notice that there is no preferential direction for the particles passing through the control volume indicating that there is no bulk flow of the particles. The lack of preferred particle direction was valid for all times after the plasma was ignited.

In order to compare the velocity behavior of the particles at one point in the particle trap to another point, it is necessary to extract information from plots like that of Figure 5.5.2 which can be constructed at every measured point. One approach is to determine an average particle velocity passing through the control volume. Because the particle velocity is insensitive to direction, it is appropriate to take the average of the magnitude of the particle velocities. The fraction of particles, $J(V)$, having a velocity magnitude less than or equal to the stated amount is shown in Figure 5.5.3 and is taken from the data in Figure 5.5.2.

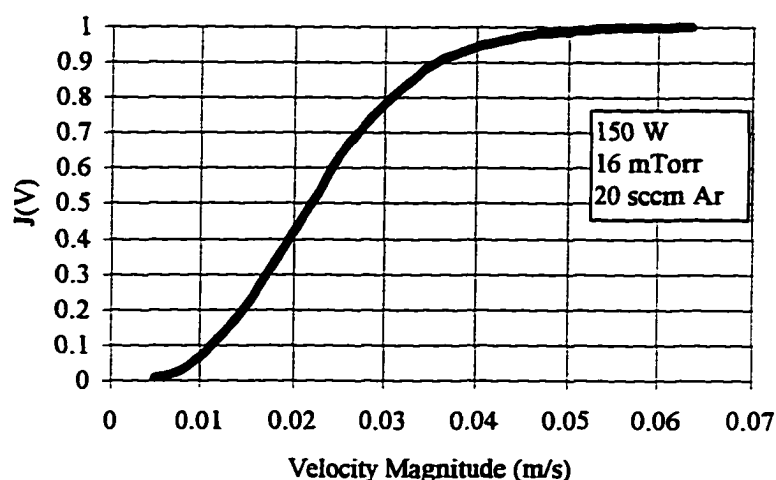


Figure 5.5.3 Fraction of particles having velocity magnitudes less than or equal to the stated amount

The average velocity magnitude, V_{50} , is then reported where $J(V) = 0.5$, the velocity magnitude at which half of the particles exhibit a lower velocity and half exhibit a higher velocity. For Figure 5.5.2 and Figure 5.5.3, the average velocity magnitude, is approximately equal to 2.2 cm/s. In general, determining V_{50} is a laborious task, especially if hundreds of plots must be constructed in order to map the velocity profile through the cross section of the particle trap. Recall that the particle velocities appear to be insensitive to direction. The average velocity of particles having a component of velocity in the positive azimuthal direction should be similar to the averages of particle velocity components in any other direction, and should be similar to V_{50} . For the current experiment, $V_{50} = 2.2$ cm/s, $V_z^+ = 1.54$ cm/s, $V_z^- = -1.84$ cm/s, $V_\theta^+ = 1.12$ cm/s, $V_\theta^- = -1.45$ cm/s. The directional average velocity component values can be easily obtained from

the experiments. The directional average velocities are lower than V_{50} , but that is to be expected because the value for V_{50} is obtained from the magnitudes of the particle velocity vectors whereas the individual direction averages are computed from the normal components of the particle velocity along each axial direction. The normal components of the particle velocity vector are necessarily smaller than the magnitude of the velocity by geometrical arguments. The velocity data reported throughout the rest of the chapter will be the average of the negatively directed azimuthal component velocities. Trends drawn from this data are consistent with trends drawn from V_{50} and the other directed velocity averages.

In Chapter 2, it was introduced that Boufendi *et al.* have previously performed research using a laser Doppler technique [53]. Their histograms did not show a bimodal behavior as was shown in Figure 5.5.1. This is likely due to the hardware settings and resolution of their equipment (as they were more interested in the behavior of particles once the plasma is extinguished) rather than a physical difference between the behavior of particles in their system and that of the present work. When Boufendi *et al.* averaged their particle velocities, they did so as if the particle histogram was unimodal rather than bimodal. Their averaging strategy will give an average particle velocity that is much lower than the bimodal directional averages discussed above or V_{50} .

In order to report trends, it is important to determine how many particles must be sampled in order to represent a statistically meaningful average. In an experiment where the plasma had reached the quasi-equilibrated state, the average velocity was recorded as a

function of the number of particles sampled at a single location. The error in the average velocity measurement for n sampled particles relative to the average velocity for 2000 sampled particles is given as:

$$\left| \frac{\bar{V}_n - \bar{V}_{2000}}{\bar{V}_{2000}} \right| = \text{Error} \quad [5.5.1]$$

It was observed that less than 4% error occurred if 500 particles are sampled. It is fairly remarkable that even if only 30 particles are sampled, the error remains less than 10%. For this work, at least 500 particles are sampled before an average velocity is computed.

Average velocity profile maps can be constructed by sampling particle velocities at discrete locations in a cross section of the ground plane particle trap. The cross section is a slice out of the toroidal ring bounded radially and axially. Figure 5.5.4 depicts the location of the slice and the direction of velocities being measured. In all locations in the cross section of the particle trap, the quality of the signal from light scattered off of the particles remained consistent. The signal quality degraded only if the particle concentration exceeded that which maintains only one particle in the probe measurement volume at a time. In Chapter 4.2, the various hardware parameters used for data collection were stated as being optimal. These parameters were selected in order to maintain the highest possible data rate while filtering out the noise of the clean room, rf noise from the plasma, and stray signals generated from the emission of the argon plasma while still maintaining the

bimodal behavior of the particle velocity histogram. Steps were taken to make sure that the velocity histograms were genuine and not due to over-powering the photomultiplier tubes, oscillations of piezos, or noise from amplifiers. As an example, to validate the signal, a velocity histogram was taken during an experiment. Immediately following, the transceiver was rotated by 90 degrees and the experiment was repeated. By rotating the transceiver, two completely independent sets of optic fibers, photomultipliers, filters, and electronic processing equipment are used to process the velocity information. The velocity information was considered genuine when the histogram from the green beams exactly matched the histogram from the rotated blue beams.

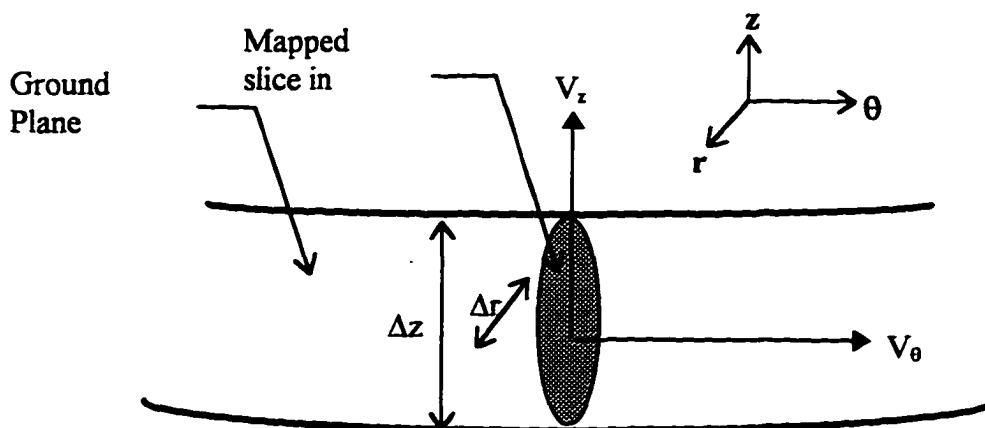


Figure 5.5.4 Location of mapped slice and measured velocity directions

A contour plot is shown in Figure 5.5.5 where lines of constant average velocity (m/s) are reported through the cross section of the particle trap.

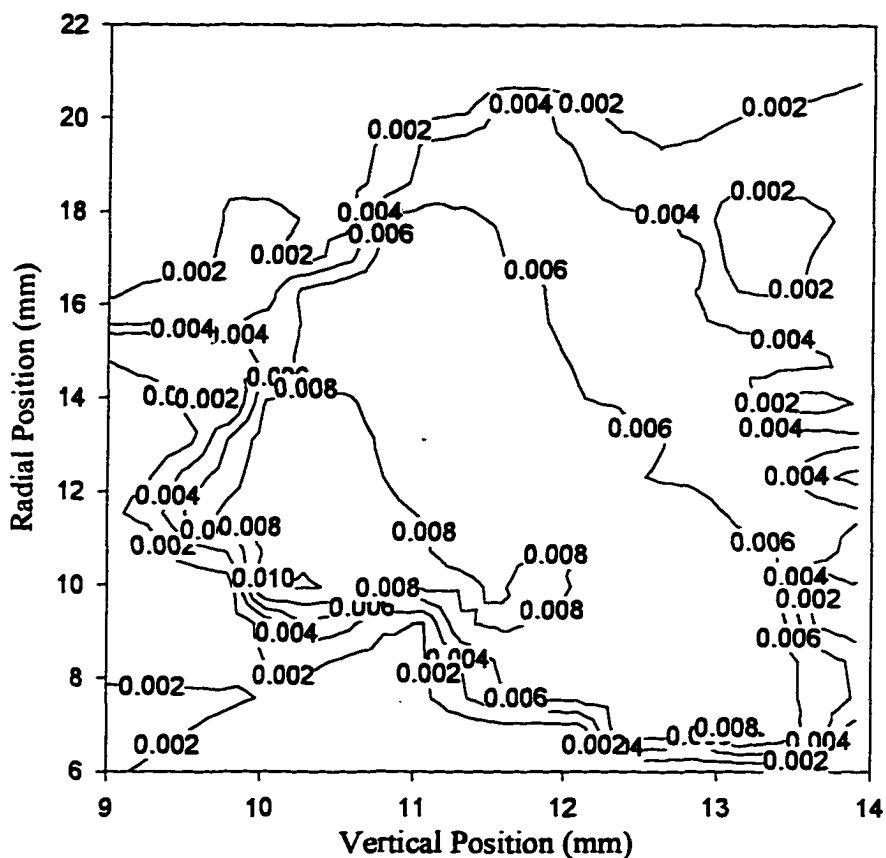


Figure 5.5.5 Contour plot of clockwise azimuthal average velocity (m/s) for 50W, 20 mTorr, argon plasma

Evaluating the average particle velocities as a function of vertical position above the electrode at constant radial position (Figure 5.5.6) shows that as the particles move closer to the electrode or to the Debye sheath, they generally exhibit higher average velocities over the particles near the bulk plasma.

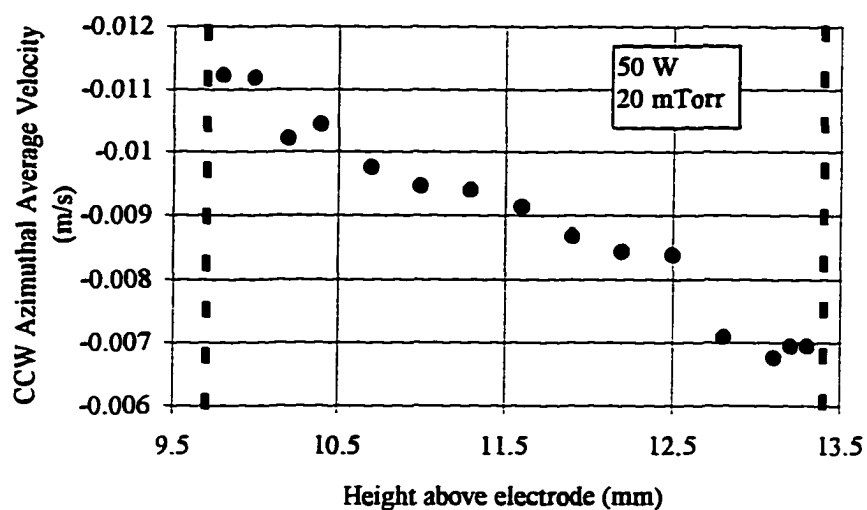


Figure 5.5.6 Vertical LDV scan at constant radius (13.0 mm)

Similarly, evaluating the average particle velocities as a function of radial position away from the edge of the powered electrode for constant vertical position (Figure 5.5.7) shows that the particles near the powered electrode exhibit slightly higher average velocities over those particles near the chamber wall. In Figures 5.5.6 and 5.5.7, the boundary of the particle trap is denoted by the dashed lines.

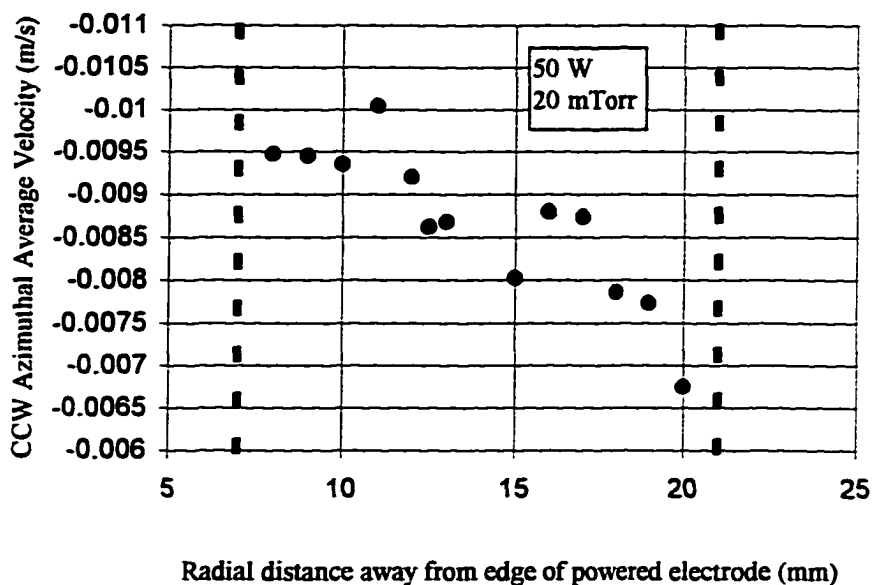


Figure 5.5.7 Radial LDV scan at constant vertical position (12.0 mm)

Line scans along the vertical and radial axis of the particle trap can be used to describe how the velocity behavior of the particles changes as a function of power and pressure. Figure 5.5.8 shows average velocity versus vertical position for various pressures at 30 W rf power. The maximum average velocity over the line scan is taken from Figure 5.5.8 to show the average particle velocity dependence on pressure.

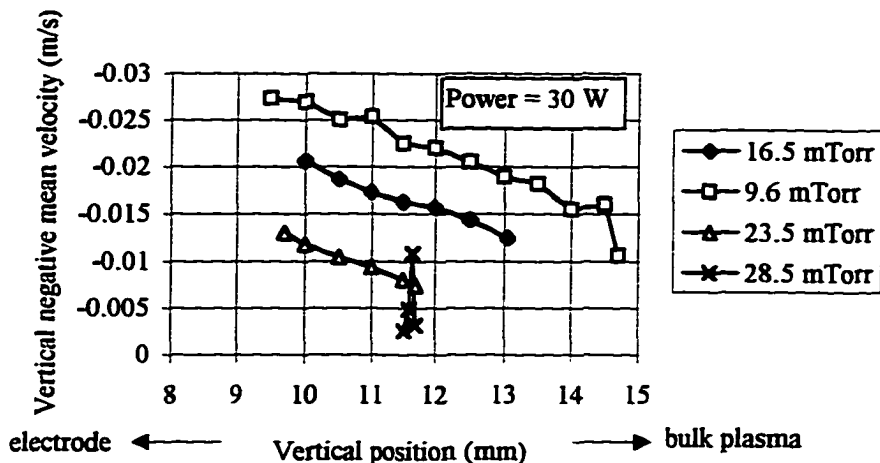


Figure 5.5.8 Particle velocity profiles for a vertical traverse through a ground plane particle trap at a plasma power of 30 W

A plot of the mean particle velocity versus chamber pressure for multiple experiments with various particle concentrations is shown in Figure 5.5.9.

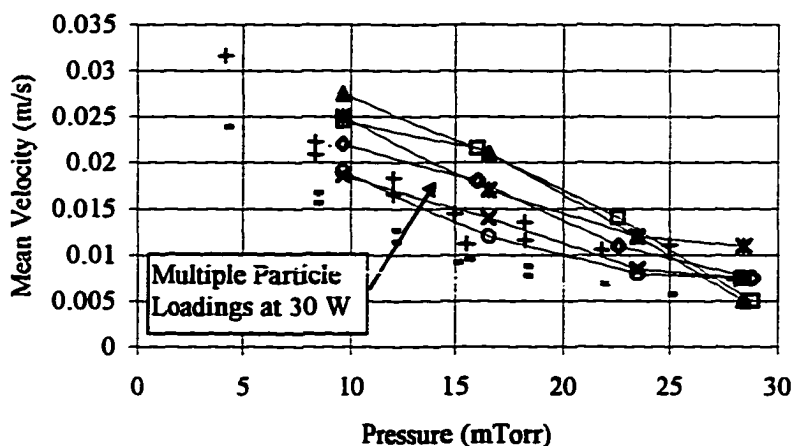


Figure 5.5.9 Mean particle velocity as a function of pressure for constant power

As pressure is increased for a constant number of particles, the average particle velocity decreases. There is a large spread of the experimental data, however, this is explained by the fact that there is a dependence of average velocity on the total number of particles in the plasma and that the experimental data set includes many different initial loadings of particles. Note that the overall change in particle velocity due to a change in pressure is greater than that due to a change in total particle number. Also note that the effect of total number of particles loaded in the plasma on velocity is more pronounced at low pressures compared with high pressures.

As with pressure, the maximum average velocity over a line scan of the particle trap can be determined as a function of power at a constant pressure of 16.5 mTorr.

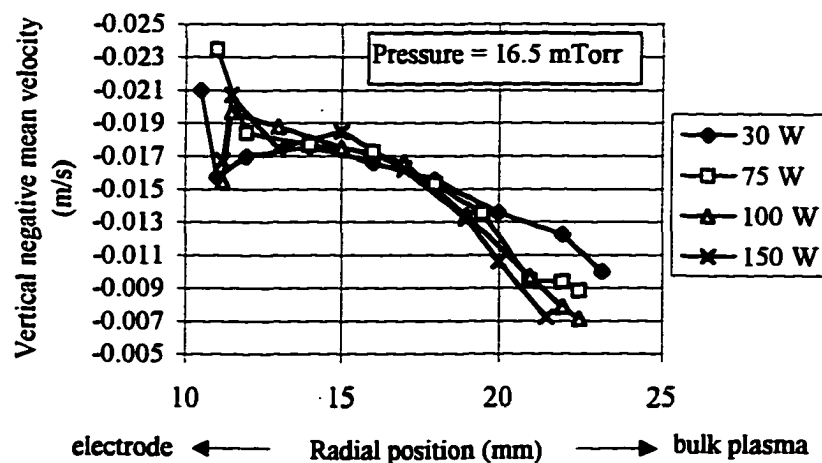


Figure 5.5.10 Radial velocity profile for varied power at 16.5 mTorr

Although the change is small, there is a slight increase in the average particle velocity with an increase in power for a fixed number of particles in the plasma. Figure 5.5.11 depicts the trend of increasing particle velocity with an increase in power over a wide range of particle loadings for constant pressure.

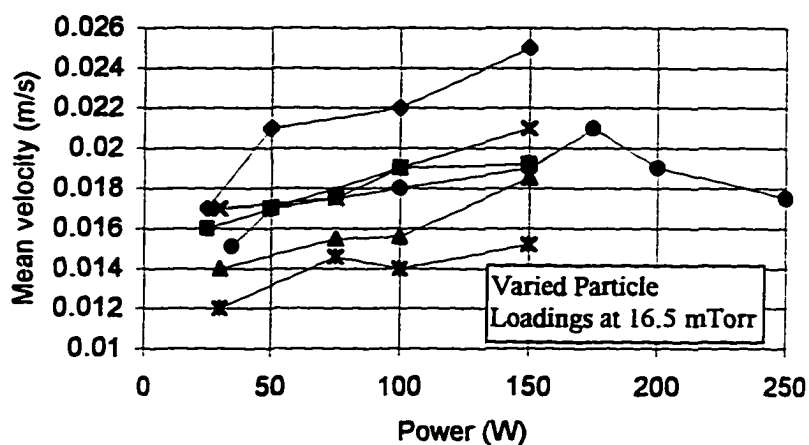


Figure 5.5.11 Mean particle velocity for varied power at constant pressure

Note that a change in the number of particles in the plasma has a large effect on the maximum average particle velocity as compared with the effect due to a variation of power. Additionally, the effect of total particle number on velocity is more pronounced at high powers than at lower powers.

Particle concentration is measured according to Equation 3.3.3. As with velocity, it is important to determine how many particles must be sampled in order to give a statistically meaningful measurement of the local particle concentration. The error

associated with calculating the concentration (C) after n particles are sampled relative to the concentration after 2000 particles are sampled is given by:

$$\text{Error} = \left| \frac{C_n - C_{2000}}{C_{2000}} \right| \quad [5.5.2]$$

It was found that if n was less than 100, a 25% error occurred, but for n greater than 200, only an 8% error occurred. Since the velocity measurement required sampling of 500 particles for a meaningful average, all of the concentration measurements will be reported after 500 particles are sampled.

The local concentration is measured for a plasma at quasi-steady state at various powers. It is seen clearly in Figure 5.5.12 that as the power is increased, the trap thickness compresses and the local particle concentration increases, indicating that as the power is increased, the inter-particle spacing decreases.

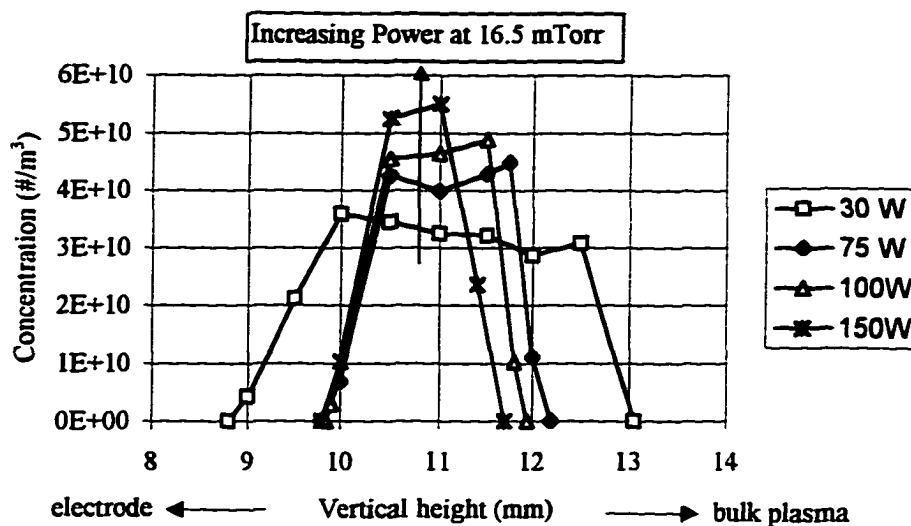


Figure 5.5.12 Local concentration of particles in a ground plane particle trap

Particle trap compression may occur for one of two reasons: either the charge per particle decreases, and hence the repulsive forces acting between the particles decreases so the particles can move closer to each other, or the plasma potential increases and the spatial gradient of the plasma potential becomes steeper, which would confine the particles to a smaller local region in the plasma. The bulk concentration of the particle trap versus power is plotted in Figure 5.5.13 for two experiments with different initial loading of particles.

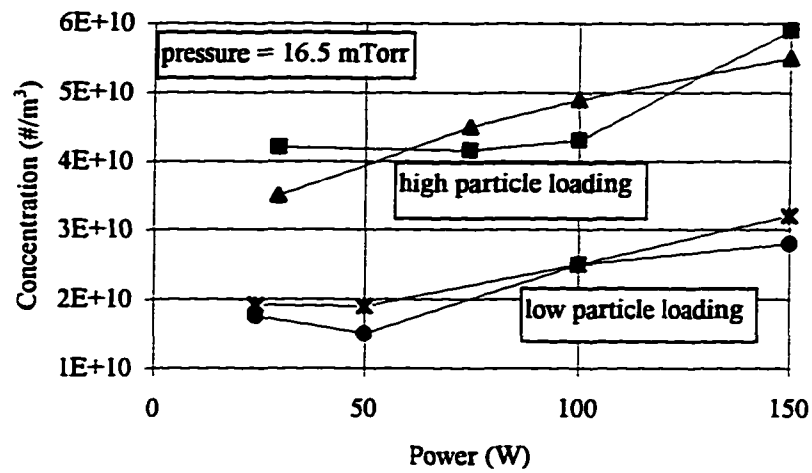


Figure 5.5.13 Maximum local particle concentration for varied power at 16.5 mTorr

Local concentration line scans are shown for various pressure settings in Figure 5.5.14 for constant power (50 W).

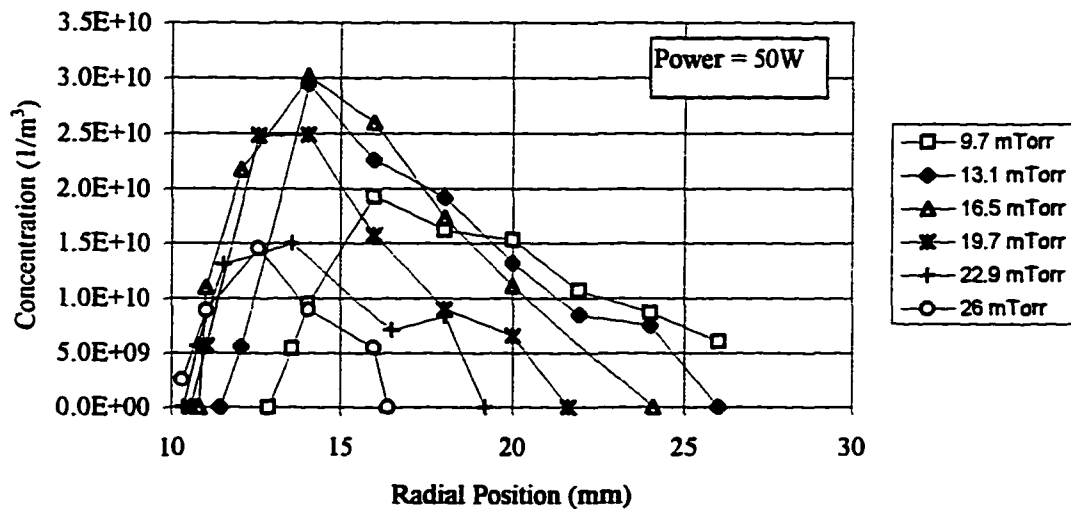


Figure 5.5.14 Local particle concentration profiles in a ground plane particle trap at 50 W

The change in the maximum local particle concentration as a function of pressure is shown in Figure 5.5.15 for various initial particle loadings and a constant power of 50 W.

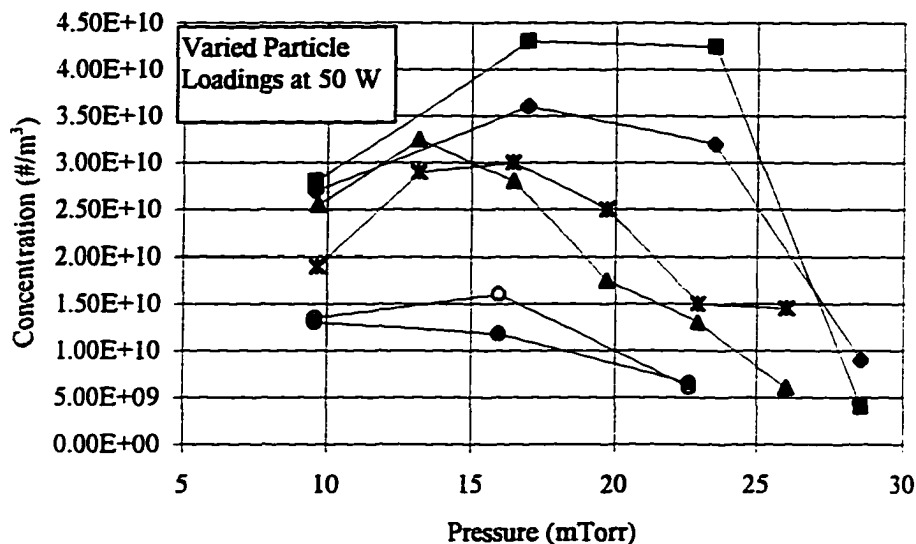


Figure 5.5.15 Maximum concentration in a ground plane particle trap as a function of pressure at 50 W

In general, the local particle concentration first increases from the low pressure value (9 mTorr) and then decreases. These trends hold with the maximum local particle concentration and the line scan averaged local particle concentration. There was a concern that the concentration decrease at high pressures is an artifact of the method of calculating the concentration. Recall, that the measuring the concentration relies on the movement of particles through the measurement control volume. We saw earlier that as pressure is increased, the average velocity of the particles decreases. As the particles tend to a static

state, the method for measuring the particle concentration breaks down. Nevertheless, although this trend is questionable, the work of Thomas and Morfill [59] shows a similar trend. Figure 5.5.16 is generated from data in [59] and shows that as the pressure is increased, the area density of particles decreases.

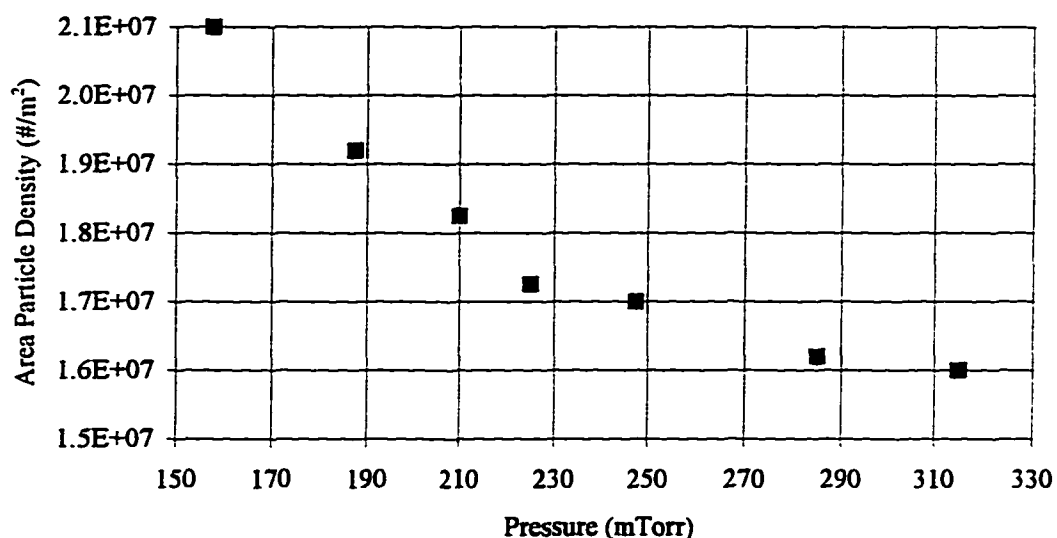


Figure 5.5.16 Area particle density as a function of pressure at constant power. Figure adapted from reference [59]

Thomas and Morfill's measurements were made by taking photographs of particles illuminated with a laser sheet, and counting the number of particles in a cross section of the particle trap. Considerable scatter in their data occurred at low pressures, which is a regime where the present research indicates that the particles exhibit high velocities.

The temporal behavior of the particle concentration can be determined by following the local particle concentration at fixed points in the particle trap as a function of time. The temporal behavior of the local particle concentration in the particle trap depends on what part of the particle trap is being observed. Recall that the particle trap is constantly shrinking in time. If a point in the center of the trap is followed, there is initially an increase in the concentration followed by a decrease. However, if a location near the edge of the trap is followed, only a decrease in time is observed. This behavior indicates that initially, since the particles are not generated in the system, the particles must be moving from the edge of the trap to the center of the trap resulting in a shrinking of the trap. One would expect that in the long time, the particle concentration in the trap would asymptote to a certain value and stay there for the duration of the experiment. This is not the case; instead of going to an asymptotic value, the local particle concentration ends up decreasing everywhere in the particle trap.

The temporal behavior of the average particle velocity can now be explained. It was observed that the particles near the bulk plasma exhibited lower average velocities than the particles near the electrode. If the average particle velocity is plotted in time for a fixed location in the trap, it is observed that the velocities tend to decrease as the fixed point becomes closer to the boundary of the shrinking particle trap.

Recall that some of the possibilities which explain the shrinking of the particle trap are that the particles are agglomerating, the particles are packing closer together, the particles are moving to more preferred locations in the particle trap, and/or the particles

are falling out of the particle trap. For the reasons explained above, the shrinking of the trap cannot be explained by particles constantly moving closer together because this would give a temporal effect of the local particle concentration always increasing.

For the large 10.2 μm particles used in this work, it was observed that the particles are not agglomerating. Figure 5.5.17 is a FESEM micrograph of one of many PSL particles collected on the electrode after a ten hour reaction at 20 mTorr and 50 W.

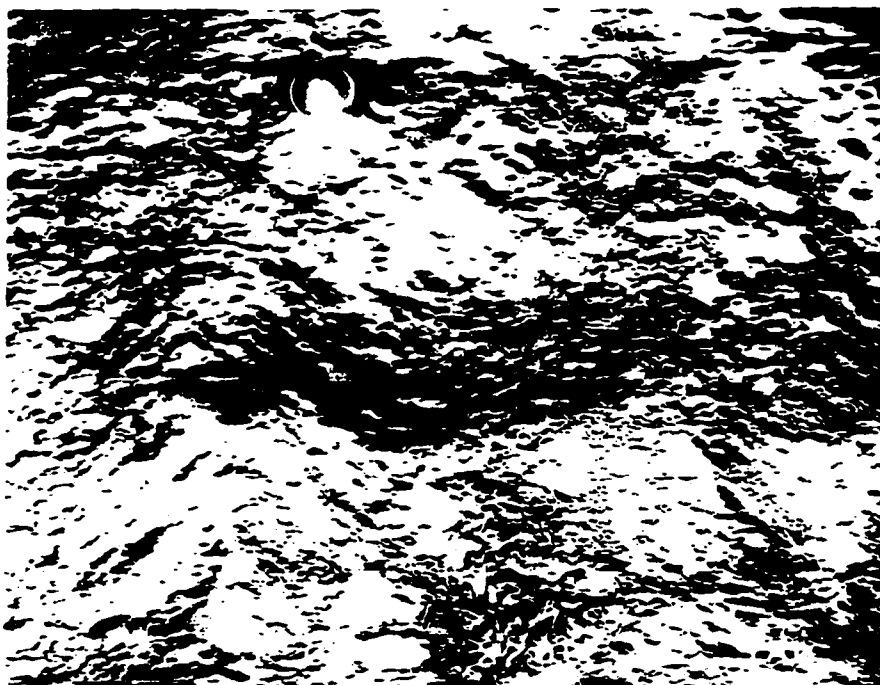


Figure 5.5.17 FESEM micrograph of a PSL particle exposed to a plasma showing no signs of agglomeration

As was explained in Chapter 2, the large particles will tend to fall on the electrode rather than sweep away in the exhaust. If the particles agglomerate, it is definitely expected that they will fall onto the electrode rather than go anywhere else in the chamber.

Considerable effort was taken to search for new particle traps or preferred locations when the reactor operating parameters were varied. In all cases explored in this research, new traps were not observed. It is concluded from the experimental evidence that the particles must be falling out of the particle trap during the course of the experiment. A physical explanation for this will be postulated in Chapter 5.8.

5.6 Summary of Experimental Results

The following trends have been observed using Laser Doppler Velocimetry and Laser Light Scatter techniques.

Table 5.6.1 Summary of experimental results

Experimental Result	Technique	Pressure Increase		Power Increase	
		Current Research	Other Researchers	Current Research	Other Researchers
Initial Area Decrease Rate	LLS/LDV	↓		↑	
Long Term Decrease Rate	LLS/LDV	↑↓		↓	
Equilibration Time	OES/LLS	No Change		↓	
Total Cross Sectional Area	LLS/LDV	↓	↓ [80] LLS	↓	↓ [22] LLS
Average Concentration	LLS/LDV	↑↓	↓ [59] LLS	↑	↑ [22] LLS
Average Velocity	LDV	↓		↑	

Note that independent of power or pressure, the area of the trap decreases with time. In the early times after plasma ignition, the trap size decrease is dominated by the plasma going to equilibrium. At long times, the trap size decrease is likely to occur because the particles are falling out of the particle trap. One possible explanation for particle fallout is that the charged particles may collide if they have enough kinetic energy

to overcome repulsive electrostatic interactions with neighboring particles. If the particles approach to within a Debye length of each other, they will induce dipole surface charging and then electrostatically attract each other. The collision of the particles may result in a partial charge transfer to one particle at the expense of the other. If one particle temporarily loses some of its charge, it will begin to fall towards the electrode because the force required to keep it electrostatically trapped is reduced. Effectively, the instantaneous particle loss of charge resembles pulsing the plasma at a certain frequency equal to the charge-decharge frequency of a particle. The partially charged particle will immediately begin recharging back to its asymptotic surface potential, however if the particle can enter the (electron-free) Debye sheath surrounding the electrode before it accrues the minimum trapping surface charge, it may deposit on the wafer. To determine the ability of a particle to escape the trap, the time it takes for an uncharged particle to exit the trap is with the time it takes to regain the necessary charge. This analysis will be discussed in Chapter 5.8.

During the long time scale, the experimentally observed decrease of the trap cross section or the loss of particles from the trap can be explained based on the representative velocity and concentration trends described previously. Two ideas must be extracted from the experimental trends, namely, what is the frequency of particle collision and how strongly are the particles held in the trap.

For the case of increasing power, both a concentration of the trap and slightly higher particle velocities over the low power experiments are observed. When the trap

concentration increases, it is a good indication that the system of charged particles is becoming more ordered. The results shown here are consistent with the fact that the plasma potential for high powers increases over the low power plasma potential, and hence the plasma exhibits a stronger hold on the particles. As power increases, the potential well in which the particles are trapped grows deeper, making escape difficult. The velocity increase indicates that the particles might exhibit higher collisional frequencies over the low power case which would indicate higher loss rates. However since the plasma has a stronger hold on the particles, they cannot easily leave the trap and so in the long time scale, the particle loss rate is lower for high powers versus low powers.

For the case of pressure, a nonlinear behavior in the local particle concentration and an asymptotic behavior in the velocity are observed. Starting with the low pressure case (10 mTorr), the particles occupy a large volume in the trap which indicates that the particles are weakly confined by the plasma. The high velocities indicate that there are not many near neighbors around the particles to slow them down after a previous particle-particle interaction. One would expect that since the particles are not held very tightly, they would easily escape the trap, however the particles must go through an inelastic charge transfer collision before falling out of the trap. The local particle trap concentrations are relatively low, so the particles exhibit infrequent near neighbor interactions and hence the loss rate is low. At the other extreme where the pressure is high (30 mTorr), the particles are nearly static. The region occupied by the particles is also smaller, so it is expected that the plasma has a strong hold on the particles. The low

velocities and small trap size explain a low cross section decrease rate. In the middle pressure region (16 mTorr), moderate velocities and a medium trap size are observed, resulting in a loss rate that is slightly higher in this range over the high pressure range and the low pressure range.

5.7 Particle Motion

Now that there is an experimental understanding of how large particles trapped in a plasma interact as a function of basic plasma operating parameters, it is desired to expand on the theoretical developments in Chapter 2.7 in order to account for particle velocity changes as a function of power and pressure. If the large particle motion is actually dominated by coulombic interactions, a particle velocity relationship based on plasma parameters should be straightforward.

Starting from equation [2.7.3], the velocity can be written in terms of a non-dimensional length, x^* , where the separation distance between two charged particles is scaled by the Debye length, λ_D :

$$V = \left[\frac{Q_p^2}{4\pi\epsilon_0 m_p \lambda_D} \frac{1}{x^*} \left(\frac{x^*}{x_o^*} - 1 \right) \right]^{1/2} \quad [5.7.1]$$

Substituting Equation 2.4.10 for the Debye length and Equation 2.3.1 for the particle charge results in:

$$V = \frac{2.56 \times 10^{-10} r_p T_e^{0.85} T_i^{0.15} n_e^{0.25} q^{0.5}}{\left(\frac{4}{3} \pi \rho_p r_p^3 \right)^{1/2} \pi^{0.5} \epsilon_0^{0.75}} \left[\frac{1}{x^*} \left(\frac{x^*}{x_o^*} - 1 \right) \right]^{1/2} \quad [5.7.2]$$

Now, it is possible to substitute in a relationship for the average electron density, Equation 2.1.8, and the electron temperature, Equation 2.1.7:

$$V = \frac{1.6 \times 10^{-7} c^{0.475} T_i^{0.15} E^{0.225}}{\bar{V}^{1/4}} \left(\frac{W}{p^{1.9}} \right)^{1/4} \left[\frac{1}{x^*} \left(\frac{x^*}{x_o^*} - 1 \right) \right]^{1/2} \quad [5.7.3]$$

If the initial separation of the charged particles is assumed to be the Debye length ($x^*=1$) and the velocity is reported after the particles are a total of two Debye lengths away from each other ($x^*=2$), and if the volume of the particle trap, the electric field strength, and the ion temperature remain constant, it is possible to show the dependence of velocity on varied pressure for constant power at 50 W (Figure 5.7.1) and for varied power at constant pressure of 16.5 mTorr (Figure 5.7.2). In both cases, the velocity is normalized to the velocity predicted at 50W and 16.5 mTorr.

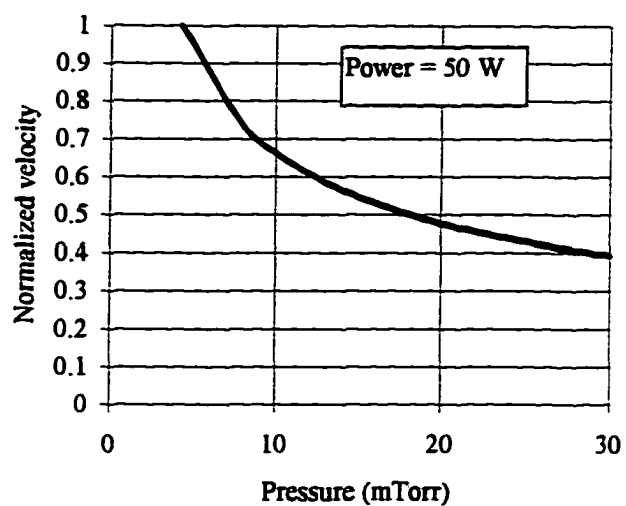


Figure 5.7.1 Theoretical particle velocity for varied pressure at constant power

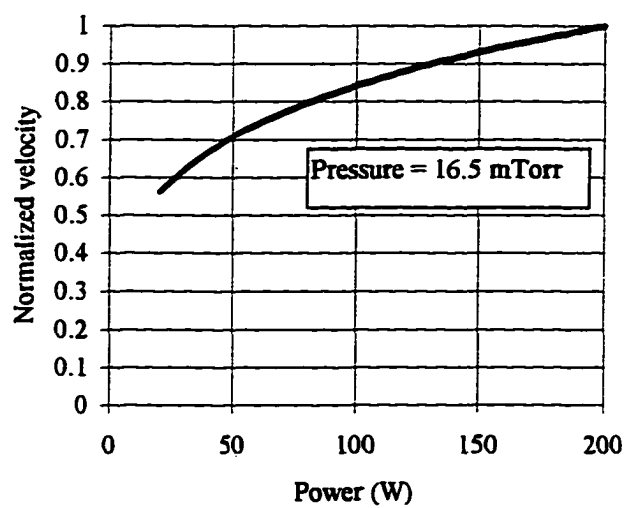


Figure 5.7.2 Predicted particle velocity for varied power at constant pressure

The agreement between the experimental results and the model is quite remarkable considering its simplicity and that it contains only fitting parameters which has been normalized out of the graph (Figure 5.7.3).

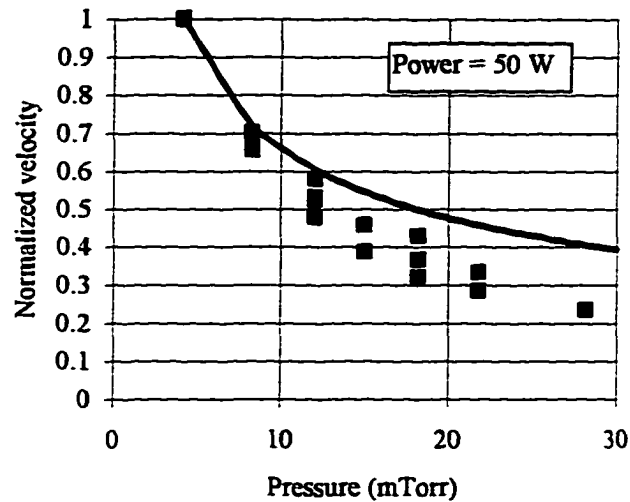


Figure 5.7.3 Comparison of experimental results and model: normalized velocity versus pressure at constant power

The normalized velocity can be plotted for the experimental results and the model for power at constant pressure (Figure 5.7.4). It is important to note that the theoretical model predicts velocity without any fitting parameter to match the data. Again, the agreement is remarkable.

Considering that the Coulomb model can predict the order of magnitude of the particle velocities measured in this work and particle velocities reported by Boufendi *et al.* [53], and because the model can predict the experimental trends with varied power and pressure, it is with high confidence that the large particle motion in a plasma can be

attributed to electrostatic interactions with neighboring particles. The ability to predict how particles will move in a plasma is a very powerful tool, which can be used to describe experimental conditions for which particle collisions and/or agglomeration events are likely. This model holds only for large particles (having diameters greater than $0.1 \mu\text{m}$). For particles smaller than $\sim 0.1 \mu\text{m}$, Brownian motion is the dominating mechanism governing particle motion, particle collisions, and particle agglomeration.

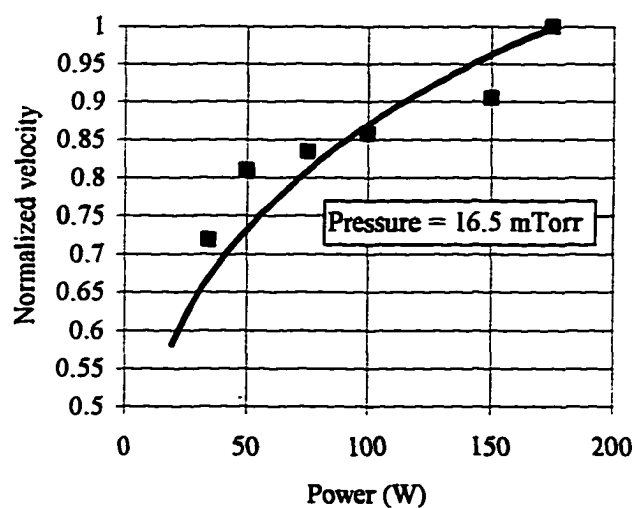


Figure 5.7.4 Normalized velocity model predictions and experimental results for varied power at constant pressure

5.8 Charging Particle/Deposition Model

Earlier, it was determined experimentally that the probable reason why the particle trap cross section decreases in time is because the particles fall out of the particle trap.

One reason why this may occur is because a charge transfer from a prior particle collision will result in a reduction of the force causing the particles to trap in the first place. Assume a particle in the particle trap underwent a particle collision and ended up losing its charge. The probability of a particle collision event will be investigated in Chapter 5.9. The time for a particle to charge, or in this case recharge, has been estimated by Goree [79]:

$$\tau = K_t \frac{(k_B T_e)^{1/2}}{d_p n_e} \quad [5.8.1]$$

where τ is the estimated time for a particle to reach $(1-e^{-1})$ of its equilibrium charge and $K_t = 2.05 \times 10^3 \text{ s} \cdot \mu\text{m} \cdot \text{cm}^{-3} \cdot \text{eV}^{-1/2}$ for an argon plasma and $T_i/T_e = 0.5$ as given in [79]. Using Equation 5.8.1 and applying the experimental parameters used in the present research, it is possible to estimate the time constant which describes how long it takes for an uncharged particle to charge. If the electron temperature is assumed to be 4 eV, the particle diameter to be 10.2 μm , and the electron density to be $1 \times 10^{16} \text{ \#/m}^3$, then the time constant is approximately 0.04 μs .

While the particle is uncharged, it can fall towards the electrode under the influence of gravity.

$$x - x_0 = v_0 t - \frac{1}{2} g t^2 \quad [5.8.2]$$

The maximum velocity observed experimentally in this work was approximately 5 cm/s. If the particle can fall into the Debye sheath before reaching an equilibrium charge, it will be able to fall all the way to the electrode. This is because the electron density in the Debye sheath is much lower than in the bulk plasma, therefore the flux of electrons to the particle surface will not allow it to recharge. If the particle is at the plasma-sheath interface (PSI) just before a collision, it may need to travel only a fraction of its diameter before it will enter the Debye sheath. The time required for the particle to travel a tenth of its diameter after a collision is approximately 3.3 μs . This time is slower than the actual time because the effect of ion wind is not accounted for. A probability of particle escape can be approximated by the ratio of the two time constants. Approximately 1% of the particle collisions at the PSI interface may result in the particle falling out of the particle trap. This may serve to explain the cross section of the particle trap decreases with time but the particle concentration does not increase.

5.9 Particle Agglomeration Model

It has been shown in Chapter 2 that there are many mechanisms which may govern the behavior of particles trapped in a plasma. For small particles (diameters less than $0.1 \mu\text{m}$), Brownian motion describes the behavior. Collision and agglomeration events of Brownian particles is well known [81]. For larger particles, it has been shown theoretically and confirmed experimentally that the likely mechanism for particle motion is Coulombic particle interactions. Calculating collision and agglomeration probabilities for larger particles is not straight forward. So as to make some progress on the subject, the theoretical work of Chapter 2 will be expanded to evaluate under what conditions it is possible that the particles will collide.

For two electrostatically interacting particles, the velocity of the second particle relative to a fixed particle as a function of distance, x , starting at an initial closest point of approach distance, x_0 , was given by Equation 2.7.3 and Figure 2.7.3. The same equation will hold whether the particles starting from rest at their closest point of approach repulse each other, or whether two particles at infinite separation are approaching each other. The closest point of approach which will give a hard collision of the particles is given by the sum of the particle radii ($x^*=2r_p/\lambda_D$). So for two infinitely separated particles, it is possible to calculate the

minimum approach velocity needed so that the particles will experience a hard collision.

Using Equation 2.7.3, it is possible to determine the required particle approach velocity for a hard collision:

$$V = \left(\frac{Q_p^2}{8\pi\epsilon_0 m_p r_p} \right)^{1/2} \quad [5.9.1]$$

For a constant density particle greater than approximately 0.1 μm in diameter, the hard collision approach velocity varies as $1/r_p$:

$$V = \frac{8.385 \times 10^{-6} T_e^{0.85} T_i^{0.15}}{\rho_p^{1/2} r} \quad [5.9.2]$$

The hard collision approach velocities are shown as a function of particle size in Figure 5.9.1 for an electron temperature of 4 eV, an ion temperature of 0.0258 eV, an electron concentration of $1 \times 10^{16} \text{ 1/m}^3$, and a particle density of 1.9 g/cm^3 for amorphous silicon (dark line) and PSL particles (dotted line).

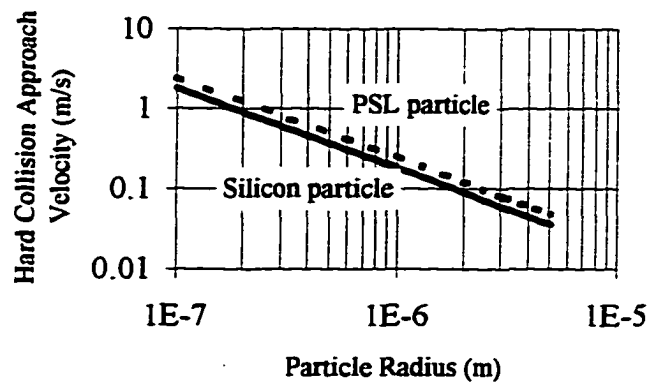


Figure 5.9.1 Hard collision approach velocities as a function of particle size for $T_e = 4 \text{ eV}$, $n_e = 10^{16} \text{ 1/m}^3$, and $T_i = 0.0258 \text{ eV}$

Notice in Figure 5.9.1 that as the particle size gets smaller, the probability of a hard sphere particle collision becomes more difficult. This does not say that a hard collision will not occur, rather only that the maximum velocity of the particles must be on the order of 1 m/s in order that a collision occur.

In the analysis in Chapter 5.8, it was assumed that a particle collision could occur. If that was indeed true, it was possible that the particles could fall out of the particle trap and contaminate the wafer. It is shown in Figure 5.9.1 that for the 10.2 μm PSL particles used in this work, an approach velocity of approximately 4-5 cm/s is required for a collision to occur. It was shown in Figure 5.5.3 that the fraction of particles having a velocity magnitude less than 4 cm/s was 0.95. In other words, about 5% of the particles will exhibit a velocity that is required in order for a particle collision to occur.

In order to determine the frequency of particle collisions as a function of power or pressure, it is necessary to compare the average particle velocity (Equation 5.7.4) and the hard sphere particle velocity (Equation 5.9.2). For constant electric field strength, the average velocity varies with pressure as $1/p^{0.475}$, whereas the hard sphere collision velocity is proportional to $1/p^{0.85}$. Therefore, with an increase in pressure, both the average velocity and the hard sphere collision velocity will decrease, however, the collision velocity decreases faster than the average velocity. Therefore, with an increase in pressure at a constant electric field strength, more particles have the potential to undergo a collision, although the total energy of the collisions will be small.

With an increase in power at constant electric field strength, the average particle velocity increases but the hard collision velocity remains constant. Therefore, as power is increased, it is expected that more particles will have sufficient energy to overcome electrostatic repulsive interactions and will collide.

If the particles are allowed to stick together after a collision, the model predicts that for large particles, collision and agglomeration events will increase for increased power or decreased pressure.

CHAPTER 6

Conclusion

In this work, efforts were taken to understand how particles move while trapped in the plasma so that predictions of particle agglomeration can be made. To accomplish this goal, Laser Light Scatter, Optical Emission Spectroscopy, and Laser Doppler Velocimetry were used to study trapped particle behavior. Behavioral trends for variations in the reactor operating conditions (power and pressure) were determined. Specifically, particle trap size, spatially resolved particle velocity in two directions, spatially resolved local particle concentration, particle trap cross section short and long term compression rates, plasma emission intensity-time profiles, maximum velocity, and maximum particle concentration were determined as a function of pressure and power.

In Chapter 2, three theories were presented and developed in order to explain the observed the motion of particles in a plasma environment. The first theory was the thermal energy theory first presented by Boufendi et al. [53]. The second theory was based on individual charged particle-molecular interactions. It was determined that these theories are appropriate for describing the motion of small particles, however do not properly

explain the motion of large particles (having diameters greater than approximately 0.1 μm). An important phenomena where the argon atoms polarize in the presence of the charged particles was explained in the second theory, that to the author's knowledge, has not been previously discussed. The third theory described particle motion due to interactions of two Coulombically interacting charged particles. This theory accurately represented the present data and also predicted the measurements in [53]. This theory was extended using fundamental plasma parametric relationships in order to predict the particle velocity as a function of power and pressure. With only one fitted parameters, this theory accurately represents the experimental trends observed with variations in power and pressure. Furthermore, this theory was explored further to suggest conditions for which particle collision events and possibly agglomeration are likely to occur. It is with high confidence that the motion of large particles can be attributed to Coulombic particle-particle interactions.

It was observed that the particle trap compresses while the plasma is ignited. Initially, the compression rate is very fast. The initial behavior correlates with the change in the plasma emission intensity with and can be correlate with the plasma going to a quasi-equilibrated state. In the long-term, the compression rate is much slower. It was experimentally shown that this is likely due to particles falling out of the particle trap during the plasma ignition. This phenomena was also explained physically. At this point, it is not conclusive that the particle trap compression is due only to particles falling out of the particle trap, however the evidence is substantial.

This research has shown experimental evidence that the trapped particles do interact coulombically, and this interaction may be the cause for particle agglomeration.

In summary,

- Laser Light Scattering techniques, Optical Emission Spectroscopy, and Laser Doppler Velocimetry were used to characterize particle interactions
- Particle trap size, local particle concentration, and particle velocity were measured as a function of power, pressure, and time.
- Initial transient behavior of the particle trap was shown to correlate well with the plasma achieving quasi-steady state.
- It was shown theoretically that for small particles, with diameters less than approximately $0.1 \mu\text{m}$, the motion of the particle is Brownian. For large particles, Brownian motion is no longer significant. The motion of the large particles is explained by charged particle Coulombic interactions.
- The Coulomb theory was extended using fundamental plasma relationships to show how the particle velocity should vary with power and pressure. Excellent agreement between the model and the experiments was observed.
- Long term behavior was shown to be likely due to particle collisions. Analysis of the probability of particle collisions showed that the collisions are indeed possible. Furthermore, if the collisions occur, an estimation of the probability that the particle would fall out of the particle trap was given.
- The equations used to describe the interactions between two charged particles were used to determine what approach velocity is required in order that a particles can overcome electrostatic repulsion and collide. It was determined that particle collisions are more likely to occur for high powers and high pressures.
- Experimental evidence suggests that if the particle trap cross section is decreasing due to particles falling out of the particle trap, contamination will be reduced as power and pressure are increased. Even though the collisions are more probable due to velocity considerations with increased power or pressure, there are other factors (i.e. strength of the forces which trap the particles) that must be considered when determining if particles are likely to fall out of the particle trap during plasma ignition.

SCIENTIFIC CONTRIBUTIONS

- Used Laser Doppler Velocimetry to study particle behavior in a particle trap. Trapped particle behavior has never been studied to this level of diagnostic sophistication. Specifically, local particle concentration and two directions of particle velocity have been measured in a particle trap. It was shown that the particle velocity is truly random. It was also shown that as the particle approaches the electrode, its velocity increases over that in the bulk particle trap.
- Coulomb theory has been used to describe the motion of large trapped particles and the dependence of this motion on reactor operating conditions. This theory agreed well with the behavioral trends and the work presented by Boufendi *et al.* in [53].
- It was experimentally observed that the particle trap compresses in time and is likely due to particles falling out of the particle trap and contaminating the wafer during the reaction.
- Probability of large particle collisions as a function of power and pressure was predicted using the experimentally verified Coulomb theory.

LIST OF SYMBOLS

Symbol	Quantity
A	Trap cross sectional area
A_{mv}	Measurement volume cross sectional area
C	Particle concentration
C_c	Cunningham correction factor
D_i	Diffusivity of species <i>i</i>
D_{mv}	Measurement volume diameter
E	Electric field strength
E_0	Amplitude of rf electric field
E_p	Particle electric field
E_{rf}	rf Electric field
F_{12}	Coulombic interaction force
F_d	Drag Force
F_E	Electrostatic force
F_g	Gravitational force
F_i^c	Ion collision force
F_i^o	Ion orbital force
F_n^c	Polarized argon collision force
F_t	Thermophoretic force
FWHM	Full width at half maximum
I	Intensity

I_{INC}	Incident intensity
I_s	Scattered intensity
J	Velocity distribution function
L	Electrode spacing
N	Number of particles
PV	Probe volume
Q_p	Particle charge
R	Chamber Radius, OES Resolution
T	Temperature
T_e	Electron temperature
T_i	Ion temperature
T_p	Particle temperature
V, \bar{V}	Chamber volume
V	Sample Volume
V_{50}	50% fraction velocity
V_{Ar}	Argon velocity
V_o	Initial velocity
V_p	Particle velocity
W	rf plasma power
a	proportionality constant
b_c	Collision frequency coefficient
$b_{\pi/2}$	Collision cross section
c	Proportionality constant, Speed of light
d	Interparticle spacing, Spacing between gratings
d_o	Atom diameter
d_p	Particle diameter

e	Electron
eV	Electron voltage
f_e	Electron energy distribution function
f_t	Temporal frequency
g	Gravitational constant
h	Plank's constant
k_B	Boltzmann factor
ks	$2\pi n_{ri}/\lambda_o$
m_{Ar}	Mass of one argon atom
m_e	Rest electron mass
m_i	Ion mass
m_n	Neutral mass
m_p	Particle mass
m_r	Reduced mass
n	Gas density, Number of illuminated gratings
n_e	Electron concentration
\bar{n}_e	Average electron concentration
n_i	Ion concentration
n_n	Neutral concentration
n_p	Particle concentration
n_{ri}	Refractive index
p	Pressure
q	Electron charge
r	Separation distance
r_o	Radius of sphere of influence, Initial separation distance
r_p	Particle radius

t	Time
t_d	Interarrival time
t_g	Gate time
u	Gas velocity
u_B	Bohm velocity
v	Particle velocity
v_2	Velocity of particle 2
v_d	Electron drift velocity
v_i	Ion velocity
v_n	Neutral thermal velocity
v_p	Particle velocity
v_s	Ion velocity relative to moving particle
$\langle v_z \rangle$	Average axial velocity
x	Separation distance, same as r
x^*	Separation distant normalized to λ_D
x_0^*	Initial separation distant normalized to λ_D
\bar{z}	Interarrival spacing
$+$	Positive ion
$-$	Negative ion
Λ	Electron diffusion length
Γ	Collision interaction parameter
Γ_i	Flux of species i
Γ_{*p}	Interaction potential for polarized argon and particle
Ξ	Empirical constant
α	Polarizability of a particle
α_{Ar}	Polarizability of argon
β	Coulombic coupling parameter
δ	Fringe spacing

ϵ	Energy of a photon, Electron energy
ϵ_0	Vacuum permittivity
γ	Beam intersection angle
κ	empirical constant
λ	Mean free path, Photon wavelength, Laser wavelength
λ_{AVE}	Average wavelength
λ_b	Blaze wavelength
λ_D	Debye length
λ_0	Incident laser wavelength
μ	Dipole moment
μ_g	Gas viscosity
μ_i	Permittivity of species i
ν	Photon frequency
ν_c	Collision frequency
θ	Angle between incident and scattered light
ρ_p	Particle density
σ	Cross section for photon emission
ω	rf frequency
ξ	empirical constant

REFERENCES

- [1] G. Moore, "Solid state VLSI: some fundamental challenges" *IEEE Spectrum*, Vol. 16, No. 4, p. 30, 1979.
- [2] M. Garrity, T. Peterson, L. Garrett, and J. O'Hanlon. "Fluid simulation of particle contamination in postplasma processes", *Journal of Vacuum Science and Technology A*, vol. 13, no. 6, 1995.
- [3] R. Blewer, "Trends in Advanced Integrated Circuit Metallization", Chemical and Environmental Engineering Seminar Series, University of Arizona, Arizona, April 22, 1997.
- [4] G. Selwyn, J. McKillop, K. Haller, and J. Wu, "*In situ* plasma contamination measurements by HeNe laser light scattering: A case study", *Journal of Vacuum Science and Technology A*, vol. 8, p. 1726, 1990.
- [5] A. Bouchoule, A. Plain, L. Boufendi, J. Blondeau, and C. Laure, "Particle generation and behavior in a silane-argon low-pressure discharge under continuous or pulsed radio-frequency excitation", *Journal of Applied Physics*, Vol. 70, No. 4, p. 1991, 1991; A. Boufendi, A. Plain, J. Blondeau, A. Bouchoule, C. Laure, and M. Toogood, "Measurement of particle size kinetics from nanometer to micrometer scale in a low-pressure argon-silane radio-frequency discharge", *Applied Physics Letters*, Vol. 60, No. 2, p. 169, 1992.
- [6] S. Choi and M. Kushner, "The role of negative ions in the formation of particles in low-pressure plasmas", *Journal of Applied Physics*, Vol. 74, No. 2, p. 853, 1993.
- [7] Y. Watanabe and M. Shiratani, "Growth kinetics and behavior of dust particles in silane plasmas", *Japanese Journal of Applied Physics*, Vol. 32, p. 3074, 1993.
- [8] J. Perrin, C. Bohm, R. Etemadi, and A. Lloret, "Possible routes for cluster growth and particle formation in RF silane discharges", *Plasma Sources Science and Technology*, Vol. 3, No. 3, p. 252, 1994.

- [9] L. Boufendi, J. Hermann, A. Bouchoule, B. Dubreuil, E. Stoffels, W. Stoffels, and M. de Giorgi, "Study of initial dust formation in an Ar-SiH₄ discharge by laser induced particle explosive evaporation", *Journal of Applied Physics*, Vol. 76, No. 1, p. 148, 1994.
- [10] K. Kim and M. Ikegawa, "Particle growth and transport in silane plasma chemical vapour deposition", *Plasma Sources Science and Technology*, Vol. 5, p. 311, 1996.
- [11] W. Reents and M. Mandich, "Water induced particle formation in the ion chemistry of silane", *Plasma Sources Science and Technology*, Vol. 3, No. 3, p. 373, 1994.
- [12] G. Jellum and D. Graves, "Particulates in aluminum sputtering discharges", *Journal of Applied Physics*, Vol. 67, No. 10, p. 6490, 1990.
- [13] W. Yoo and Ch. Steinbrüchel, "Growth of plasma-generated particles and behavior of particle clouds during sputtering of silicon and silicon dioxide", *Journal of Vacuum Science and Technology A*, Vol. 11, No. 4, p. 1258, 1993.
- [14] G. Kroesen, W. Stoffels, E. Stoffels, M. Haverlag, J. den Boer, and F. de Hoog, "Negative ions and particle formation in low-pressure halocarbon discharges", *Plasma Sources Science and Technology*, Vol. 3, No. 3, p. 246, 1994.
- [15] R. Buss and W. Hareland, "Gas phase particulate formation in radio-frequency fluorocarbon plasmas", *Plasma Sources Science and Technology*, Vol. 3, No. 3, p. 268, 1994.
- [16] R. Buss and S. Babu, "Synthesis of silicon nitride particles in pulsed radio frequency plasmas", *Journal of Vacuum Science and Technology*, Vol. 14, No. 2, p. 577, 1996.
- [17] G. Selwyn, "Electrode Engineering, a new technology for control of particle contamination and process uniformity in plasma processing", in "The Physics of Dusty Plasmas", P. Shukla, D. Mendis and V. Chow, eds., World Scientific, 1996.
- [18] A. Paranjpe, J. McVittie, and S. Self, "Algorithms for numerical simulation of radio-frequency glow discharges", *Physical Review A*, Vol. 41, No. 12, p. 6949, 1990.
- [19] J. Boeuf, "Numerical model of rf glow discharges", *Physical Review A*, Vol. 36, No. 6, p. 2782, 1987.

- [20] D. Graves and K. Jensen, "A continuum model of DC and RF discharges", *IEEE Transactions on Plasma Science*, Vol. PS-14, No. 2, p. 78, 1986.
- [21] P. Ventzek, R. Hoekstra, and M. Kushner, "Two dimensional modeling of high plasma density inductively coupled sources for materials processing", *Journal of Vacuum Science and Technology B*, Vol. 12, p. 461, 1994.
- [22] S. Collins, "Particle trapping, transport and charge in capacitively and inductively coupled plasmas in a gaseous electronics conference RF reference cell", Ph.D. dissertation, University of Arizona, 1996.
- [23] J. Kang, "The particle trap and plasma parameter studies in an RF argon discharge", Ph.D. dissertation, University of Arizona, 1997.
- [24] R. Carlile and S. Geha, "Physical properties of contamination particle traps in a process plasma", *Journal of Applied Physics*, Vol. 73, No. 10, p. 4785, 1993.
- [25] J. O'Hanlon, J. Kang, K. Russel, and L. Hong, "The effects of electrostatic, molecular drag and gravitational forces on the behavior of particle clouds in an RF discharge", *IEEE Transactions on Plasma Science*, Vol. 22, No. 2, p. 122, 1994.
- [26] S. Collins, D. Brown, J. O'Hanlon, and R. Carlile, "Particle trapping, transport and charge in capacitively and inductively coupled plasmas in a gaseous electronics conference RF reference cell", *Journal of Vacuum Science and Technology A*, Vol. 14, No. 2, p. 634, 1996.
- [27] S. Beck, S. Collins, and J. O'Hanlon, "A study of methods for moving particles in RF processing plasmas", *IEEE Transactions on Plasma Science*, Vol. 22, No. 2, p. 128, 1994.
- [28] E. Stoffels, W. Stoffels, D. Vender, G. Kroesen, and F. de Hoog, "Laser-particle interactions in a dusty RF plasma", *IEEE Transactions on Plasma Science*, Vol. 22, No. 2, p. 116, 1994.
- [29] G. Selwyn, "A Phenomenological study of particulates in plasma tools and processes", *Japanese Journal of Applied Physics*, Vol. 32, p. 3068, 1993.
- [30] P. Cabarrocas, P. Gay, and A. Hadjadj, "Experimental evidence for nano-particle deposition in continuous argon-silane plasmas: Effects of silicon nanoparticles on film properties", *Journal of Vacuum Science and Technology A*, Vol. 14, No. 2, p. 655, 1996.

- [31] S. Cohen, "An introduction to plasma physics for materials processing", in "Plasma etching, an introduction", D. Manos and D. Flamm, eds., Academic Press, Inc., 1989.
- [32] E. Meeks and J. Shon, "Modeling of plasma-etch processes using well stirred reactor approximations and including complex gas-phase and surface reactions", *IEEE Transactions on Plasma Science*, Vol. 23, No. 4, p. 539, 1995.
- [33] M. Garrity, T. Peterson, and J. O'Hanlon, "Particle formation rates in sulfur hexafluoride plasma etching of silicon", *Journal of Vacuum Science and Technology A*, Vol. 14, No. 2, p. 550, 1996.
- [34] D. Rader and T. Geller, "Particle transport modelling in semiconductor process environments", *Plasma Sources Science and Technology*, Vol. 3, p. 426, 1994.
- [35] D. Graves, J. Daniels, M. Kiehlbauch, S. Mahnovski, J. Coburn, A. Fiala, M. Li, H. Singh, E. Tonnis, and C. Abrams, "Plasma modeling and diagnostic studies for PFC reduction", 1st Annual Review Meeting for the NSF/ERC Engineering Research Center for Environmentally Benign Semiconductor Manufacturing, Tucson, Arizona, 15 April, 1997.
- [36] S. Middleman and A. Hochberg, "Process Engineering Analysis in Semiconductor Device Fabrication", New York: McGraw Hill, Inc., 1993.
- [37] J. Goree and T. Sheridan, "Particulate release from surfaces exposed to a plasma", *Journal of Vacuum Science and Technology A*, Vol. 10, No. 6, p. 3540, 1992.
- [38] G. Selwyn, J. Singh, and R. Bennet, "In situ laser diagnostic studies of plasma-generated particulate contamination", *Journal of Vacuum Science and Technology A*, Vol 7, No. 4, p. 2758, 1989.
- [39] Ch. Hollenstein, W. Schwarzenbach, A. Howling, C. Courteille, J. Dorier, and L. Sansonnens, "Anionic clusters in dusty hydrocarbon and silane plasmas", *Journal of Vacuum Science and Technology A*, Vol. 14, No. 2, p. 535, 1996.
- [40] E. Whipple, "Potentials of surfaces in space", *Rep. Prog. Phys.*, Vol. 44, p. 1197, 1981.
- [41] R. Nowlin and R. Carlile, "The electrstatic nature of contaminative particles in a semiconductor processing plasma", *Journal of Vacuum Science and Technology A*, Vol. 8, No. 5, p. 2825, 1991.

- [42] R. Hazelton, "Measurement of dust grain charging in a laboratory plasma", *IEEE Transactions on Plasma Science*, Vol. 22, No. 2, p. 91, 1994.
- [43] B. Walch, M. Horanyi, and S. Robertson, "Measurement of the charging of individual dust grains in a plasma", *IEEE Transactions on Plasma Science*, Vol. 22, No. 2, p. 97, 1994.
- [44] A. Garscadden, B. Ganguly, P. Haaland, and J. Williams, "Overview of growth and behavior of clusters and particles in plasmas", *Plasma Sources Science and Technology*, Vol. 3, No. 3, p. 239, 1994.
- [45] M. Barnes, J. Keller, J. Forster, J. O'Neill, and D. Coultas, "Transport of dust particles in glow-discharge plasmas", *Physical Review Letters*, Vol. 68, No. 3, p. 313, 1992.
- [46] F. Huang, H. Hwang, and M. Kushner, "A model for transport and agglomeration of particles in reactive ion etching plasma reactors", *Journal of Vacuum Science and Technology A*, Vol. 14, No. 2, p. 562, 1996.
- [47] O. Havnes, T. Nitter, V. Tsytovich, G. Morfill, and T. Hartquist, "On the thermophoretic force close to walls in dusty plasma experiments", *Plasma Sources Science and Technology*, Vol. 3, No. 3, p. 448, 1994.
- [48] G. Jellum, J. Daugherty, and D. Graves, "Particle thermophoresis in low pressure glow discharges", *Journal of Applied Physics*, Vol. 69, No. 10, p. 6923, 1991.
- [49] D. Bohm, "Minimum ionic kinetic energy for a stable sheath" in *The Characteristics of Electrical Discharges in Magnetic Fields*, A. Guthry and R. Wakerling, eds., New York: McGraw Hill, p. 77, 1949.
- [50] A. Bouchoule and L. Boufendi, "High concentration effects in dusty plasmas", *Plasma Sources Science and Technology*, Vol. 3, No. 3, p. 292, 1994.
- [51] J. Prausnitz, R. Lichtenhaler, and E. de Azevedo, *Molecular Thermodynamics of Fluid-Phase Equilibria*, 2nd edition, New Jersey: P T R Prentice Hall, p. 55, 1986.
- [52] J. Daugherty and D. Graves, "Particle temperature in radio-frequency glow discharges", *Journal of Vacuum Science and Technology A*, Vol. 11, No. 4, p. 1126, 1993.
- [53] L. Boufendi, A. Bouchoule, R. Porteous, J. Blondeau, and C. Laure, "Particle-particle interactions in dusty plasmas", *Journal of Applied Physics*, Vol. 73, No. 5, p. 2160, 1993.

- [54] T. Kihara, *Advanced Chemical Physics*, Vol. 1, p. 276, 1958.
- [55] A. Ikezi, "Coulomb solid of small particles in a plasma", *Physics of Fluids*, Vol. 29, p. 1764, 1986.
- [56] H. Thomas, G. Morfill, V. Demmel, J. Goree, B. Feuerbacher, and D. Möhlmann, "Plasma crystal: coulomb crystallization in a dusty plasma", *Physical Review Letters*, Vol. 73, p. 652, 1995.
- [57] J. Chu and L. I, "Direct observation of coulomb crystals and liquids in rf dusty plasmas", *Physical Review Letters*, Vol. 72, p. 4009, 1994.
- [58] G. Lapenta, "Particle in cell simulation of particulates in glow discharges and in space plasmas" in the *Physics of Dusty Plasmas*, P. Shukla, D. Mendis, and V. Chow, eds., World Scientific, 1996.
- [59] H. Thomas and G. Morfill, "Plasma crystals - structural properties and melting transition" in the *Physics of Dusty Plasmas*, P. Shukla, D. Mendis, and V. Chow, eds., World Scientific, 1996.
- [60] D. Dubin and T. O'Neil, "Pure ion plasmas, liquids, and crystals", *Physics of Fluids*, P2, p. 460, 1992.
- [61] E. Brittain, W. George, and C. Wells, *Introduction to Molecular Spectroscopy Theory and Experiment*, London: Academic Press, 1970.
- [62] L. Pauling and E. Wilson Jr., *Introduction to Quantum Mechanics with Applications to Chemistry*, Dover Publishing Inc., 1985.
- [63] S. Baskin and J. Stoner, *Atomic Energy Levels and Grotrian Diagrams*, New York: American Elsevier Publishing Co., 1975.
- [64] A. Straheim, in *Radiation Chemistry: Principles and Applications*, Farataziz and Rodgers, eds., New York: VCH Publishers, Inc., 1987.
- [65] M. Dalvie, G. Selwyn, M. Surendra, C. Guarnieri, and J. McGill, "Detection of particle traps by spatially resolved optical emission spectroscopy over grooved electrodes in radio frequency discharges", *Applied Physical Letters*, vol. 63, p. 3279, 1993; R. Carlile, J. O'Hanlon, L. Hong, M. Garrity, and S. Collins, "Contamination and particle traps due to a cone, cube, and disk", *Plasma Sources Science and Technology*, vol. 3, p. 334, 1994.

- [66] B. Chu, *Laser Light Scattering, basic principles and practice*, 2nd edition, Boston: Academic Press, Inc., 1991
- [67] Aerometrics Inc., a subsidiary of TSI Inc., 755 N. Mary Avenue, Sunnyvale, CA 94086 ph: (408)-738-6688.
- [68] S. Sankare, K. Ibrahim, and W. Bachalo, "Coherent scattering of multiple particles in phase Doppler interferometry", *Particle-Particle Systems Characterization II*, p. 35, 1994.
- [69] *Real Time Signal Analyzer Hardware Manual*, Aerometrics, Inc., 755 N. Mary Ave., Sunnyvale, CA 94086.
- [70] K. Ibrahim, M. Fidrich, and W. Bachalo, "Evaluations of an advanced real-time signal processing system using the Fourier transform", presented at The Second International Conference on Fluid Dynamics Measurements and its Applications, Beijing, China, 1994.
- [71] K. Ibrahim and W. Bachalo, "The significance of the Fourier analysis in signal detection and processing in laser Doppler and phase Doppler applications", in *Proceedings of the Sixth International Symposium on Applications of Laser Technologies to Fluid Mechanics*, Lisbon, Portugal, 1992.
- [72] C. Koh, P. Hookham, and L. Leal, "Experimental investigation of concentrated suspension flows in a rectangular channel", *Journal of Fluid Mechanics*, Vol. 266, p.1, 1993.
- [73] Personal discussion with Carlos Schuler, formerly of Aerometrics Inc.
- [74] J. Zhu, R. Rudoff, E. Bachalo, and W. Bachalo, "Number density and mass flux measurements using the phase Doppler particle analyzer in reacting and non-reacting swirling flows", presented at the 31st Aerospace Sciences Meeting and Exhibit, Reno NV, 1993, AIAA 93-0361.
- [75] R. van de Wall and S. Soo, "Measurement of transport properties of gas-solid suspension using phase Doppler anemometry", submitted to *Powder Technology*.
- [76] D. Winske, "Numerical simulation of dusty plasmas", p. 60; N. d'Angelo, A. Barkan, and R. Merlino, "Experiments on dust-plasma interactions", p. 93; R. Merlino and A. Barkan, "Confinement of dust particles in a double layer", p. 102; in "The Physics of Dusty Plasmas, P. Shukla, D. Mendis, and V. Chow, eds., Singapore: World Scientific, 1996.

- [77] V. Donnelly, "A simple optical emission method for measuring percent dissociations of feed gases in plasmas: Application to Cl_2 in a high-density helical resonator plasma", *Journal of Vacuum Science and Technology A*, Vol. 14, No. 3, p. 1076, 1996.
- [78] R. Carlile, S. Geha, J. O'Hanlon, and J. Stewart, "Electrostatic trapping of contamination particles in a process plasma environment", *Applied Physics Letters*, Vol. 59, No. 10, p. 1167, 1991.
- [79] J. Goree, "Charging of particles in a plasma", *Plasma Sources Science and Technology*, Vol. 3, No. 3, p. 400, 1994.
- [80] M. Garrity, PhD dissertation, University of Arizona, *in progress*.
- [81] J. Seinfeld, "Atmospheric Chemistry and Physics of Air Pollution", New York: John Wiley and Sons, 1986.